



BRNO UNIVERSITY OF TECHNOLOGY

VYSOKÉ UČENÍ TECHNICKÉ V BRNĚ

FACULTY OF ELECTRICAL ENGINEERING AND COMMUNICATION

FAKULTA ELEKTROTECHNIKY A KOMUNIKAČNÍCH TECHNOLOGIÍ

DEPARTMENT OF TELECOMMUNICATIONS

ÚSTAV TELEKOMUNIKACÍ

RECENT ADVANCES IN FRACTIONAL-ORDER ANALOG CIRCUITS

NEJNOVĚJŠÍ POKROKY V OBLASTI ANALOGOVÝCH OBVODŮ ZLOMKOVÉHO ŘÁDU

HABILITATION THESIS

HABILITAČNÍ PRÁCE

AUTHOR
AUTOR PRÁCE

Ing. DAVID KUBÁNEK, Ph.D.

BRNO 2022

Abstract

This habilitation thesis is focused on research in the area of analog linear electrical circuits of fractional, i.e. non-integer order. These function blocks provide new, more general and flexible characteristics that cannot be obtained by classic integer-order circuits or only at the cost of increasing their complexity. The thesis is divided into seven main chapters, which are initially focused on the motivation, the goals of the work and the description of the current state of the art. Subsequently, the method of realizing passive circuit elements with fractional-order impedance using layered resistive-capacitive structures with distributed parameters is presented. Further, the possibilities of transforming fractional-order impedances using active circuits to obtain a wider range of available parameters of these elements are described. This is followed by a chapter dealing with modeling the impedance properties of biological materials, specifically the cardiac cell membrane, using fractional-order impedance elements. The next part of the thesis is focused on frequency filters of fractional order. Different forms of transfer functions of these filters are presented and their coefficients are found for various types of filter characteristics. The final chapter deals with fractional-order oscillators and their specific features that distinguish them from their integer-order counterparts. For all presented solutions, properties are verified using computer simulations or experimental measurements, and the achieved results are evaluated. The text is written to have not only scientific but also pedagogical contribution. The thesis consists primarily of original research of its author in years after his Ph.D. thesis defense. All presented solutions were published in journals with impact factor or presented at international conferences.

Keywords

fractional-order circuit, fractional-order element, element with distributed parameters, impedance transformation, fractional-order impedance model, fractional-order filter, fractional-order oscillator

Abstrakt

Tato habilitační práce je zaměřena na výzkum v oblasti analogových lineárních elektronických obvodů zlomkového, někdy též označovaného fraktálního, tedy neceločíselného řádu. Tyto funkční bloky poskytují nové, obecnější a flexibilnější charakteristiky, které nemohou být získány klasickými obvody celočíselného řádu nebo pouze za cenu zvýšení jejich složitosti. Práce je členěna do sedmi hlavních kapitol, které jsou zpočátku zaměřeny na motivaci vzniku práce, cíle práce a popis současného stavu dané problematiky. Následně je představena metoda realizace pasivních obvodových prvků s impedancí zlomkového řádu pomocí vrstevných rezistivně-kapacitních struktur

s rozprostřenými parametry. Dále jsou popsány možnosti transformací impedancí zlomkového řádu pomocí aktivních obvodů vedoucí k získání širší škály dostupných parametrů těchto prvků. Následuje kapitola zabývající se modelováním impedančních vlastností biologických materiálů, konkrétně membrány srdeční buňky, pomocí prvků s impedancí zlomkového řádu. Další část práce je zaměřena na kmitočtové filtry zlomkového řádu. Jsou představeny různé typy přenosových funkcí těchto filtrů a nalezeny jejich koeficienty pro různé druhy filtračních charakteristik. Závěrečná kapitola pojednává o oscilátorech zlomkového řádu a jejich specifických vlastnostech, kterými se odlišují od obvodů celočíselného řádu. U všech prezentovaných řešení je provedeno ověření vlastností pomocí počítačových simulací nebo experimentálního měření a dosažené výsledky jsou zhodnoceny. Práce je psána tak, aby měla nejen vědecký, ale i pedagogický přínos. Jejím obsahem jsou především originální výsledky výzkumu autora v době po obhajobě jeho doktorské práce. Všechna prezentovaná řešení byla publikována v impaktovaných časopisech nebo prezentována na mezinárodních konferencích.

Klíčová slova

obvod zlomkového řádu, prvek zlomkového řádu, prvek s rozprostřenými parametry, impedanční transformace, impedanční model zlomkového řádu, filtr zlomkového řádu, oscilátor zlomkového řádu

KUBÁNEK, David *Recent Advances in Fractional-Order Analog Circuits*: habilitation thesis. Brno: Brno University of Technology, Faculty of Electrical Engineering and Communication, Department of Telecommunications, 2022. 134 p.

Author's Declaration

I declare that I have written my habilitation thesis on the theme of “Recent Advances in Fractional-Order Analog Circuits” independently and using the technical literature and other sources of information which are all quoted in the thesis and detailed in the list of literature at the end of the thesis.

As the author of the habilitation thesis, I furthermore declare that, as regards the creation of this habilitation thesis, I have not infringed any copyright. In particular, I have not unlawfully encroached on anyone's personal and/or ownership rights and I am fully aware of the consequences in the case of breaking Regulation §11 and the following of the Copyright Act No 121/2000 Sb., and of the rights related to intellectual property right and changes in some Acts (Intellectual Property Act) and formulated in later regulations, inclusive of the possible consequences resulting from the provisions of Criminal Act No 40/2009 Sb., Section 2, Head VI, Part 4.

Brno, October 24, 2022

author's signature

Acknowledgements

I would like to express my sincerest thanks to Prof. Ing. Kamil Vrba, CSc., for guiding me since my Ph.D. studies and from the beginning of my scientific and also pedagogic career at Department of Telecommunications, for giving me valuable hints innumerable times and for providing me plenty of opportunities to grow, not only professionally.

My special thanks go to prof. Ing. Jaroslav Koton, Ph.D., doc. Ing. Jan Jeřábek, Ph.D., doc. Ing. Norbert Herencsár, Ph.D., Ing. Jan Dvořák, Ph.D. and other colleagues from Brno University of Technology for close collaboration and fruitful discussions made on everyday basis.

Finally, and most importantly, I would very much like to thank for support of my family. It would not be possible to manage without tolerance and understanding of my wife Anna and kids Monika and Pavel.

Brno, October 24, 2022

author's signature

Contents

INTRODUCTION	8
1. THESIS OVERVIEW	9
1.1 MOTIVATION	9
1.2 GOALS	11
1.3 CONTRIBUTION	12
1.3.1 <i>Relation to Author's Publications</i>	13
1.4 THESIS STRUCTURE	14
2. STATE OF THE ART	15
2.1 FRACTIONAL-ORDER ELEMENTS	15
2.2 FRACTIONAL-ORDER FILTERS	17
2.3 FRACTIONAL-ORDER OSCILLATORS	18
3. FOE WITH DISTRIBUTED RC LAYERS	20
3.1 DESCRIPTION OF SYNTHESIS METHOD AND ALGORITHM	21
3.2 VERIFICATION OF SYNTHESIS	27
3.3 CONCLUSIONS OF THE SYNTHESIS METHOD	29
4. IMPEDANCE TRANSFORMATIONS OF FOE	30
4.1 GYRATOR-BASED FO INDUCTOR	30
4.1.1 <i>Influence of OTA Terminal Impedances</i>	32
4.1.2 <i>Dynamic Properties</i>	35
4.1.3 <i>Simulation Results and Concluding Remarks</i>	36
4.2 FOE OF COMPLEMENTARY ORDER	38
4.2.1 <i>Implementation by GIC</i>	40
4.3 FOE SERIES USING GIC	41
4.3.1 <i>Implementation and Properties of GIC</i>	45
4.3.2 <i>Influence of OTA Parasitics and Optimization of GIC Performance</i>	47
4.3.3 <i>OTA-Based Circuit with Negative Conductance</i>	52
4.3.4 <i>Simulation Results</i>	53
4.3.5 <i>Optimization Examples</i>	57
5. IMPEDANCE MODELS EMPLOYING FOE	60
5.1 FOE IN CARDIAC CELL MEMBRANE MODEL	60
5.1.1 <i>Cell Membrane Measurement Technique</i>	61
5.1.2 <i>Analytical Formulas and Least Squares Fitting</i>	63
5.1.3 <i>Results and Discussion</i>	65
6. FO ANALOG FREQUENCY FILTERS	69
6.1 FO FILTERS WITH ARBITRARY QUALITY FACTOR	69
6.1.1 <i>Transfer Functions and Coefficient Search</i>	69
6.1.2 <i>Results and Discussion</i>	71
6.1.3 <i>Circuit Implementation and Simulation</i>	76
6.1.4 <i>Concluding Remarks</i>	79
6.2 FO BAND-PASS FILTERS WITH ADJUSTABLE SLOPE	79

6.2.1	<i>Transfer Functions and Coefficient Search</i>	80
6.2.2	<i>Results and Discussion</i>	84
6.2.3	<i>Circuit Implementation and Simulation</i>	88
6.2.4	<i>Concluding Remarks</i>	89
6.3	<i>(N + A)-ORDER TRANSFER FUNCTIONS</i>	90
6.3.1	<i>Transfer Functions and Coefficient Search</i>	90
6.3.2	<i>Results and Discussion</i>	93
6.3.3	<i>Extension to High-Pass Filters</i>	97
6.3.4	<i>Circuit Implementation and Simulation</i>	97
6.3.5	<i>Concluding Remarks</i>	100
6.4	<i>OTHER AUTHOR'S WORKS ON FO FILTERS</i>	101
6.4.1	<i>Implementations and Analyses of FO Filters</i>	101
6.4.2	<i>FO Filters with Elliptic Responses</i>	102
6.4.3	<i>FO Filters Approximated by IO Rational Transfer Functions</i>	102
7.	FO OSCILLATORS	104
7.1	<i>FO OSCILLATOR DESIGN AND EVALUATION</i>	104
7.1.1	<i>Oscillation Frequency Tuning</i>	106
7.1.2	<i>Simulation and Experimental Measurement</i>	109
7.1.3	<i>Concluding Remarks</i>	112
8.	CONCLUSION	113
	BIBLIOGRAPHY	115
	ABBREVIATIONS AND SYMBOLS	128
	LIST OF FIGURES	131
	LIST OF TABLES	134

INTRODUCTION

Despite of strong effort to replace analog electronic systems by fully digital substitutes, there are still areas where analog circuits play an important role and cannot be simply overwhelmed. It is valid especially in the cases, where low power consumption, high-frequency signal processing, high spectral purity, fast response, minimized delay, real-time processing, and/or implementation of complex transfer functions are required. There are also many systems where analog approach is simpler, cheaper, or sufficient compared to the digital solution. The analog systems have typical drawbacks compared to their digital counterparts, such as aging of elements leading to long-lasting gradual change of their properties; dependence of parameters on temperature, supply voltage, electromagnetic field; more complicated design taking many conditions and parameters into account, etc. [1]. Many of these shortcomings of analog circuits have been minimized by various self-trimming and self-compensation techniques [2], [3] and analog signal processing is and will always be considered irreplaceable and indispensable in future circuit designs.

The properties of analog electronic circuits are given by their structure and parameters of used components. If operational amplifiers are used as active elements, setting the characteristics of circuits is possible only by changing the values of passive elements, i.e. most often the resistance of resistors or capacitance of capacitors. To overcome this limitation, many advanced active elements with electronically adjustable parameters have been developed [4]. Most of the basic active elements offer only single parameter control, i.e. of the transconductance in the case of the operational transconductance amplifier (OTA) [5], resistance of current input terminal (X) in current controlled current conveyor of second generation (CCCII) [6], transresistance of the operational transresistance amplifier (OTRA) [7], etc.

These elements enabled extensive options for setting the parameters of circuits intended for generation, conversion, modulation, compression/expansion, filtering, shaping, etc. of analog signals. However, the development in the possibilities of setting and universality of characteristics progressed even further, when fractional-order circuits appeared. These circuits, which are the main focus of this thesis and which will be discussed in more detail in the following parts, provide properties that cannot be realized by classic circuits or only at the cost of increasing their complexity. Possibility to obtain such arbitrary circuit characteristics is very beneficial in many applications e.g. for dynamic shaping of spectral character of particular signals in biomedical signal processing [8], [9], for modeling of electrical parameters of biological materials and tissues [10], [11], [12] in communications [13], or in automation and control systems [14].

1. THESIS OVERVIEW

This chapter contains an overview of this thesis. In Section 1.1, the motivation of the thesis is described and the main goals are summarized in Section 1.2. The contribution to the scientific topic of the thesis and author's related publication activities are briefly discussed in Section 1.3. Finally, organization of this thesis is introduced in Section 1.4.

1.1 Motivation

Fractional calculus is a branch of mathematical analysis that deals with derivatives and integrals having non-integer, i.e. fractional order [15], [16]. Its foundations were laid more than 300 years ago, but only a few decades ago it was found to be a very useful mathematical instrument that can be used in numerous seemingly diverse and widespread fields of practical science and engineering. Fractional calculus has gradually penetrated many disciplines, such as physics, system theory, signal processing, material theory, economics, electrical engineering, bioengineering, chemical engineering, medicine, optics, geology, etc. [8] – [22].

So far, several formulas have been defined for the calculation of fractional derivatives or integrals. As an example, let us present the Grünwald-Letnikov fractional derivative formula [16]

$${}_{t_0}D_t^\alpha f(t) = \lim_{h \rightarrow 0} \frac{1}{h^\alpha} \sum_{m=0}^{\left[\frac{t-t_0}{h} \right]} (-1)^m \frac{\Gamma(\alpha+1)}{m! \Gamma(\alpha-m+1)} f(t-mh). \quad (1.1)$$

Here, $\Gamma(\cdot)$ is the Gamma function, α is a real number representing the fractional order and t_0 and t are the terminals of fractional differentiation. The Grünwald-Letnikov definition is presented here because it leads to a correct generalization of the current linear system theory [17], but it is important to note that other definitions e.g. by Riemann-Liouville and Caputo are also available for describing fractional derivatives.

As mentioned, fractional calculus is increasingly employed in theory of systems, where differential and integral equations are widely used to describe their behaviour. It is proved that by generalizing the order of differentiation or integration in these equations from integer to fractional, it is possible to obtain more general properties or more accurate description of various dynamical systems. Such systems described by integro-differential equations of fractional order are called fractional-order (FO) systems.

As it is common in electrical circuit theory, to avoid solving differential equations in the time domain, the Laplace transform with the complex variable $s = j\omega$ is utilized, which leads to simpler algebraic expressions describing the analyzed circuit. By applying this transform to (1.1) with zero initial conditions with lower terminal $t_0 = 0$, the derivative of a time-domain function $f(t)$ can be converted to the frequency domain:

$$\mathcal{L}\{ {}_0D_t^\alpha f(t) \} = s^\alpha F(s), \quad (1.2)$$

where $F(s)$ is Laplace transform of $f(t)$ and thus, the FO differentiation is expressed simply as multiplication by s^α .

Generalizing classic capacitor or inductor to FO domain, fractional-order elements (FOE) or fractors realizing differentiation or integration of fractional order between cross voltage and through current have been defined [23]. The admittance of FOE can be written as $Y(s) = s^\alpha F_0$, where F_0 is a proportionality constant generally referred to as fractance, and therefore FOE directly implements the FO differentiation according to the relation (1.2). Considering $\alpha \in (0, 1)$, the element is called fractional-order capacitor (FOC), capacitive fractor or capacitive FOE and F_0 represents its pseudo-capacitance with the unit Farad/sec $^{1-\alpha}$. For $\alpha \in (-1, 0)$, the FOE is a fractional-order inductor (FOI), inductive fractor or inductive FOE with pseudo-inductance $1/F_0$ and the unit Henry/sec $^{1-\alpha}$. Apparently, choosing the values of $\alpha = -1, 0, 1$, the classic inductor, resistor, and capacitor are obtained, respectively. FOEs with higher fractional order can be also defined for $|\alpha| > 1$ as described e.g. in [24]. From the FOE admittance relation, it is apparent that the slope of its magnitude is 20α dB per frequency decade and its phase is $\alpha\pi/2$ radians or 90α degrees. As the phase is independent of frequency, this element is also referred to as constant phase element (CPE).

The complex variable s with a non-integer power can also be present in more complex functions describing not only the immittance but also the transfer properties of circuits or expressing their characteristic polynomial or equation. These FO functions can be obtained by connecting FOE to various known electrical circuits instead of standard passive elements, most often classic capacitors. Another possibility is to define completely new formats of circuit functions with the fractional power of the variable s and the subsequent search for their circuit implementation, e.g. by an approximating circuit of integer order.

The simplest FO transfer function (TF) containing only s^α multiplied by a constant is provided by the FO differentiator and integrator for α being positive and negative, respectively. More complex FO TFs in the rational form containing polynomials with the variable s raised to a non-integer exponent in at least one term are provided by FO frequency filters. There is usually a non-integer highest power of s in the denominator, and non-integer exponents may appear in other terms as well. In this area, the issue of the appropriate format of TFs and their coefficients for different types of filters (low-, high-, band-pass, band-stop) and their magnitude and phase frequency responses, as well as various time responses, still remains unexplored.

Also interesting are FO oscillators, where the fractional order α is another degree of freedom in setting the oscillation condition, oscillation frequency and especially the mutual phase shift of output signals in the case of multi-output oscillators.

Significant attention is also paid to the research of the FOE itself. Despite the intensive efforts, it has not yet been possible to find an implementation of this element that would provide sufficiently accurate impedance characteristics in a sufficient frequency range, and at the same time be compatible with modern integrated circuit manufacturing technologies. FOEs are currently most often emulated using passive ladder circuits with resistors and classic capacitors [25], which have the disadvantage of a large number of elements with a high spread of their values. Other presented implementations of FOE are mainly prototypes using various chemical substances or biological materials [26]. Due to the numerous shortcomings of these structures and their unsuitability for integrated implementation, opportunities for further research open up here.

It is obvious that the FO circuits represent an emerging field that expands the boundaries of realizable electrical systems, changing they are viewed, designed, and implemented. These changes bring the opportunity to pursue creative new designs which can reach applications ranging from biomedical signal processing to industrial control systems. Therefore, it is necessary to address this topic by tackling challenges in creating and applying new design methodologies, simulation and characterization of FO circuits, systems, and devices.

1.2 Goals

The aim of this thesis is to present new knowledge in the field of FO circuits, both those obtained by other experts and mainly those reached by the author of this work during his research activities. As described above, the importance of FO circuits is constantly growing and their further application possibilities are being sought. Their significant advantage is the possibility of realizing more general characteristics that cannot be realized by classic circuits or only at the cost of increasing their complexity. Therefore, it is necessary to advance both the theoretical understanding of the FO systems and the tools to easily implement them in order to accelerate their advancement and adoption in the practical areas of engineering instead of academic and research environments only.

The specific goals that are addressed by this thesis include:

- to provide readers with resources covering the fundamentals of FO electrical circuits and elements for analog signal processing, their usability and importance. It is also necessary to give explanation of these fundamentals and to present current state and trends in this research area;
- to demonstrate and analyze principles and properties of FOE implementations, with emphasis on the resistive-capacitive layer structure with distributed parameters. This very promising configuration is suitable for fabrication by available integration technologies, such as thick- and thin-film, or complementary metal oxide semiconductor (CMOS);
- to introduce the possibilities of transforming the impedance function of FOE using

circuits with active elements. Attention is paid mainly to the impedance inverter (gyrator), and also to the general immittance converter (GIC). Using these transformation circuits, it is possible to obtain a number of different FO elements with adjustable impedance magnitude and phase from one or a few FOEs. This technique addresses the current lack of availability of FOE with different parameter values. The aim is also to investigate the limitations of these impedance transformation circuits, to determine the influence of parasitic properties and to propose measures for their compensation;

- to show the advantages of modeling the impedance properties of biological materials using a circuit with FOE. On the example of a cell membrane, it is demonstrated that it is more appropriate to model the membrane capacitance using FOE instead of a classic capacitor;
- to design new types of FO frequency filter TFs providing responses that cannot be obtained with classic integer-order (IO) filters. Coefficients are sought for these functions, which ensure the required filter characteristics. Circuit topologies implementing these FO filtering functions are presented;
- to investigate the specific properties of FO oscillator circuits, to focus on the effect of the fractional component α on their parameters, in particular the frequency and condition of oscillations and phase shifts between output signals;
- to verify the properties of the designed structures by appropriate analyzes, simulations and in many cases also by experimental measurements. The obtained results are discussed, evaluated and compared with another solutions.

1.3 Contribution

The text of the thesis is written so that it has both a scientific and a pedagogical contribution. It should therefore serve not only experts in the field of FO circuits and systems, but also students interested in this topic to gain fundamental knowledge, overview of the current state of the art and to get acquainted with the latest scientific achievements.

The Chapter 2 has both pedagogical and scientific benefits, as it presents basic published knowledge in the field of FO systems and circuits. Chapters 3 to 5 are based on the results of the author's research activities obtained mainly in the years 2016 – 2022. These sections therefore have a predominantly scientific character, but are written to have also a pedagogical contribution and can serve, for example, Ph.D. students to gain new knowledge and build on it. The presented theoretical knowledge, methods or design procedures are supplemented by the respective circuit implementations, including the procedure of design of element parameters, and their functionality is verified by computer simulation and in many cases by experimental measurements. Attention was also paid to the analysis of real properties of the proposed solutions and the possibilities of

compensating the deviations from theoretical assumptions. Thus, the effort was to bring all the results of the author's research into the final form, which can be realized using available elements, materials or technologies. Thanks to this, the correctness of the proposed solutions is verified and the results can be easily used in practical applications.

1.3.1 Relation to Author's Publications

David Kubánek, the author of this thesis, has been engaged in research on analog electrical circuits since the beginning of his doctoral studies in 2002. Until the time of finishing this thesis, he is the author or co-author of 62 publications indexed in the Web of Science Core Collection database, whereas he is the main author in case of 19 of them. These results include 28 journal articles and 34 international conference papers and have so far received 499 citations.

During his Ph.D. studies between 2002 and 2005, the author's scientific activities mainly focused on frequency filters with non-traditional active elements. As a post-doc, he continued to research the design and analysis of linear and nonlinear analog circuits. In 2014, David Kubánek began to deal with systems, circuits and elements of fractional order, which are the content of this thesis. The results described in the following chapters have been published by the author in reputable journals and conference proceedings, and these own publications are properly cited in the text and included in the list of references. The goal is to base this thesis particularly on the most recent achievements of the author. None of the results presented in the following chapters were included in the author's Ph.D. thesis or any past author's theses.

Research results described in the thesis are partially subject of the recent Czech Science Foundation research project No. GA16-06175S – Synthesis and analysis of fractional-order systems using non-conventional active elements. Author of the thesis participated in this project from 2016 to 2018. This thesis also includes the results of the INTER-COST project LTC18022 – Analogue fractional systems, their synthesis and analysis, on which the author collaborated between 2018 and 2020. This project was part of the COST Action CA15225 – Fractional-order systems – analysis, synthesis and their importance for future design, representing a network of researchers dealing with fractional calculus and its usage in system description, modelling and design. The thesis also includes the results of the project GA19-24585S – Synthesis of reliable electrical phantoms describing fractional impedance behavior of real-world systems, solved between 2019 – 2021, in which David Kubánek also participated.

During his scientific activities, the author of this thesis collaborated with several foreign experts in the field and scientific workplaces. In the area of FOEs it was with prof. Ushakov from Kalashnikov Izhevsk State Technical University, Russia. The FO filters were investigated in collaboration with Dr. Todd Freeborn from University of Alabama, Tuscaloosa, USA and Dr. Shibendu Mahata from Dr. B. C. Roy Engineering College, Durgapur, India. In many topics of FO circuit design, the author collaborated with prof.

Costas Psychalinos from University of Patras, Greece and prof. Darius Andriukaitis from Kaunas University of Technology, Lithuania.

1.4 Thesis Structure

The thesis is divided into seven basic chapters. Chapter 1 gives the thesis overview including the motivation, goals and contribution. The state of the art in the field of FO elements and circuits is introduced in Chapter 2. Design techniques and verification of FOEs based on resistive-capacitive layer structures with distributed parameters are given in Chapter 3. Chapter 4 deals with impedance transformations of FOE resulting in an increase in the number or range of fractance or order values. Chapter 5 discusses employing FOEs in impedance models, particularly in cardiac cell membrane model. Chapters 6 and 7 describe design and evaluation of FO filters and oscillators, respectively. Chapter 8 concludes the thesis.

2. STATE OF THE ART

As already mentioned in the Section 1.1, mathematical basics of description of FO systems were laid nearly 300 years ago as a foundation of fractional calculus. Since that it has gained deeply rooted mathematical concepts and today it is known that many real-world dynamic systems cannot be exactly described by a system of simple differential equations of integer order. FO systems have lately been attracting significant attention and gaining more acceptance as generalization to classic IO systems.

FO systems are an evolving area of multidisciplinary research, which gives rise to many new potential applications [22]. Evidence of this can be found in the study [21] which described the FO systems as “21st century systems”. The reason for the increased interest in fractional calculus and FO system design may be seen in the fact that the presence of fractional order represents another degree of freedom to mathematically describe the behavior of a function block. This enables one to provide characteristics in between integer orders in comparison to standard IO systems, which may become beneficial while more accurate signal generation, processing and measurement, and/or system modeling and control is required.

Given that the contribution of this thesis can be divided into three main areas, including FO impedance elements, FO frequency filters, and FO oscillators, the further description of the current state of knowledge will be divided in this sense into the following three sections.

2.1 Fractional-Order Elements

Although mathematical description of fractional calculus, its derivatives and integrals is generally known [16] and is being further developed, e.g. [27], [28], there is a gap in availability of electronic function blocks needed to implement required FO operations on analog signals. This is due to the fact that FOEs are still not readily available as it is the case of other standard elements, such as resistors, capacitors, inductors, various types of active elements, etc.

The recent survey on possible techniques and approaches to design single or multi-component FOE as being proposed by different research groups can be found in [26]. Here the authors state that particularly single-component FOEs are being researched upon vigorously. They are mostly based on electrochemical principles utilizing various chemical substances, for example porous polymer materials [29], nanocomposites of conductive particles in dielectric [30], [31], [32] or layered structures in dielectric [33], [34]. These elements are mostly designed on the basis of choice of suitable materials, their arrangement and fabrication technologies by conducting many experiments, but no algorithms using exact circuit theory laws are employed. The experimental results are used to derive approximated design equations by regression methods. Common features

of these elements are low range of the fractional order α and/or narrow frequency band of the constant phase shift. None of the elements is currently commercially available in the solid-state form and most of them also do not have any dependence relation between the order α and the electrochemical parameters [26].

Thus, a common way to obtain FOEs is their emulation by multicomponent IO passive or active circuits. The method is based on the approximation of the term s^α in the impedance function by IO rational function [35] – [39]. This function is then implemented for example in the form of Foster or Cauer passive ladder networks with resistors and standard capacitors (or inductors) [25]. However, the values of these resistors and capacitors must be precise to obtain the required accuracy of approximation [25]. Furthermore, when the values of α close to 0 or 1 are required, the ratio of the resistances and capacitances is very high [40]. This makes the integration in the film or semiconductor technology very difficult or even impossible. Also, the passive emulation structures cannot be tuned electronically. The last two drawbacks mentioned are eliminated by active emulation circuits, which are usually based on state-variable multi-feedback structures whose TF equals to IO rational function approximating the required FOE impedance function [41]. These circuits can offer electronic adjustability thanks to the controlled active elements employed and are suitable for integrated implementation. The common feature of these emulation techniques is their validity only in a limited frequency band and the limited approximation accuracy highly dependent on the circuit complexity.

Although these passive and active emulators do not replace the required FOE exactly, their use is suitable for the initial validation of the proposed FO circuit solutions. The advantage of this approach is also the fact that, given the expected commercial availability of FOEs, it will be possible to simply swap the emulator structures for a given FOE and the behavior of the originally designed FO circuit will not change.

The author of this thesis with his research team focused on the development of solid-state FOEs based on resistive-capacitive layer elements with distributed parameters (RC-EDP) composed of appropriately interconnected R-C-NR structures (here R and C denote resistive and capacitive layers, respectively, and N is the ratio of layer resistances). The results of these scientific activities are described in Chapter 3.

Obtaining different parameters of FOE, i.e. the fractance and order α , requires a new design of the structure of the element or, in the case of an emulator, all the parameters of its components. This led the author and his team to explore the concept of using GIC that is capable to design a wide set of FOEs with fractional order from a specified range and electronically adjustable fractance using a very limited set of so called “seed” FOEs. These achievements are presented in Chapter 4. It should be noted here that FOE transformations using GIC were also dealt with by other authors, see e.g. [42], and it was verified that it is possible to electronically adjust the fractance value and to obtain the order not only in the range (0, 1), but also (–2, 2). However, the article [42] does not

consider extended transformation capabilities of fractional order and generating such an amount of different order values using only a few (one or two) “seed” FOEs.

Another large area of employing FOE is to model the electrical properties of various real-world substances, biological tissues and biochemical materials [10] – [12]. Modeling the impedance characteristics of various samples using electronic circuits (also called phantoms) is very important, especially in cases where it is difficult to maintain the properties of these samples over time. The Cole impedance model [43] is frequently utilized for characterizing bioimpedance properties, whereas many research studies confirmed that employing FOE instead of classic capacitor in the Cole model brings improvement in the modeling accuracy, see e.g. [10] and the references therein. The Section 5 deals with scientific achievements of the author in this field.

2.2 Fractional-Order Filters

Analog frequency filters can also be designed as FO. This approach provides more general properties, the most notable of which is the possibility of continuously adjusting the roll-off of the magnitude frequency response without limitation to multiples of 20 dB/dec as is the case of IO filters [44]. FO low-pass (LP) and high-pass (HP) filters feature the stop-band slopes of $-20(n + \alpha)$ dB/dec and $+20(n + \alpha)$ dB/dec, respectively, where n is nonnegative integer component and $\alpha \in (0, 1)$ is fractional component of the order, whereas the sum $(n + \alpha)$ is the fractional order of the filter. For example, a 2.4-order LP filter thus provides magnitude frequency response stop-band slope of -48 dB/dec. This fine setting of attenuation values in the magnitude response is easily realizable using FO filters over their IO counterparts. The flexible and precise shaping of FO filter characteristics is an efficient feature which finds applications in many signal processing systems [45], [46], [47].

The design procedures of IO analog filters are well known [48], however obtaining a suitable analytic description, mostly as TF in s -domain, and circuit implementation of a FO filter is a more complex task. For this purpose, the following two approaches are mainly used:

- Numerical search for coefficients of FO TF to minimize the error between the magnitude frequency response of this TF and the selected target function that determines the FO filter requirements over a defined frequency band. In the previous works e.g. the LP Butterworth [44], Chebyshev [49], inverse Chebyshev [50], elliptic [51], arbitrary quality factor [52], flat band-pass (BP) [53], and HP Butterworth [54] target magnitude responses have been approximated by the FO filter TF. Once the resulting coefficients of the FO TF are found, it is then usually realized using a circuit derived from a known IO analog filter, where a classic capacitor is replaced with FOC. As the implementations of FOE are currently being researched intensively and a solid-state FOE is expected to be available soon, it is important to focus on this design approach and to investigate the

utilization of FOE in traditional filter topologies to transform these into fractional order. The author of this thesis also dealt with this type of FO filters and his respective scientific results are presented in Sections 6.1, 6.2, 6.3, 6.4.1, and 6.4.2.

- The second approach approximates the characteristic of FO filter by a higher IO rational TF, which is then implemented by an IO circuit of increased complexity but using classic off-the-shelf elements. The early works, e.g. [55], [56], [57], are based on IO approximation of s^α in the FO TF resulting from the first approach, thus in fact two consecutive approximations are carried out. In the latter works [58], [59], [60], the IO rational approximant is found directly to fit the target characteristic of FO filter. However, the drawbacks here are the limited frequency bandwidth and higher number of components (both active and passive) compared to the first approach. Several author's results concerning this kind of FO filter design are briefly described in Section 6.4.3.

It should be noted that other approaches of obtaining the FO filter TF are also available. Conditions for FO Butterworth TF coefficients based on non-integer order generalization of the Butterworth squared magnitude frequency response are provided in [61]. The design of FO Butterworth-like filter in w -plane is presented and the TF coefficients are given in [62], however, the TF contains more poles and thus more terms in denominator and therefore it leads to more complex circuit realizations. Moreover, the procedure is designed for lower-order Butterworth responses having order just between zero and one. A more general approach is provided in [63], which determines the coefficients of FO TF using the transition bandwidth, stop-band frequency gain, and maximum allowable pass-band peak (and not a particular approximation type). The drawback is that the TF coefficients are not provided explicitly for a sufficient range of the input parameters and require designers to setup their own optimization search routines to calculate the required coefficients.

2.3 Fractional-Order Oscillators

Oscillators, i.e. circuits that generate sinusoidal signals, form an important group of electrical circuits. In most cases, they are designed as second- or third-order circuits, but many FO oscillators have emerged in recent years. These structures are also characterized by the generation of sinusoidal signals at one or more of their outputs, but they provide some specific properties that are not present in classic IO oscillators. This is the possibility of generating signals with extremely high or low frequencies [64], [65], tuning the oscillation frequency by changing the order of the used FOE(s) [66], [67], [68], setting a stepless phase shift of output signals without limitation to integer multiples of 90 degrees [67] – [70], etc. The disadvantage of FO oscillators is the complexity of their mathematical description, especially the relations for the oscillation frequency and the condition [69], [71]. Thus, the design is not simple and many properties, such as electronic adjustment of the oscillation frequency or condition and their effect on the

phase shifts of the output signals, are not investigated in the literature. Basic FO oscillator design techniques are given in [69]. Known second or third order oscillators with standard passive and active elements, such as operational amplifiers, are used here. These structures are transformed into their fractional counterparts by substituting classic capacitor(s) with FO one(s), with the order of the oscillator being reduced from 2 or 3 to slightly lower. Most of the above-cited works use a standard description of FO oscillators based on a characteristic equation. A simpler approach to the design of these circuits may be to use a resonator consisting of a FO capacitor and inductor in combination with a resistor (negative or positive) providing an undamped operation of the resonator [72]. It offers a straightforward way to understand the oscillator operations and logically derive all important design equations in a practically usable form. The author's contribution to the field of FO oscillators is given in Chapter 7.

3. FOE WITH DISTRIBUTED RC LAYERS

Elements with FO impedance, also known as FOEs or simply fractors, are very perspective building blocks for design and implementation of FO circuits and systems. These systems are described by FO differential and integral equations and their analytical description in the Laplace transform contains the non-integer power of the complex variable s . As already mentioned in Section 1.1, the admittance of FOE can be generally written as

$$Y(s) = s^\alpha F_0, \quad (3.1)$$

whereas when $0 < \alpha < 1$ the FOC with its pseudo-capacitance F_0 is concerned and when $-1 < \alpha < 0$ the FOE represents FOI with pseudo-inductance $1/F_0$. From the viewpoint of FO circuit analysis and synthesis, both FOC and FOI can be assumed. However, as the capacitors are preferred instead of inductors in practical IO circuit design, most of the researchers understand under FOE the FOC only.

The idea of realizing impedances with given characteristics by resistive-capacitive (RC) circuits with distributed parameters was put forward already long ago, see e.g. [73], [74]. The synthesis method is based on utilizing homogenous RC lines of the form R-C-0 (resistor-capacitor-conductor) described by voltage-current relations containing hyperbolic trigonometric functions. However, the synthesis of FOE is not considered in the aforementioned works, as well as the problem of its physical realization by film or semiconductor RC lines is not addressed. Therefore, the possibility of FOE synthesis based on R-C-0 lines has been investigated and the physical realization using modern film technologies has been evaluated. It turned out that the implementation is impossible under the existing restrictions on the specific parameters of resistive and dielectric materials, since it leads to element sizes that are comparable with the dimensions of neither ordinary discrete elements, nor integrated circuits. Next to the basic R-C-0 lines, also other types of RC lines were analyzed. As it will be discussed below, the R-C-NR layer structure shows to be suitable for efficient design of FOEs [75], [76], [77]. It contains two resistive layers with resistances R and $N \cdot R$, a capacitive (dielectric) layer with capacitance C between them and four connection terminals as shown in Fig. 3.1.

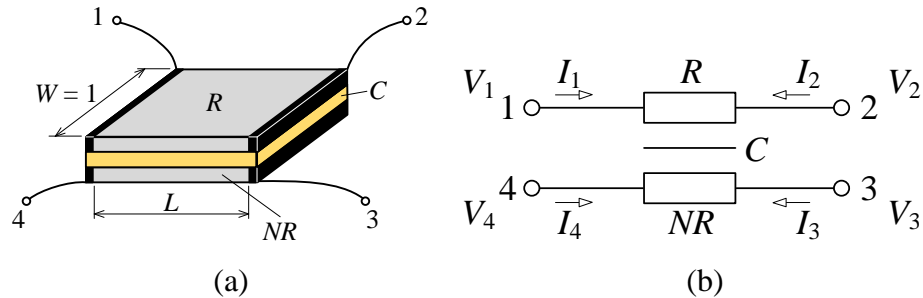


Fig. 3.1 (a) 3D view of R-C-NR structure; (b) its equivalent schematic

Analyzing the structure in Fig. 3.1(b), the relation between the currents I_1, I_2, I_3, I_4 and voltages V_1, V_2, V_3, V_4 can be described using admittance matrix as [78]

$$\begin{bmatrix} I_1 \\ I_2 \\ I_3 \\ I_4 \end{bmatrix} = \frac{1}{(1+N)R} \begin{bmatrix} \frac{\theta}{\tanh \theta} + N & -\frac{\theta}{\sinh \theta} - N & \frac{\theta}{\sinh \theta} - 1 & 1 - \frac{\theta}{\tanh \theta} \\ -\frac{\theta}{\sinh \theta} - N & \frac{\theta}{\tanh \theta} + N & 1 - \frac{\theta}{\tanh \theta} & \frac{\theta}{\sinh \theta} - 1 \\ \frac{\theta}{\sinh \theta} - 1 & 1 - \frac{\theta}{\tanh \theta} & \frac{\theta}{\tanh \theta} + \frac{1}{N} & -\frac{\theta}{\sinh \theta} - \frac{1}{N} \\ 1 - \frac{\theta}{\tanh \theta} & \frac{\theta}{\sinh \theta} - 1 & -\frac{\theta}{\sinh \theta} - \frac{1}{N} & \frac{\theta}{\tanh \theta} + \frac{1}{N} \end{bmatrix} \begin{bmatrix} V_1 \\ V_2 \\ V_3 \\ V_4 \end{bmatrix}, \quad (3.2)$$

where

$$\theta = \sqrt{j\omega RC(1+N)}. \quad (3.3)$$

As the R-C-NR structure has fourth-order admittance matrix, the number of different synthesizable impedances is significantly larger than for RC lines of the form R-C-0. Therefore, a structural-parametric synthesis method of FOE composed of specifically connected four-terminal homogeneous R-C-NR structures (lines) has been developed [75], [79], [80]. This method described in the next section profits from genetic algorithm, is implemented as a computer program and has shown its effectiveness based on practical experience.

3.1 Description of Synthesis Method and Algorithm

The synthesis of any technical object involves creating its structure and determining its parameters. These two parts are called *structural* and *parametric* synthesis. The *structure of the object* determines what physical parts it consists of and how these parts are interconnected. The *parameters of the object* are understood as structural and electrophysical parameters of its parts. We consider the synthesis of FOE based on R-C-NR structures with distributed parameters. Obviously, the *structure* of the element is given by the interconnection of the particular, in this case four, R-C-NR structures resulting in the connection diagram of the FOE components. The *parameters* include the properties of the resistive and dielectric rectangular layers, i.e. their lengths L (relative to the unity width $W = 1$ of all R-C-NR structures) and electrophysical characteristics, such as resistance and capacitance per unit length. Considering that FOE is supposed to be manufactured in one of the known integrated technologies, it is advisable that the electrophysical characteristics of the layers are the same for all the parts of the element.

The synthesis objective is the constant level (with defined error) of the input impedance phase in the range from 0 to -90 degrees. The frequency range of phase constancy, restrictions on the ratio of the resistivity of the top and bottom resistive layers

N , the boundaries of resistance and capacitance per unit length, and fixed values of other parameters in the equivalent circuit model of the RC line, see [75], are set as constraints.

The properties of FOE based on R-C-NR structures are described by a large number of internal factors. For example, there are more than 10 000 variants of connection schemes for four four-terminal R-C-NRs, not including combinations of structural and electrophysical parameters of the layers. Therefore, for such objects it is not rational to use common methods of minimizing objective functions. In such cases the heuristic optimization methods are the most effective, in particular evolutionary algorithms based on the generate-and-test principle. One of these methods is the genetic algorithm (GA) [81], which has been also used here for the synthesis of FOE.

When designing the synthesis method, it was very important to specify the coding of R-C-NR FOE factors appropriately. All these factors that fully and unambiguously describe the design of the structure can be represented by a set Ψ of the form

$$\Psi = \mathbf{P} \cup \mathbf{C}, \quad (3.4)$$

where \mathbf{P} is a set of parametric factors, i.e. the parameters of individual R-C-NR structures. The set \mathbf{C} includes circuit structure factors covering the interconnections of adjacent R-C-NRs and their connection to the overall input nodes of the synthesized FOE denoted as *in* and *gnd*. The set \mathbf{P} can be further defined as

$$\mathbf{P} = \mathbf{N} \cup \mathbf{L}, \quad (3.5)$$

where the sets \mathbf{N} and \mathbf{L} include the values of the parameters N (ratio of the resistivity of the top and bottom layers) and L (relative length of the layers) of each R-C-NR. The set \mathbf{C} can be specified as

$$\mathbf{C} = \mathbf{E} \cup \mathbf{A} \cup \mathbf{B}, \quad (3.6)$$

where the set \mathbf{E} includes valid interconnection schemes of adjacent R-C-NRs, the set \mathbf{A} determines the nodes of adjacent R-C-NRs connected to the *gnd* node, and the set \mathbf{B} defines connections of external terminals of the series of R-C-NR structures to *in* and *gnd* nodes or contains information about their interconnection. Since the program for FOE synthesis has been developed in the MATLAB environment, it is advisable to express the introduced sets of the factors in matrix format. The detailed description of these matrices can be found in [79].

The requirements for the frequency response of the impedance phase of the synthesized FOE are determined in the form of a window as seen in Fig. 3.2. The width of the window determines the frequency range of phase constancy ($\omega_{\min}RC$ to $\omega_{\max}RC$), and its height defines the permissible deviation ($\pm\varepsilon$) from a given level of the constant phase φ_c . Regardless of the shape of the phase response, it is important that all its points fall into this window. Therefore, the easiest way to evaluate the fitness function is to determine the number of the phase response points, which are located within a given window.

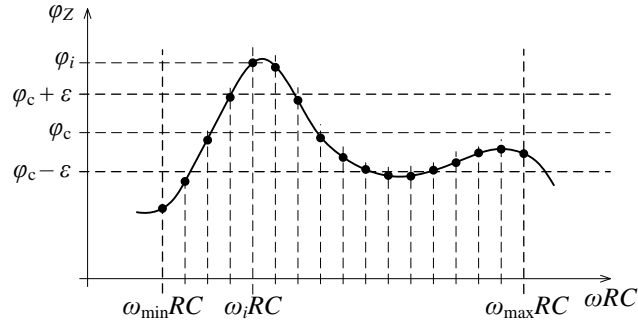


Fig. 3.2 Example of the allowed window of the phase response for fitness function calculation

In this case the fitness function can be specified by the formula

$$Fit = \sum_{i=1}^{M_\omega} \sigma_i, \quad (3.7)$$

where

$$\sigma_i = \begin{cases} 1, & \text{if } |\varphi_c - \varphi_i| < \varepsilon \\ 0, & \text{if } |\varphi_c - \varphi_i| \geq \varepsilon \end{cases} \quad \text{for } \omega_{\min} RC \leq \omega_i RC \leq \omega_{\max} RC, \quad (3.8)$$

φ_i is the value of the impedance phase of the evaluated FOE variant at a frequency $\omega_i RC$, i is the number of the frequency point in the given frequency range from $\omega_{\min} RC$ to $\omega_{\max} RC$; $i = 1, 2, \dots, M_\omega$, whereas M_ω is total number of frequency points. In the example in Fig. 3.2 based on the relation (3.7) we get $Fit = 11$ (with a maximum possible value of 17). The value of φ_i is computed by the methods of circuit theory utilizing the admittance matrix of one R-C-NR structure appearing in (3.2) and parametric and circuit factors given by the sets **P** and **C**.

When developing the general structure of GA, it was considered that the elements of the sets **P** and **C** have different physical nature, different mathematical representations of genes and chromosomes, as well as different algorithms for implementing crossover and mutation operators. Thus, the GA was implemented as multi-stage as seen in the flow-chart of the proposed algorithm in Fig. 3.3. At the beginning of the synthesis, the allowed impedance phase window and the genetic algorithm parameters x , y (maximum number of iterations) and δ (threshold for Fit function) are defined by the user. The program continues with generating random elements of the set **P**. The block “Formation of parental individuals with parameters from the set **C**” deals with creating the initial parental pair by random generation of elements of the set **C** and computing their fitness functions in cycles until two individuals (i.e. parents) are found with the Fit value higher than a threshold specified internally in the program. A similar block “Formation of parental individuals with parameters from the set **P**” is also present in the program which randomly generates elements of the set **P** until their Fit value reaches another internally specified

threshold. The choice of parental individuals ensures initial approach of the fitness function to the optimum and essentially influences the fitness function growth in the following parts of the algorithm.

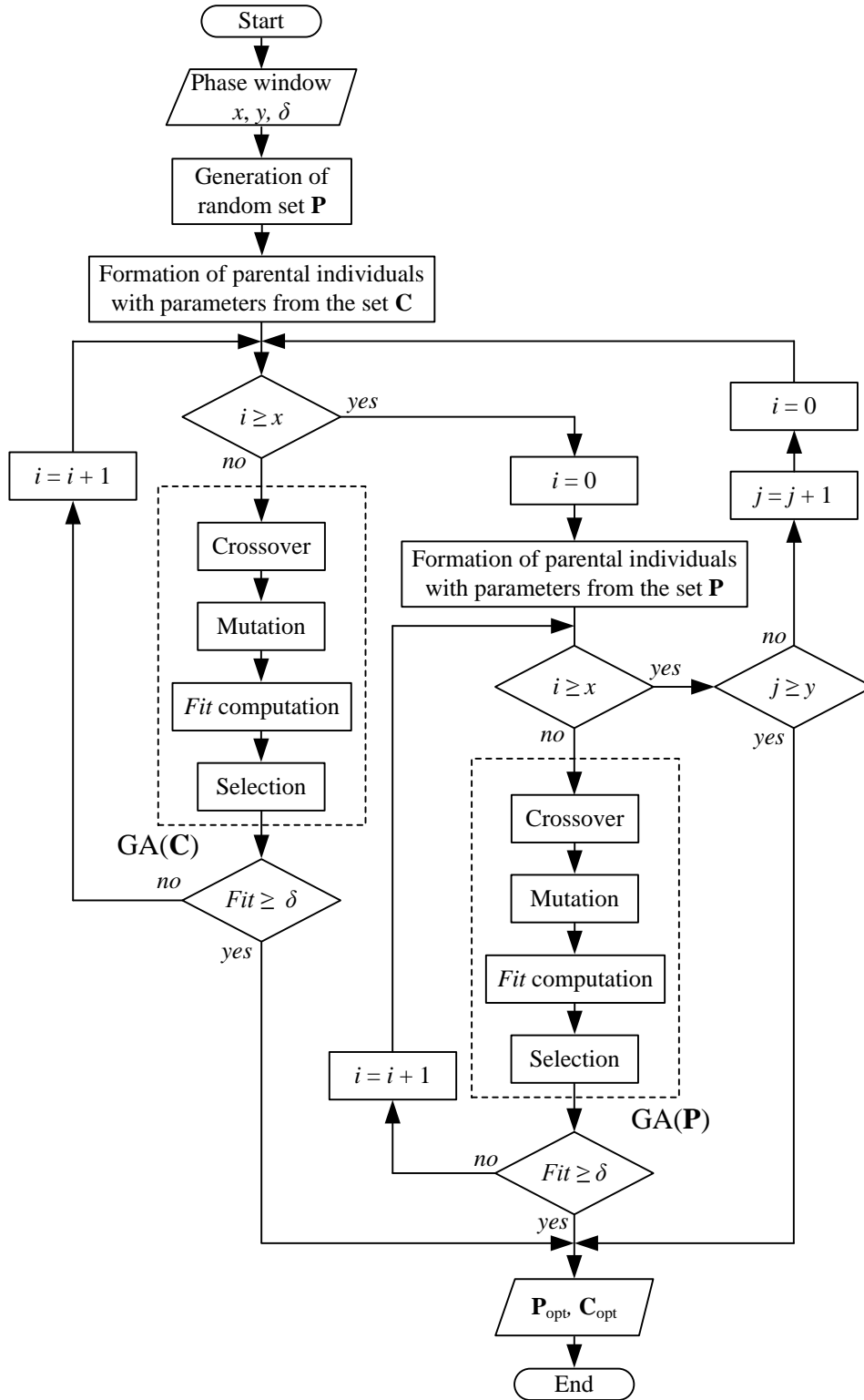


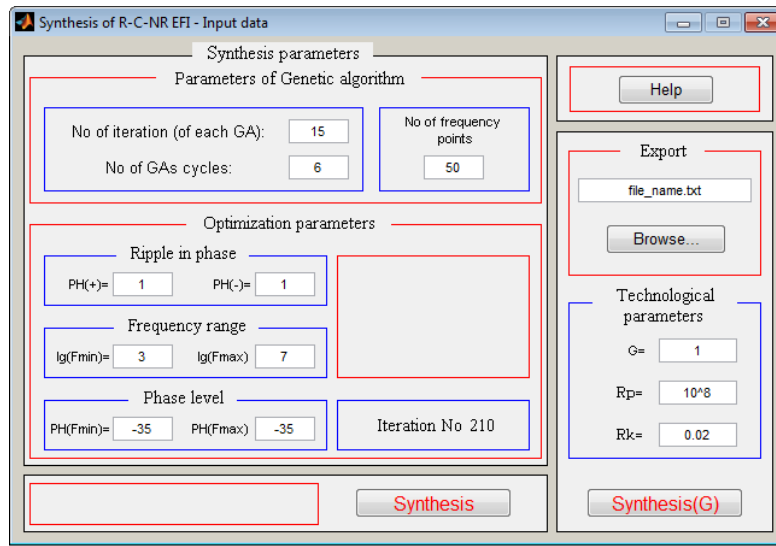
Fig. 3.3 Flow-chart of algorithm for R-C-NR FOE synthesis

From this point the program is divided into two genetic algorithms GA(C) and GA(P). The first one searches for the optimized internal and external connections and the second one deals with optimizing the parametric factors of the R-C-NR FOE. The sets **E**, **A**, and **B**, see (3.6), are processed by GA(C) whereas the parametric factors are unaffected. In the case of GA(P), the sets **N** and **L**, see (3.5), are optimized without altering the connections. The standard blocks “Crossover”, “Mutation”, and “Selection” are included in both of the partial GAs. The algorithm GA(C) and also the whole synthesis program are terminated when the *Fit* value of the two selected individuals reaches a certain threshold δ . For the best results, δ is equal to the total number of frequency points M_ω , hence the user sets M_ω in the user interface. Another condition of termination of GA(C) is reaching a given number of iterations x . In this case the synthesis continues with execution of the algorithm GA(P) with fixed elements of the set **C**. As a result, the optimized parameters of the set **P** are found. The termination conditions of GA(P) are the same as in the case of GA(C). If the algorithm GA(P) is terminated by exceeding the allowed number of iterations x (and *Fit* value does not reach δ) the program proceeds again with GA(C). Both GAs can be alternated in this way up to y times, provided that the *Fit* value still does not reach δ .

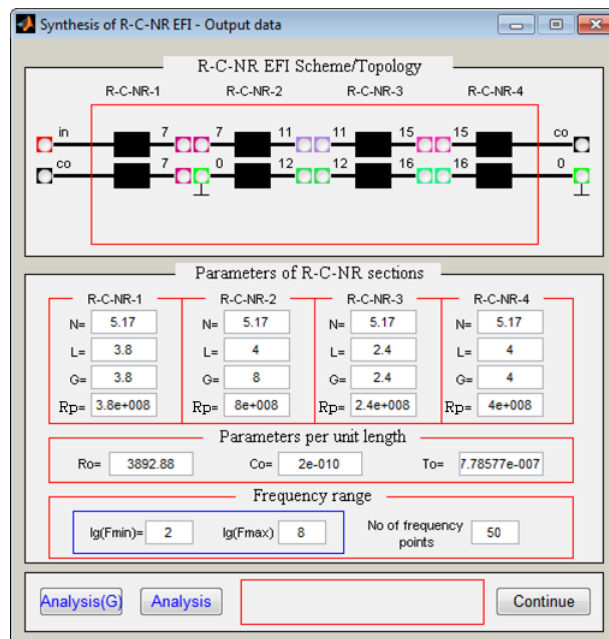
Based on the proposed algorithms, the main program modules and user interface for working with the synthesis program in interactive mode have been developed. The user interface dialog boxes are shown in Fig. 3.4. The dialog box in Fig. 3.4(a) is used to set the requirements for the phase response (in degrees) of the input impedance of the FOE in the form of a window. The window height, i.e. the allowed ripple of the phase response, is set by positive “PH(+)” and negative “PH(–)” deviation from the mean phase value at the respective frequency. The mean phase values at the lower and upper frequency boundaries are given by “PH(Fmin)” and “PH(Fmax)”, respectively. These values are equal for fractional orders that are real numbers. The values “lg(Fmin)” and “lg(Fmax)” are logarithms of lower and upper boundary frequencies (in Hz), which define the frequency range of phase constancy. By setting these values, it is possible to change the frequency bandwidth of the window of the phase constancy and also to shift it along the frequency axis. The values “No of iteration (of each GA)” and “No of GAs cycles” correspond to x and y respectively in Fig. 3.3. The parameter “No of frequency points” specifies the value of M_ω .

The program provides two synthesis modes. The button “Synthesis” executes the synthesis without taking into account the technological parameters, whereas “Synthesis(G)” considers these parameters. The technological parameter “G” is the coefficient of proportionality between the transition resistance between the resistive and capacitive layers and the resistance of the top-layer, “ R_p ” is the leakage resistance of the capacitive layer, and “ R_k ” is the resistance of metal contacts. These parameters are defined for elemental part of the multilayer R-C-NR network as presented in [75]. They depend on the manufacturing technology and therefore their values are to be determined,

for example by experimental measurement of test samples. The values stated here ($G = 1$, $R_p = 10^8$, $R_k = 0.02$) are typical for thick-film technology [82].



(a)



(b)

Fig. 3.4 Dialog windows of the FOE synthesis program; (a) input and (b) output data of synthesis

When one of the conditions for exiting the synthesis program is fulfilled, the dialog box with synthesis results is displayed (Fig. 3.4(b)) along with the impedance phase graph of the synthesized FOE. The displayed frequency range and the parameters of the R-C-NR structures can be changed in this box by user. The synthesis can continue with the changed parameters (but without changing the connections of particular R-C-NR

structures) when Continue is pressed. In addition, this box also provides the possibility of quick analysis of the FOE model with synthesized or user-modified parameters both taking into account the technological parameters “Analysis(G)”, and without taking them into account “Analysis”.

3.2 Verification of Synthesis

The synthesis of FOE based on four R-C-NR sections was carried out for the required constant phase -35° with deviation $\pm 1^\circ$ in the frequency range 1 kHz to 10 MHz and 50 frequency points. The resulting element is described by the topology in Fig. 3.5 and the parameters $N = 5.17$, $L_1 = 3.8$, $L_2 = 4$, $L_3 = 2.4$, $L_4 = 4$. The original generated values of the layer resistance $R_0 = 3893 \Omega$, and capacitance $C_0 = 200$ pF per unity length were modified to the new values $R_0 = 2280 \Omega$, and $C_0 = 77$ pF to obtain more suitable dimensions of the thick-film experimental samples. This modification only shifts the FOE impedance characteristic to 4.4-times higher frequencies without changing its shape. Generally, if the resistance R_0 and capacitance C_0 are changed to the new values $A \cdot R_0$ and $B \cdot C_0$, the impedance characteristic is shifted to $1/(A \cdot B)$ -times higher frequencies without changing its shape.

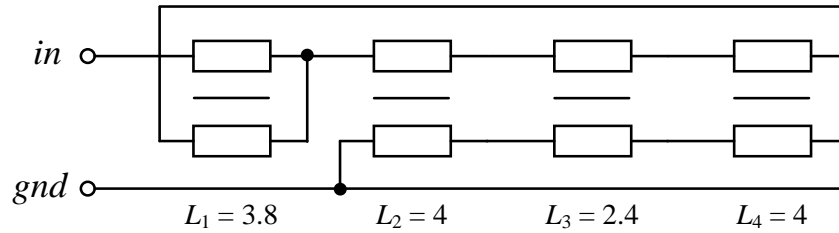


Fig. 3.5 Designed topology of FOE

Based on the materials used within the thick-film technology to implement the required FOE, the final physical length (L_{Fi}) and width (W_{Fi}) of i -th R-C-NR section are defined as follows:

$$L_{Fi} = \sqrt{\frac{R_0 C_0}{R_{sq} C_{sq}}} L_i, \quad W_{Fi} = \sqrt{\frac{R_{sq} C_0}{R_0 C_{sq}}}, \quad (3.9)$$

where R_{sq} and C_{sq} are the sheet resistance (i.e. resistance per square) and capacitance per unit area of the resistive and dielectric inks used for practical realization, respectively. In this case the values are $R_{sq} = 1925 \Omega/\text{sq}$ and $C_{sq} = 4.06$ pF/mm². Using (3.9), the resulting final lengths of the sections are $L_{F1} = 18$ mm, $L_{F2} = 18.95$ mm, $L_{F3} = 11.37$ mm, and $L_{F4} = 18.95$ mm, whereas the width of all sections is $W_F = 4$ mm. The designed FOE was fabricated as a prototype sample [83] in thick-film technology at Brno University of Technology and its photograph is depicted in Fig. 3.6. Note that the sections 3 and 4 are joined together.

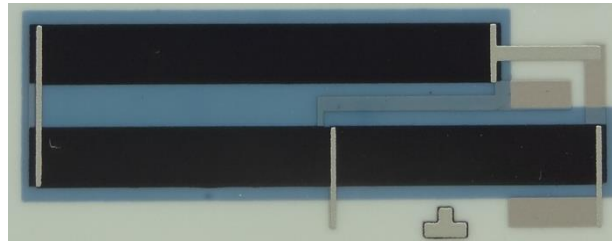


Fig. 3.6 Photograph of the fabricated thick-film FOE sample [83] (dimensions approx. 43x16 mm)

The theoretical FOE phase frequency characteristic displayed by the design program is shown in Fig. 3.7 by black line. The measured characteristic is shown by red color, whereas the blue line shows the simulated phase with the layer resistances and capacitances really achieved in the produced samples. The difference of this simulated (blue) characteristic compared to the synthesized (black) one is caused particularly by the error in the resistance ratio N of the fabricated samples. The measured characteristic matches the simulated one at low frequencies, however the measured phase exhibits parasitic decrease at high frequencies. This phenomenon is primarily caused by parasitic capacitances of the resistive layer contacts which are above each other in the FOE prototype and do not have zero area. To compensate this parasitic effect, the bottom resistive layer was extended by the contact width in order to move the bottom-layer contact and not let it overlap with the top-layer contact.

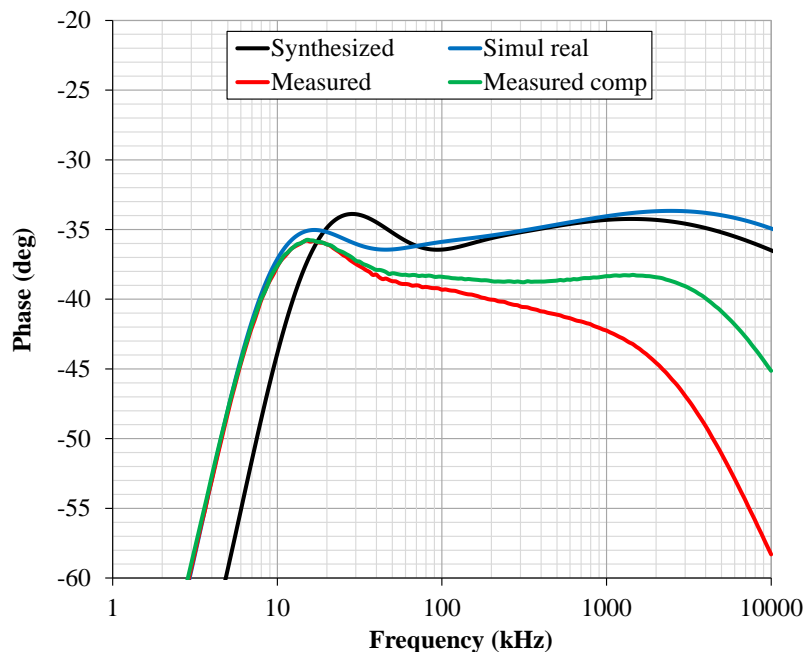


Fig. 3.7 Phase characteristics of the synthesized R-C-NR FOE (black), measured samples (red), simulated with the real properties of the manufactured materials (blue), and measured samples with compensation of contact parasitic capacitances (green)

The modification was practically verified on fabricated samples and resulted in improvement which is confirmed by the green characteristic in Fig. 3.7. The compensated samples show the impedance phase value between -36° to -39° in the frequency band from 8.7 kHz to 3 MHz which is 2.5 decades.

3.3 Conclusions of the Synthesis Method

The principle of FOE synthesis has been proposed, which consists in the use of segments of R-C-NR lines interconnected in a certain way. A description of the synthesis method has been given with explanation of the employed GA. The method allows obtaining physically feasible designs with a range of fractional order α from approximately 0.06 to 0.94, i.e. the phase from 5° to 85° in the operating frequency range 3 to 3.5 decades. The example of FOE has been synthesized with impedance phase characteristics constant at 35° . The validity of the models employed in the synthesis program has been proven by the circuit simulation program and mainly by the experimentally fabricated samples of FOEs using the thick-film technology. The measurements of the test samples show that impedance phase characteristics correspond with sufficient accuracy to the requirements specified during the synthesis and prove the functionality of the proposed design tool.

Although the verification of the synthesis procedure is presented in this thesis by measurements of only one fabricated sample, the presented method has been verified also by other designs of the author and his team, see [75], [80], [84]. In the future, the presented design method is expected to be verified also in thin-film [85] and in CMOS technology [86].

Methods for trimming parameters of the R-C-NR structures were also developed. These methods use two-dimensional models of the structures and a virtual trimming algorithm to design notches interrupting the upper resistive layer at certain locations. After the physical realization of these notches e.g. by laser, the impedance characteristics of the manufactured FOE will be optimized. Details on trimming can be found in the paper [80]. A parametric FOE is also described in [80], enabling the setting of the impedance order (phase) using the ratio N . Although this topic is still in its initial stage, it is very promising, and future research should be directed to the area of the realization of adjustable FOEs using CMOS technology.

4. IMPEDANCE TRANSFORMATIONS OF FOE

The problem with most FOE implementations presented so far is that they do not provide electronic adjustability of their impedance magnitude and phase. As discussed in Section 2.1, FOEs can be emulated by Foster or Cauer structures containing a ladder network of resistors and classic capacitors. However, in the basic form these structures are not adjustable. Changing the input impedance magnitude and phase of these structures would require adjusting all resistance and capacitance values. The author of this work and his team proposed a solution that brings controllability to these passive emulation RC structures in the article [87]. The designed circuit is based on Foster I topology, where the passive elements are replaced by adjustable subcircuits with electronically controllable active elements. The adjustable resistors are implemented by OTAs and the tunable capacitors are implemented using capacitance multipliers which employ Voltage Differencing Current Conveyor (VDCC). The proposed structure provides electronic control of the impedance order and electronic shifting of the frequency band of the emulation validity.

Another solution to get adjustable FOE is to use an impedance converter with active elements. This block transforms the impedance of the connected FOE(s) to obtain a required value of its input impedance at specific frequency. In this context, the author of this work dealt with impedance magnitude transformations of FOEs using two-operational-amplifier GIC as described in [88]. Of greater importance are then the author's works on the design of OTA-based gyrator implementing FO inductance simulator, impedance transformations resulting in FOE of complementary order, and the use of GIC to obtain series of FOE values. These topics are described in more detail in the following sections.

4.1 Gyrator-Based FO Inductor

Although mainly capacitive FOEs are being developed and used, inductive FOEs (FOIs or inductive fractors) are also required in many FO circuits. Let us mention e.g. electrical equivalent models of biological tissues [10], parallel and series FO LC resonators [72], [89], [90], FO frequency filters [91], [92]. The FOIs can be emulated by e.g. Foster or Cauer ladder circuits consisting of resistors and classic inductors [93]. However, implementation of inductors by classic passive coils is currently being avoided due to their shortcomings, such as bulky dimensions, complicated fabrication, incompatibility with integrated technologies, low quality factor and other parasitic electrical properties.

Assuming a solid-state FOC is expected to be available soon, it is advisable to design FOI by connecting such a FOC to a circuit that provides immittance inversion which is the case of gyrator, immittance inverter or GIC [94]. The convenient solution is a gyrator which can employ only two OTAs offering precise and broadband characteristics thanks

to recent improvements in CMOS technologies. In addition, OTAs allow electronic adjustability of the resulting synthetic inductance. The following part of this section is based on the articles [95] and [96] by the author of this thesis.

Ideal OTA (Fig. 4.1) is a voltage-controlled current source defined by the following relation

$$i_{\text{OUT}} = g_m (v_+ - v_-), \quad (4.1)$$

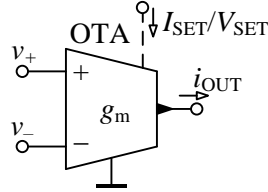


Fig. 4.1 Schematic symbol of OTA

where g_m is the transconductance which is commonly adjustable by an external dc current I_{SET} or dc voltage V_{SET} . The internal impedance of input and output terminals of an ideal OTA is infinity. The schematic of the gyrator employing two OTAs is shown in Fig. 4.2 [5].

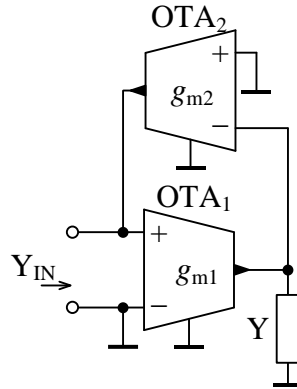


Fig. 4.2 OTA-based gyrator

The input admittance of the circuit can be written as:

$$Y_{\text{IN}} = \frac{g_{m1}g_{m2}}{Y}. \quad (4.2)$$

Assuming transformation of FOC with $Y(s) = s^\alpha F$ and $0 < \alpha < 1$, the resulting input admittance is

$$Y_{\text{IN}}(s) = \frac{g_{m1}g_{m2}}{s^\alpha F}, \quad (4.3)$$

which represents admittance of FOI with the following magnitude and phase:

$$Y_{IN}(j\omega) = \frac{g_{m1}g_{m2}}{\omega^\alpha F} \angle -\frac{\alpha\pi}{2}. \quad (4.4)$$

Since it is not possible to produce perfectly ideal active elements, it is suitable to analyze the influence of parasitic properties of OTA on the gyrator function transforming capacitive fractor to inductive one. The deviations of the magnitude and phase impedance characteristic are investigated and the guidelines for minimizing these errors are given. Also steps for optimal utilization of OTA dynamic range are stated below.

4.1.1 Influence of OTA Terminal Impedances

Real properties of OTA are usually modeled by shunt resistances and capacitances of the input and output terminals. Input resistance can be very large, especially in CMOS technology, whereas input capacitance is typically tens of femtofarads. Output resistance reaches usually several hundreds of kilohms and output capacitance up to a few hundreds of femtofarads [97]. Considering these parasitic properties of OTA, the gyrator schematic can be modified to the form in Fig. 4.3.

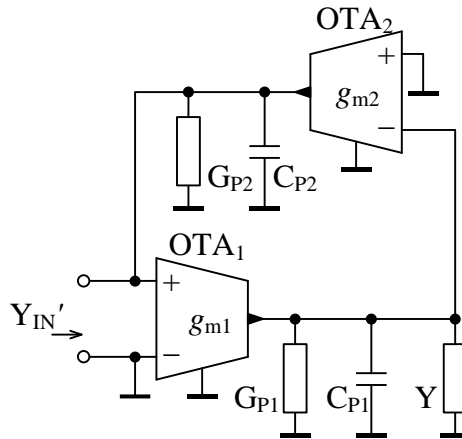


Fig. 4.3 Gyrator with OTA parasitic properties

The parasitic properties of OTA₁ output and OTA₂ input are together modeled with G_{P1} and C_{P1} . The parasitics of OTA₁ input and OTA₂ output are modeled with G_{P2} and C_{P2} . The relation for gyrator input admittance considering the OTA parasitic properties and loading the gyrator with FOC instead of the element Y is

$$Y_{IN}'(s) = \frac{g_{m1}g_{m2}}{s^\alpha F + G_{P1} + sC_{P1}} + G_{P2} + sC_{P2}. \quad (4.5)$$

To illustrate the meaning of (4.5) the passive circuit with the identical input admittance $Y_{IN}'(s)$ can be drawn in Fig. 4.4. Analyzing (4.5) and Fig. 4.4, the FOC connected to the gyrator is transformed to FOI with admittance $g_{m1}g_{m2}/(s^\alpha F)$ which is in accordance with the relation for ideal case (4.3). Naturally the parasitics C_{P1} and G_{P1} are also transformed by the gyrator and they appear in the structure in Fig. 4.4 as inductor

with admittance $g_{m1}g_{m2}/(sC_{P1})$ and resistor with admittance $g_{m1}g_{m2}/G_{P1}$. The elements G_{P2} and C_{P2} appear directly at the input of the whole structure and thus their admittance is an additive part of the overall input admittance $Y_{IN}'(s)$.

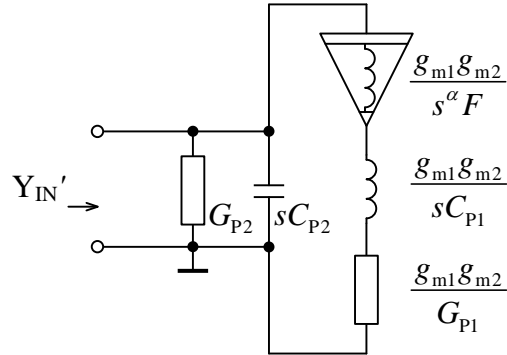


Fig. 4.4 Passive circuit with the input admittance (4.5); the relations in the schematic express admittances of the particular elements

Considering the aforementioned typical values of the OTA parasitic properties, the form of the admittance magnitude and phase frequency characteristics resulting from (4.5) can be depicted by the asymptotic Bode plots in Fig. 4.5. At low frequencies the input admittance is real and its magnitude has a constant value $g_{m1}g_{m2}/G_{P1}$ (when neglecting G_{P2} which is much lower). This parasitic behavior with limited admittance magnitude and zero phase persists up to the frequency

$$\omega_{GP1} \approx \left(\frac{G_{P1}}{F} \right)^{\frac{1}{\alpha}}. \quad (4.6)$$

Above this frequency the admittance of the inductive fractor in Fig. 4.4 is lower than $g_{m1}g_{m2}/G_{P1}$ and the operation of the gyrator can be considered correct, i.e. approximately providing admittance of FOI (4.3), which is marked by the red line in Fig. 4.5. The magnitude of the gyrator input admittance drops with the slope -20α dB/dec and the phase is $-\alpha\pi/2$. Note that the admittance characteristics of an ideal inductive fractor can be obtained by linear extension of the red traces in Fig. 4.5 throughout the whole frequency range. The correct behavior of the gyrator may end at the frequency

$$\omega_{GP2} \approx \left(\frac{g_{m1}g_{m2}}{G_{P2}F} \right)^{\frac{1}{\alpha}}, \quad (4.7)$$

where the input admittance magnitude decreases to G_{P2} . Above this frequency, the input admittance has again real character with the magnitude G_{P2} . Further, above the frequency

$$\omega_{CP2} \approx \frac{G_{P2}}{C_{P2}} \quad (4.8)$$

the influence of the parasitic capacitance C_{P2} prevails and the admittance Y_{IN}' has purely

capacitive character which is far away from the desired FO inductor. As shown in Fig. 4.5 by the dashed part of characteristic, it may happen that at the frequency

$$\omega_{CP2}' \approx \left(\frac{g_{m1}g_{m2}}{C_{P2}F} \right)^{\frac{1}{\alpha+1}} \quad (4.9)$$

the FO admittance $g_{m1}g_{m2}/(s^\alpha F)$ equals to the admittance sC_{P2} while the conductance G_{P2} is lower than both of the admittances. In this case the FO inductance produced at the input port of the gyrator resonates with the parallel parasitic capacitance C_{P2} . This resonance can be potential source of instability. Analysis of (4.5) shows that the real part of Y_{IN}' can never decrease below G_{P2} which means that this parasitic element positively impacts the stability of the structure in Fig. 4.3.

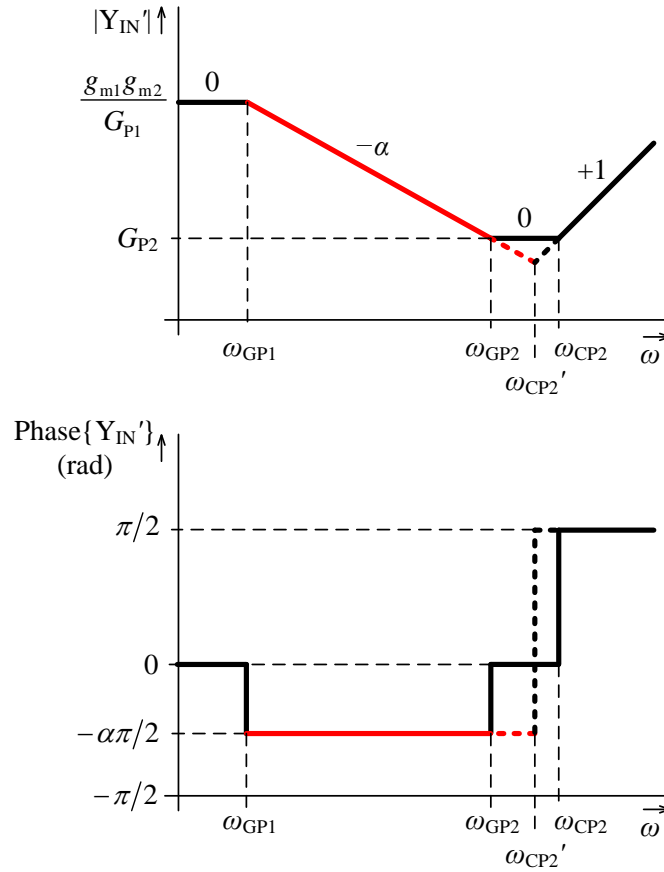


Fig. 4.5 Bode magnitude and phase admittance characteristics expressing (4.5) (the values at the magnitude characteristic denote the order of the admittance in the respective frequency band)

The classic inductor in Fig. 4.4 arising from immittance inversion of C_{P1} has usually negligible effect on the gyrator input admittance. Its contribution can be in decreasing the input admittance at frequencies above ω_{CP2} , however in this band the input admittance is increased by C_{P2} which outweighs.

The following recommendations can be drawn from the previous analysis to improve the performance of the gyrator mainly as far as operation bandwidth, and range of obtainable admittance magnitude are concerned:

- If there is a possibility to modify the fractance F , increase the values of both $(g_{m1}g_{m2})$ and F such that the ratio $(g_{m1}g_{m2})/F$ remains constant. This decreases the lower cut-off frequency ω_{GP1} , and thus, expands the band of correct operation of the gyrator to lower frequencies without affecting the FO inductance. Moreover, the maximum obtainable magnitude of input admittance $g_{m1}g_{m2}/G_{P1}$ increases.
- From the OTA parasitic properties, the main effort should be to decrease G_{P1} , which also brings a decrease of ω_{GP1} and an increase of maximum input admittance magnitude. Adherence to the recommendation on decreasing G_{P1} will also efficiently increase ω_{GP2} , as due to the gyrator topology, we may assume $G_{P1} \approx G_{P2}$. This can be achieved by choosing an OTA structure that offers low parasitic conductance at input and output terminals. An alternative way to reduce a parasitic conductance in the gyrator is connecting a negative conductance in parallel as described in the author's article [96]. To further optimize the gyrator operation at high frequencies in terms of increasing ω_{CP2} , it is recommended to choose an OTA structure with low C_{P2} .

It is also interesting that for lower values of α , the bandwidth of the correct operation is widened which is related to the lower steepness of the admittance magnitude characteristic. Thus, a gyrator implementing a FOI has a higher bandwidth than a gyrator implementing a classic inductor.

4.1.2 Dynamic Properties

Next to the non-ideal frequency analysis, it is also important to investigate the dynamic properties of the gyrator such that the amplifiers operate in linear mode and the maximum voltage and current values of their terminals are not exceeded. As far as common OTAs are concerned, the most limiting is the non-linearity of their input transistor stage, which takes effect already at differential input voltages of several tens of millivolts. Let us denote the maximum allowed amplitude of OTA input voltage for linear operation $V_{OTA,MAX}$. The output drive current of OTA is also limited to a maximum value $I_{OTA,MAX}$; whereas, it holds $I_{OTA,MAX} = g_m V_{OTA,MAX}$. The value of $V_{OTA,MAX}$, and also maximum allowable transconductance g_m can be determined from the respective OTA documentation. The following two conditions must be met to avoid the non-linear operation of the gyrator:

- The gyrator input voltage V_{IN} must not be higher than the allowed input voltage range of OTA₁ $V_{OTA1,MAX}$

$$V_{IN} \leq V_{OTA1,MAX} \quad (4.10)$$

- The second condition for V_{IN} provides that the voltage swing across the gyrator

loading admittance Y does not exceed the maximum possible OTA₂ input voltage $V_{\text{OTA2,MAX}}$

$$V_{\text{IN}} \leq \frac{g_{m2} V_{\text{OTA2,MAX}}}{|Y_{\text{IN}}|} \quad (4.11)$$

Apparently, the allowed V_{IN} according to (4.11) changes with frequency. It reaches the minimum value at the lowest operating frequency where $|Y_{\text{IN}}|$ is maximal. It can be concluded that the gyrator input voltage V_{IN} must meet both the conditions (4.10) and (4.11) simultaneously when the linear operation of both OTAs is required. If the conditions for maximum gyrator input current I_{IN} are required, they can be easily derived from (4.10) and (4.11) by substituting $V_{\text{IN}} = I_{\text{IN}}/|Y_{\text{IN}}|$.

Practical guidelines for gyrator parameter design were compiled based on the above observations. For those interested they are available in the work [96]. By following these rules, in addition to the correct input admittance, the highest possible frequency and magnitude range of the gyrator are ensured and the active elements are prevented from non-linear operation and overloading.

If the OTA₂ with differential (balanced) output is available, it is possible to easily obtain a differential gyrator with floating input as also demonstrated in the author's work [96].

4.1.3 Simulation Results and Concluding Remarks

To verify the results presented in the Subsection 4.1.1, the computer simulation of the input admittance of the gyrator was carried out using OrCAD software. The parasitic properties were chosen $1/G_{P1} = 1/G_{P2} = 346 \text{ k}\Omega$, $C_{P1} = C_{P2} = 0.28 \text{ pF}$, which is in accordance with the CMOS OTA cell introduced in the work [97]. The OTA transconductances are $g_{m1} = g_{m2} = 1 \text{ mS}$. A total of four loading admittances Y were employed with identical magnitude $|Y| = 1 \text{ mS}$ at 1 kHz and different $\alpha = 0.25, 0.5, 0.75, 1$, i.e. three of them FO and one classic capacitor. The respective values of the fractance F are $112 \text{ }\mu\text{F}\cdot\text{s}^{-0.75}$, $12.6 \text{ }\mu\text{F}\cdot\text{s}^{-0.5}$, $1.42 \text{ }\mu\text{F}\cdot\text{s}^{-0.25}$, 159 nF . The simulation results are depicted in Fig. 4.6.

The characteristics with solid lines were obtained using ideal FOCs modeled in OrCAD by GFREQ controlled source with interconnected input and output, similar to OTA-based resistor. For more details on the ideal FOC modeling by the GFREQ block see Subsection 6.1.3. The solid-line characteristics in Fig. 4.6 are in accordance with the Bode plots in Fig. 4.5. The important cut-off frequencies and asymptotic magnitude and phase values are confirmed by the simulations. The limited frequency band of the correct functionality of the gyrator can be observed. The maximum admittance magnitude at low frequencies reaches $g_{m1}g_{m2}/G_{P1} = 346 \text{ mS}$ in all cases. The constant magnitude section between ω_{GP2} and ω_{CP2} is not apparent in the simulations as the value $G_{P2} = 0.0029 \text{ mS}$ is

too low to take effect. It is also confirmed that the bandwidth of correct operation increases as α decreases.

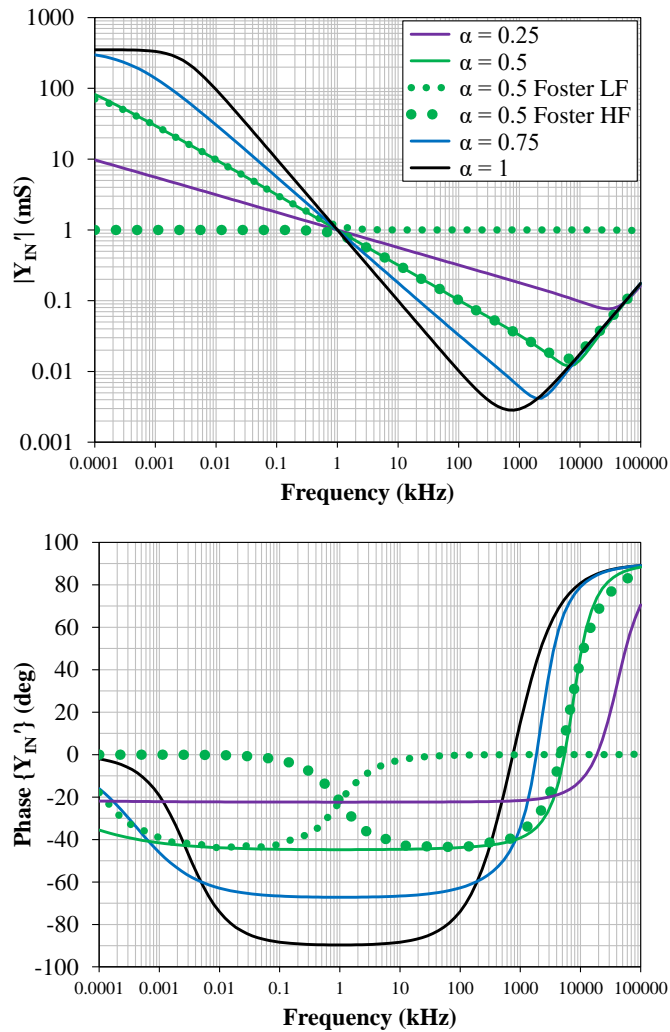


Fig. 4.6 Simulated magnitude and phase characteristics of gyrator input admittance

The simulations with FOC emulated by 5th order Foster I structure containing standard resistors and capacitors computed for Oustaloup approximation [25] are also presented in Fig. 4.6 by dotted lines. Only the case with $\alpha = 0.5$ was chosen to maintain clarity of the graph. Two different emulators of FOC were used, as covering the whole gyrator operating bandwidth which is more than seven decades would require a very complex emulator structure. Thus, the first emulator covers the frequency range 0.1 Hz to 1 kHz (marked with smaller dots in Fig. 4.6) and the second one 1 kHz to 10 MHz (marked with larger dots in Fig. 4.6). The schematic and values of resistors and capacitors of the Foster I emulator can be found in [95]. The dotted characteristics in Fig. 4.6 simulated with the emulated FOC exhibit an additional error compared to the solid green characteristic obtained using ideal FOC. The operational frequency band of the emulator is lower than the bandwidth of the gyrator with ideal FOC and considering only the real

OTA properties. Thus, the bandwidth of the FOC is a limiting factor of the total bandwidth of the gyrator.

To conclude, the immittance inversion by gyrator is suitable for obtaining FOIs as they are not as easy to manufacture in passive form as FOCs. Nevertheless, this approach has limitations caused by the active element real properties, affecting mainly the operational bandwidth, range of the obtainable input admittance and dynamic range. While designing the gyrator circuit it is essential to set sufficiently large OTA transconductances. This leads also to large fractance F , which reduces the circuit sensitivity to the parasitics G_{P1} and C_{P1} .

The Section 4.1 is based mainly on the findings of the paper [95]. As already referenced, a significant extension of this topic can be found in the author's article [96], where, for example, the compensation of parasitic conductance of OTA terminals by means of a shunt negative resistor realized by a specially connected OTA is practically shown. Furthermore, the dynamic optimization following the rules introduced in the Subsection 4.1.2 is also performed in the article. The step-by-step guidelines for the design of gyrator parameters, including the flowchart, the floating gyrator variant, and practical design of FOI for an electrical model of the human respiratory system are also demonstrated in [96].

4.2 FOE of Complementary Order

Wider possibilities of FOE immittance transformations in comparison with the gyrator described in Section 4.1 are presented in articles [98] and [99], in which the author of this thesis also participated. Transformation of FOEs and their fractional order α to obtain the complementary order $\beta = 1 - \alpha$ is demonstrated there. The transformation also allows to obtain capacitive and/or inductive FOEs with adjustable pseudo-capacitance and/or pseudo-inductance, which results in significant reduction of the required FOEs or their RC emulators in a final circuit, where the feature of tunability and adjustability is required. Furthermore, FO frequency-dependent negative resistors of type I (FDNR-I) or fractional D elements specified with D parameter [100] can be obtained using the approach.

Assume GIC as shown in Fig. 4.7 containing three admittances $Y_1 - Y_3$ as passive elements and a network of generally arbitrary types of active elements.

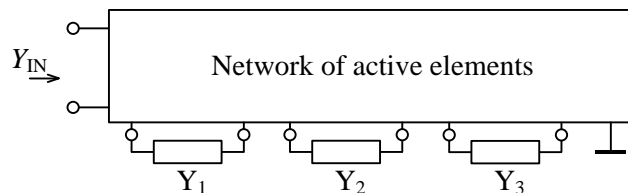


Fig. 4.7 General view on immittance converter

Let the input admittance Y_{IN} of this GIC be defined as

$$Y_{\text{IN}} = \frac{Y_2 Y_3}{Y_1}. \quad (4.12)$$

Selecting the specific types (i.e. resistor, capacitor and/or FOE) of the individual admittances $Y_1 - Y_3$, the following transformation cases can be described:

- **Case I:** $Y_1 = s^\alpha F_\alpha$, $Y_2 = sC$, $Y_3 = G$

$$Y_{\text{IN1}} = s^\beta \frac{CG}{F_\alpha}, \quad (4.13)$$

and FOC with complementary order $\beta = 1 - \alpha$ and pseudo-capacitance CG/F_α is obtained.

- **Case II:** $Y_1 = G_1$, $Y_2 = s^\alpha F_\alpha$, $Y_3 = G_2$

$$Y_{\text{IN2}} = s^\alpha \frac{F_\alpha G_2}{G_1}, \quad (4.14)$$

and the FO capacitance multiplier is designed with the multiplication constant G_2/G_1 , whereas the fractional order remains unchanged.

- **Case III:** $Y_1 = s^\alpha F_\alpha$, $Y_2 = G_1$, $Y_3 = G_2$

$$Y_{\text{IN3}} = \frac{G_1 G_2}{s^\alpha F_\alpha}, \quad (4.15)$$

and the synthetic FOI is designed with the order α and its pseudo-inductance $F_\alpha/(G_1 G_2)$.

- **Case IV:** $Y_1 = sC$, $Y_2 = s^\alpha F_\alpha$, $Y_3 = G$

$$Y_{\text{IN4}} = \frac{F_\alpha G}{s^\beta C}, \quad (4.16)$$

and the FOI with complementary order $\beta = 1 - \alpha$ and pseudo-inductance $C/(F_\alpha G)$ is obtained.

- **Case V:** $Y_1 = s^\alpha F_\alpha$, $Y_2 = sC_1$, $Y_3 = sC_2$

$$Y_{\text{IN5}} = s^{2-\alpha} \frac{C_1 C_2}{F_\alpha}, \quad (4.17)$$

and the FO FDNR-I with its order $(2 - \alpha)$ and the parameter $D = C_1 C_2 / F_\alpha$ is defined.

- **Case VI:** $Y_1 = G$, $Y_2 = s^\alpha F_\alpha$, $Y_3 = sC$

$$Y_{\text{IN6}} = s^{1+\alpha} \frac{F_\alpha C}{G}, \quad (4.18)$$

and again, the FO FDNR-I as in Case V is obtained, however here its fractional

order is $(1 + \alpha)$ and the parameter $D = F_\alpha C/G$.

Assuming that only one discrete FOE is expected to be employed in the transformation cell, generally the Case VII can be defined for $Y_1 = sC_1$, $Y_2 = s^\alpha F_\alpha$, $Y_3 = sC_2$. In this case, however, the definition of input impedance is given by (4.14) and fractional capacitor multiplier is designed again, just the multiplication constant is C_2/C_1 . Note that all the Cases described above assume at most one FOE. Using more FOEs, other design cases of passive synthetic elements can be defined, but are not analyzed here.

It is evident that for each of the possible design Cases described above the required fractional order and/or the value of the pseudo-capacitance, pseudo-inductance or pseudo- D can be adjusted by properly selecting the parameters of the passive elements. Note that for Cases I – IV, the general admittance Y_3 has the character of a basic conductor (i.e. G). Hence, OTA element defined with its adjustable transconductance g_m can be advantageously used for the design of the transformation cell, as it offers electronic adjustability of the pseudo-capacitance or pseudo-inductance of the final FOE. Furthermore, the Cases I and IV show that FOEs of fractional order β being complementary to the original fractional order α of the assumed capacitive FOE are obtained. Hence, for the practical design and mainly in case of implementing the FO function blocks as integrated circuits, significantly reduced number of FOEs is required to offer sufficient tunability and adjustability.

4.2.1 Implementation by GIC

The above described theory of transforming FOEs is verified using the immittance converter. To follow the advantage of electronic adjustability of the final FO synthetic elements, the operational transconductance amplifier (OTA), see Fig. 4.1 and equation (4.1), is employed in this converter. The second active element used is a simple second-generation current conveyor CCII (Fig. 4.8), whose behaviour is defined by the following relations for terminal currents and voltages: $i_Y = 0$; $v_X = v_Y$; $i_Z = i_X$.

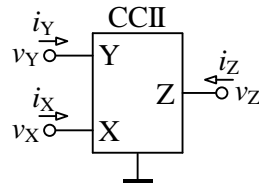


Fig. 4.8 Schematic symbol of CCII

Using the OTA and CCII as active elements, the GIC as shown in Fig. 4.9 can be used and its input admittance can be expressed as

$$Y_{IN} = \frac{Y_2 g_m}{Y_1}. \quad (4.19)$$

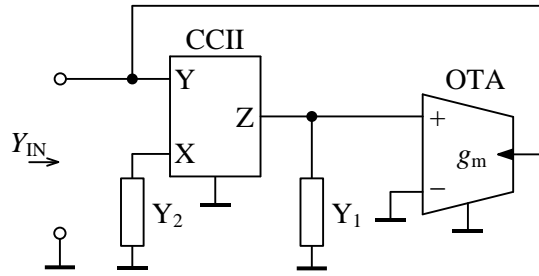


Fig. 4.9 General immittance converter using CCII and OTA as active elements

This relation corresponds to (4.12) assuming that $Y_3 = g_m$. Selecting the type of the admittances Y_1 and Y_2 according to the Cases I – IV as described above, the grounded FOC or FOI with the order α or β ($\beta = 1 - \alpha$) and adjustable pseudo-capacitance or pseudo-inductance can be designed.

The Cases I and II of transforming discrete FOE are further analyzed through simulations and also experimental measurements in the article [99]. For this purpose, the Foster I RC network emulating FOC with fractional order $\alpha = 0.2$ is utilized. The active elements in the GIC were implemented using commercially available AD844 circuits [101]. It has been practically proven that with the help of GIC it is possible to electronically adjust the pseudo-capacitance by setting the transconductance g_m without affecting the fractional order $\alpha = 0.2$ or $\beta = 1 - 0.2 = 0.8$. See the article [99] for more details on verifying the functionality of the circuit in Fig. 4.9.

4.3 FOE Series Using GIC

This section further expands and generalizes the possibilities of FOE impedance transformations. It builds on the findings from the previous Section 4.2, while the GIC of Fig. 4.7 is further expanded in order to obtain greater variability of input admittances. This approach enables an efficient design of FOE series while using a very limited set of “seed” FOEs. The author’s works [102], [103] dealing with this topic show the use of only up to two “seed” FOEs with properly selected fractional order α_{seed} (the same order for both FOEs) as passive elements that results in the design of a series of 17 synthetic FOEs with different α being in the range $[-2; 2]$.

The final extension of these transformations is described by the author and his team in the article [24], on which this extensive Section 4.3 is based. A concept to efficiently design a series of floating synthetic FOEs using GIC is proposed here. Using even single or a very limited number of “seed” FOEs it is possible to obtain a wide set of new FOEs featuring fractional order α being in the range $[-p; p]$, where p is arbitrary integer number. The concept is further developed by proposing a general circuit structure of the GIC that employs OTAs as active elements. To show the efficiency of the proposed technique, the use of only up to two “seed” FOEs with properly selected fractional orders as passive elements results in the design of a series of 51 FOEs with different α being in the range

$[-2; 2]$. Comprehensive analysis of the proposed GIC is given including effect of parasitic properties of active elements and optimization process to improve the overall performance.

Assume a general function block as shown in Fig. 4.10 that is represented by general active/passive network to which general admittance elements Y_i ($i = 1, \dots, p$; p being even number) are connected. The general active/passive network may represent arbitrary interconnection of an arbitrary type of active and passive elements and is determined by its parameter g , a transconductance specific for this active/passive network.

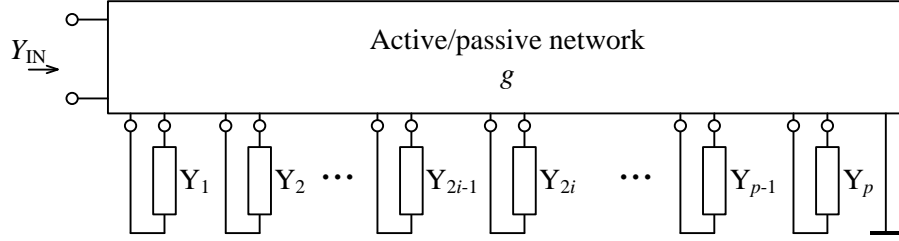


Fig. 4.10 View on general immittance converter as a function block

Let the input admittance Y_{IN} of such a general function block be defined as

$$[Y_{IN}] = \begin{bmatrix} 1 & -1 \\ -1 & 1 \end{bmatrix} \frac{\prod_{i=1}^{p/2} Y_{(2i)}}{\prod_{i=1}^{p/2} Y_{(2i-1)}} g. \quad (4.20)$$

The general admittances Y_i ($i = 1, \dots, p$) may be represented by any type of passive element, such as conductor (i.e. resistor), inductor, capacitor, and FOE with their fractional orders α_i equal to 0, -1 , 1, and α_{FOE} ($-1 < \alpha_{FOE} < 0$ or $0 < \alpha_{FOE} < 1$), respectively, in accordance with the admittance format (3.1). Under these assumptions, for the fractional order α defining the phase angle of the input admittance (4.20) can be written

$$\alpha = \sum_{i=1}^{p/2} \alpha_{(2i)} - \sum_{i=1}^{p/2} \alpha_{(2i-1)}. \quad (4.21)$$

and the feasible range of fractional order α is defined as $[-p, p]$. To better demonstrate the advantageous features of the proposed concept of designing a series in fractional order α of FOEs, let $p = 4$. Then (4.20) and (4.21) simplify to:

$$[Y_{IN}] = \begin{bmatrix} 1 & -1 \\ -1 & 1 \end{bmatrix} \frac{Y_2 Y_4}{Y_1 Y_3} g, \quad (4.22)$$

and

$$\alpha = \alpha_2 + \alpha_4 - \alpha_1 - \alpha_3, \quad (4.23)$$

respectively.

As in practical analog circuit design, classic inductors, and/or inductive fractors are not commonly used, in the further text it is assumed that the general admittance elements Y_i may be replaced only by conductors ($\alpha_i = 0$), capacitors ($\alpha_i = 1$), and/or capacitive FOEs ($\alpha_i = \alpha_{\text{FOE}}$, $0 < \alpha_{\text{FOE}} < 1$). Consequently, the following set of synthetic passive elements observed at the input of the immittance converter and specific with their fractional order α can be described:

- Frequency-dependent negative resistor - type I (FDNR-I), $\alpha = 2$,
- Fractional FDNR-I, $1 < \alpha < 2$,
- Capacitor C, $\alpha = 1$,
- Capacitive FOE, $0 < \alpha < 1$,
- Resistor R, $\alpha = 0$,
- Inductive FOE, $-1 < \alpha < 0$,
- Inductor L, $\alpha = -1$,
- Fractional frequency-dependent negative resistor - type II (FDNR-II),
 $-2 < \alpha < -1$,
- FDNR-II, $\alpha = -2$.

Note that the feasible range of fractional order α is now $[-2, 2]$ only, which is caused by the fact that neither classic nor fractional inductors are assumed to replace one or more general admittance elements Y_i .

The frequency-dependent negative resistor-type I (FDNR-I) is also referred to as the *D* element (or double capacitor) and features purely real negative resistance that decreases in magnitude with increasing frequency [100], whereas FDNR-II also exhibits purely real negative resistance, however, its magnitude increases for increasing frequency. Additionally, comparing with [42], the inductive FOE, fractional FDNR-II, fractional FDNR-I, and capacitive FOE, may be referred to as Type-I fractor, Type-II fractor, Type-III fractor, and Type-IV fractor, respectively.

Using GIC allows to obtain a wide series of new FOEs using a very limited set of “seed” FOEs and their fractional order α_{seed} . As an example, assume a “seed” FOE with fractional order $\alpha_{\text{seed}} = 0.2$. Using always at most two identical “seed” FOEs and two capacitors together with conductors to replace external admittance elements Y_i ($i = 1, \dots, 4$) in (4.22), then according to (4.23) 19 unique values of fractional order α from the range $[-2, 2]$ are obtained. The combinations of external passive elements, i.e., of the conductors, capacitors, and “seed” FOEs, are listed in Tab. 4.1 in terms of their α_i values.

To better comprehend the advantage in utilizing “seed” FOEs, even 51 different values of fractional order α , still from the range $[-2, 2]$, can be obtained by assuming two different order values $\alpha_{\text{seed1}} = 0.25$ and $\alpha_{\text{seed2}} = 0.0625$. As a result, for each α , the input admittance Y_{IN} given by (4.22) features a phase angle from the range $[-180, 180]$ degrees as illustrated in Fig. 4.11. The specific combinations of external admittance types defined by their α_i are summarized in Tab. 4.2.

Table 4.1 Combinations of admittances Y_i , their α_i and the unique fractional order α of Y_{IN} for $\alpha_{seed} = 0.2$

α_1	α_2	α_3	α_4	α
0	1	0	1	2
0.2	1	0	1	1.8
0.2	1	0.2	1	1.6
0	1	0	0.2	1.2
0	1	0	0	1
0.2	1	0	0	0.8
0.2	1	0.2	0	0.6
0	0.2	0	0.2	0.4
0	0.2	0	0	0.2
0	0	0	0	0
0.2	0	0	0	-0.2
0.2	0	0.2	0	-0.4
1	0.2	0	0.2	-0.6
1	0.2	0	0	-0.8
1	0	0	0	-1
1	0	0.2	0	-1.2
1	0.2	1	0.2	-1.6
1	0.2	1	0	-1.8
1	0	1	0	-2

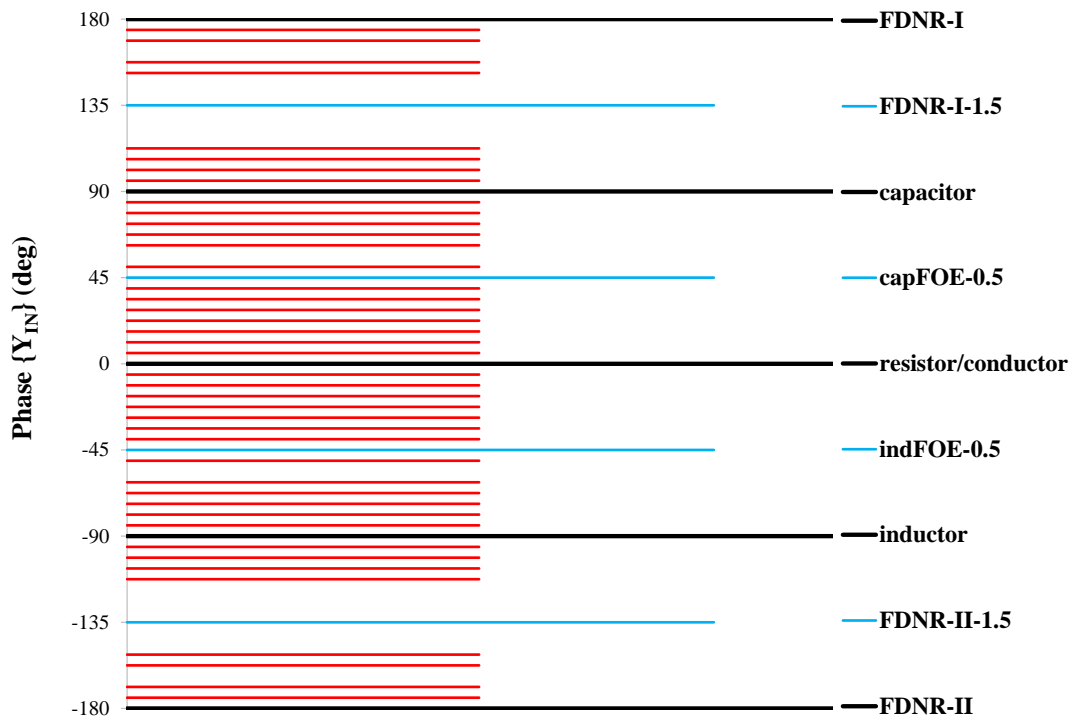


Fig. 4.11 Feasible phase angles of Y_{IN} (4.22) using up to two seed FOEs with $\alpha_{seed1} = 0.25$ and $\alpha_{seed2} = 0.0625$

Hence, it may be obvious that using a very limited set of “seed” FOEs, a broad series of new FOEs primarily with different fractional order α may be obtained. Furthermore, by adjusting the values of external capacitors (C), conductors (G), and most preferably also the transconductance g of the active/passive network it is possible to obtain a generally arbitrary value of the fractance being observed at the input of the GIC.

Table 4.2 Combinations of admittances Y_i , their α_i and the unique fractional order α of Y_{IN} for $\alpha_{seed1} = 0.25$ and $\alpha_{seed2} = 0.0625$

α_1	α_2	α_3	α_4	α
0	1	0	1	2
0	1	0.0625	1	1.9375
0.0625	1	0.0625	1	1.875
0	1	0.25	1	1.75
0.0625	1	0.25	1	1.6875
0.25	1	0.25	1	1.5
0	1	0	0.25	1.25
0	1	0.0625	0.25	1.1875
0.0625	1	0.0625	0.25	1.125
0	1	0	0.0625	1.0625
0	1	0	0	1
0	1	0.0625	0	0.9375
0.0625	1	0.0625	0	0.875
0	1	0.25	0.0625	0.8125
0	1	0.25	0	0.75
0.0625	1	0.25	0	0.6875
0.25	1	0.25	0.0625	0.5625
0	0.25	0	0.25	0.5
0	0.25	0.0625	0.25	0.4375
0.0625	0.25	0.0625	0.25	0.375
0	0.25	0	0.0625	0.3125
0	0.25	0	0	0.25
0	0.25	0.0625	0	0.1875
0	0.0625	0	0.0625	0.125
0	0.0625	0	0	0.0625
0	0	0	0	0

α_1	α_2	α_3	α_4	α
0.0625	0	0	0	-0.0625
0.0625	0	0.0625	0	-0.125
0.25	0	0	0.0625	-0.1875
0.25	0	0	0	-0.25
0.25	0	0.0625	0	-0.3125
0.25	0.0625	0.25	0.0625	-0.375
0.25	0	0.25	0.0625	-0.4375
0.25	0	0.25	0	-0.5
1	0.25	0.0625	0.25	-0.5625
1	0.0625	0	0.25	-0.6875
1	0	0	0.25	-0.75
1	0	0.0625	0.25	-0.8125
1	0.0625	0	0.0625	-0.875
1	0	0	0.0625	-0.9375
1	0	0	0	-1
1	0	0.0625	0	-1.0625
1	0.0625	0.25	0.0625	-1.125
1	0	0.25	0.0625	-1.1875
1	0	0.25	0	-1.25
1	0.25	1	0.25	-1.5
1	0.0625	1	0.25	-1.6875
1	0	1	0.25	-1.75
1	0.0625	1	0.0625	-1.875
1	0	1	0.0625	-1.9375
1	0	1	0	-2

4.3.1 Implementation and Properties of GIC

To prove the theoretical concept in designing series of floating FOEs, the novel configuration of GIC based on OTAs is shown in Fig. 4.12. Considering the relation (4.1) describing OTA and performing routine algebraic analysis, the input admittance is determined as

$$[Y_{IN}] = \begin{bmatrix} 1 & -1 \\ -1 & 1 \end{bmatrix} \frac{\prod_{i=1}^{p/2} Y_{(2i)}}{\prod_{i=1}^{p/2+1} Y_{(2i-1)}} \frac{\prod_{i=1}^{p/2+2} g_{m(2i-1)}}{\prod_{i=1}^{p/2+1} g_{m(2i)}}. \quad (4.24)$$

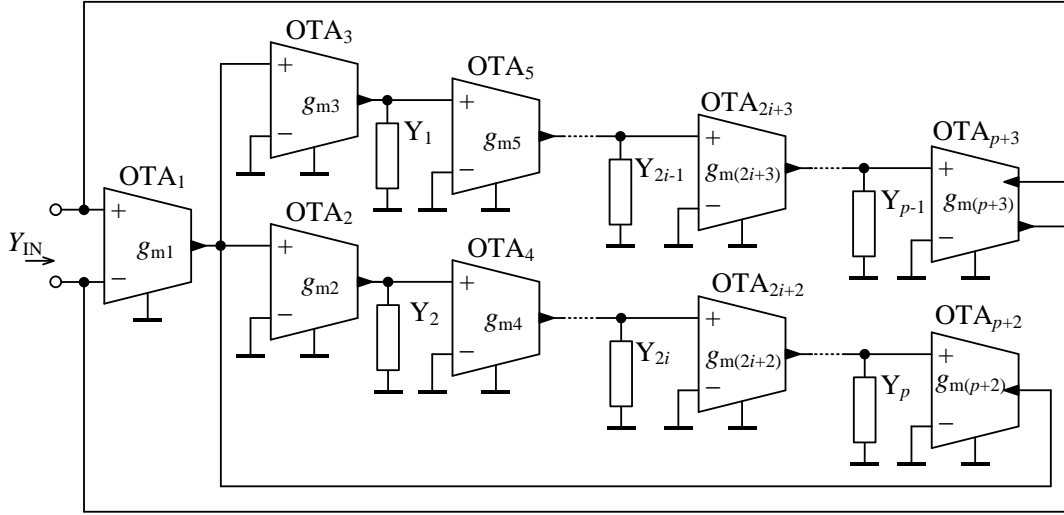


Fig. 4.12 Proposed OTA-based general immittance converter

Comparing (4.24) with (4.20), it may be observed that the proposed circuit from Fig. 4.12 fully follows the behavior of a GIC, whereas for the transconductance g it holds

$$g = \frac{\prod_{i=1}^{p/2+2} g_{m(2i-1)}}{\prod_{i=1}^{p/2+1} g_{m(2i)}}. \quad (4.25)$$

The following beneficial features of the proposed GIC are identified:

- Floating synthetic FOEs are designed;
- only grounded external admittances are employed;
- electronic tunability of $|Y_{IN}|$ is possible by proper adjustment of the transconductances g_m of the active elements;
- there is no restriction concerning matching between passive (external) or active elements.

In theory, using the proposed OTA-based GIC from Fig. 4.12, the feasible range of the fractional order α is $[-p, p]$, whereas p is generally an arbitrary even integer number. For a more practical design of a series of FOE, let $p = 4$. The GIC from Fig. 4.12 simplifies to a circuit as shown in Fig. 4.13, whose input admittance according to (4.24) is specified as

$$[Y_{IN}] = \begin{bmatrix} 1 & -1 \\ -1 & 1 \end{bmatrix} \frac{Y_2 Y_4}{Y_1 Y_3} \frac{g_{m1} g_{m3} g_{m5} g_{m7}}{g_{m2} g_{m4} g_{m6}}. \quad (4.26)$$

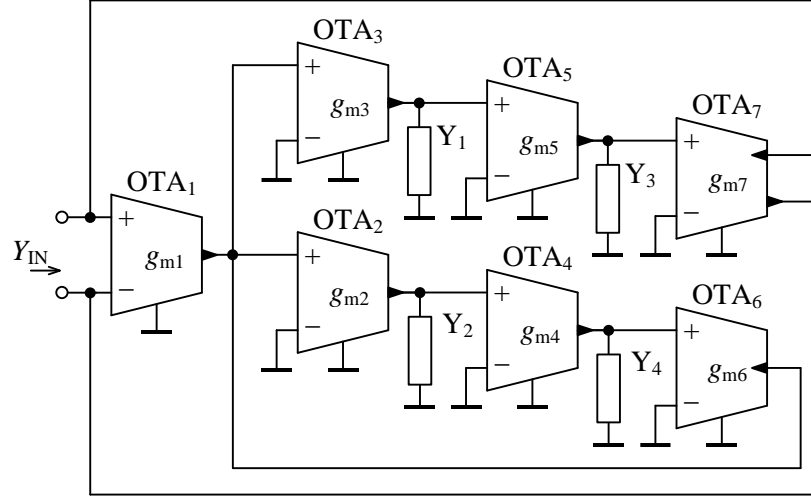


Fig. 4.13 Proposed OTA-based general immittance converter for $p = 4$

For the same reasons as already discussed above, assuming the external admittance elements Y_i ($i = 1, \dots, 4$) to be suitably replaced by conductors, capacitors, and capacitive-type “seed” FOEs, the immittance converter from Fig. 4.13 is capable of designing a series of FOEs with the fractional order α in the range $[-2, 2]$. Once the inductors and inductive FOEs are used to replace one or more external admittances, the range of fractional order α will be $[-4, 4]$.

For the purpose of analysis of the real behavior of the proposed GIC from Fig. 4.13, the OTA element designed in the $0.18 \mu\text{m}$ TSMC CMOS process as presented in [97] is used. The transconductance g_m of this element can be controlled by external voltage according to the relation

$$g_m = 2 \cdot 10^{-3} \cdot V_{SET} \quad (4.27)$$

in the range of V_{SET} from 0 to 0.5 V, i.e. g_m ranging from 0 to 1 mS. Details on this OTA element can be found in the article [97] and in [24], from which this section is mostly based.

4.3.2 Influence of OTA Parasitics and Optimization of GIC Performance

Similarly to the gyrator case in Subsection 4.1.1, the influence of real (parasitic) properties of OTAs on the overall performance of the proposed GIC will be analyzed. In theory, the internal impedance of OTA input and output terminals is infinity. Considering a real OTA, its properties are commonly modeled by resistances and capacitances

connected between each of the terminals and ground. Considering these OTA parasitic properties, the proposed GIC from Fig. 4.13 can be redrawn as seen in Fig. 4.14.

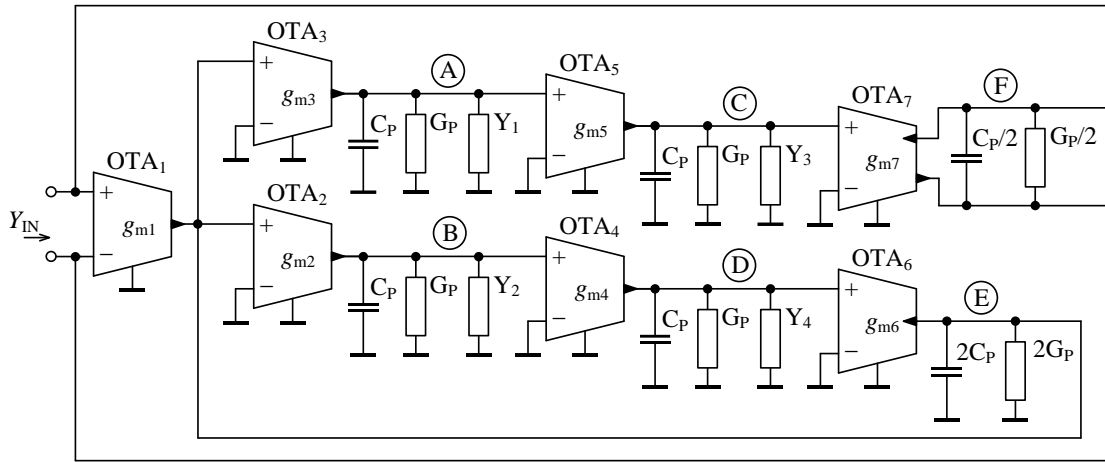


Fig. 4.14 Proposed GIC with OTA parasitic properties

Assuming that all OTAs in the circuit are the same, the parasitic conductors G_P symbolize a parallel combination of the input and output internal resistances of OTA. Similarly, the parasitic capacitors C_P represent a parallel combination of OTA input and output internal capacitances. Based on [97], their approximate values used in this analysis are $G_P \approx 1/(346 \text{ k}\Omega) = 2.89 \mu\text{S}$ and $C_P \approx 0.28 \text{ pF}$. For clarity, the nodes and input port, where the modeled parasitics are present are labeled by circled letters A to F in Fig. 4.14. Note that the parasitic elements in the node E express the properties of twice the number of OTAs, thus their conductance and capacitance are double compared to the other parasitic elements, i.e., $2G_P$ and $2C_P$. As the overall input port of the GIC labeled as F is differential, the terminal parasitic elements G_P and C_P are connected in series here (through ground) and thus these parasitics are considered to be $G_P/2$ and $C_P/2$. If the GIC is connected as single-ended, i.e., one of its input terminals is grounded, the values of the parasitic elements of the input node should be considered G_P and C_P .

To solely evaluate the influence of OTA parasitic properties, the FOEs, resistors, and capacitors used to replace the external admittance elements are assumed to be ideal.

i) Nodes, A, B, C, D

The external admittance elements connected to these nodes are expected to be replaced by conductors (i.e., resistors), classic capacitors, or capacitive FOEs. In case of replacing by conductors, the parallel parasitic conductance G_P is added, but it is usually very small compared to the external conductance and can be neglected. The capacitance C_P is also in parallel and considering external conductance of the order of millisiemens (mS), the parasitic effect of C_P becomes significant at a very high frequency (above approx. 500 MHz), and thus can also be neglected.

On the other hand, the replacement of external admittances by capacitors or capacitive FOEs is worth analyzing. At low frequencies these elements have a very low admittance magnitude and the parasitic conductance G_P may prevail. In case of FOE with fractional order α and fractance F this happens below the frequency:

$$\omega_{GP} \approx \left(\frac{G_P}{F} \right)^{\frac{1}{\alpha}}, \quad (4.28)$$

as illustrated by asymptotic admittance magnitude plot in Fig. 4.15.

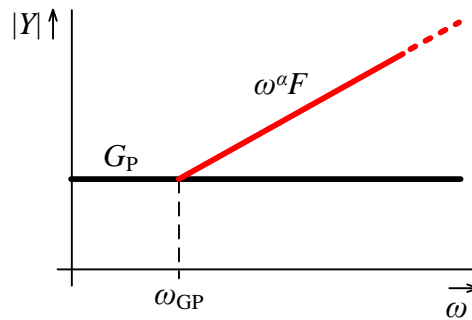


Fig. 4.15 Magnitude frequency characteristics of the working (red line) and parasitic (black line) admittances of the nodes A to D

Note that (4.28) is also valid for a classic capacitor when considering $\alpha = 1$ and a capacitance equal to F . It follows that for a higher value of F , correct operating range is extended to lower frequencies. Once for a specific F sufficiently low ω_{GP} is not provided, the parasitic conductance G_P can be reduced, e.g., by connecting in parallel a negative conductance as described in the Subsection 4.3.3 in detail. Using this approach, i.e., the negative conductance, the frequency ω_{GP} can theoretically be shifted to very low values. However, the demands on the accuracy of the negative conductance increase. Reducing G_P also decreases the lower bound of the obtainable admittance magnitudes of nodes A to D.

ii) Node E

In case of ideal OTAs, the order of the admittance of the node E (Y_E) equals to $\alpha_E = -(\alpha_2 + \alpha_4)$, and hence can range from 0 to -2 . Thus, the character of the admittance ranges from resistive through fractional inductive, inductive, fractional FDNR-II to FDNR-II. The resistive character will be not included in the analysis, as in this case the whole lower branch including OTA_2 , OTA_4 , and OTA_6 can be omitted and replaced by a resistor and a similar conclusion as described in the previous part *i)* is reached. Considering all other possible characters of Y_E , the OTA parasitic properties affect the circuit mainly at high frequencies, since the admittance magnitude defined as

$$|Y_E| = \frac{g_{m2}g_{m4}g_{m6}}{\omega^{(\alpha_2+\alpha_4)}F_2F_4}, \quad (4.29)$$

becomes comparable with or even lower than the admittance magnitude of the parasitics $2G_P$ or $\omega 2C_P$, which may prevail. The situation is illustrated by the admittance magnitude asymptotic plots in Fig. 4.16.

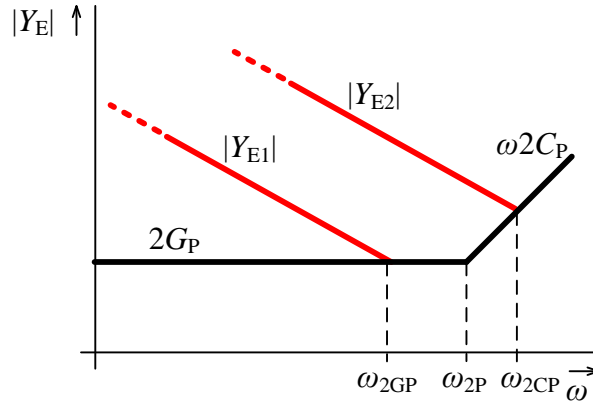


Fig. 4.16 Magnitude frequency characteristics of the working (red lines) and parasitic (black lines) admittances of the node E

The black lines are defined by the admittances of the parasitic elements and their breakpoint is at the frequency ω_{2P} :

$$\omega_{2P} = \frac{2G_P}{2C_P} = \frac{G_P}{C_P}. \quad (4.30)$$

This frequency is approximately 1.6 MHz for the above mentioned parasitics of the OTA. The red lines ($|Y_{E1}|$ and $|Y_{E2}|$) in Fig. 4.16 show two cases of possible admittance magnitudes of the node E that are not affected by the parasitics $2G_P$ and $2C_P$ yet. When the red lines approach the black “boundary” line represented by the admittance of the parasitics, these parasitics start to take effect. The cut-off frequency of the correct operation for the first case ($|Y_{E1}|$) is:

$$\omega_{2GP} \approx \left(\frac{g_{m2}g_{m4}g_{m6}}{2G_P F_2 F_4} \right)^{\frac{1}{\alpha_2+\alpha_4}}. \quad (4.31)$$

Considering the second case ($|Y_{E2}|$), the cut-off frequency is:

$$\omega_{2CP} \approx \left(\frac{g_{m2}g_{m4}g_{m6}}{2C_P F_2 F_4} \right)^{\frac{1}{1+\alpha_2+\alpha_4}}. \quad (4.32)$$

Both these frequencies can be increased by increasing $|Y_E|$, which can be done by increasing the product $g_{m2}g_{m4}g_{m6}$ as seen in (4.29). The decrease of the product F_2F_4 (F_2

and/or F_4) is also possible, however this may increase the lower cut-off frequency in the nodes B and/or D, see the part *i*) and (4.28). The orders α_2 and α_4 are fixed to obtain the required order of the GIC input admittance. The cut-off frequency ω_{2GP} can also be increased by decreasing $2G_P$ using the negative conductance compensation (see below in the Subsection 4.3.3 until $\omega_{2GP} = \omega_{2P}$). Decreasing further the parasitic conductance, the relation (4.32) starts to hold for the cut-off frequency. Note that if the compensation circuit with the negative conductance described below with the same OTA is used to reduce $2G_P$, in (4.30) and (4.32) it is necessary to assume $3C_P$ instead of $2C_P$ as the compensation circuit has its own parasitic capacitance equal to C_P .

Under certain conditions a sharp peak in the node E admittance magnitude characteristic can occur at the cut-off frequency. This happens when the sum of the phasors of ideal Y_E , $j\omega 2C_P$, and $2G_P$ approaches zero as illustrated in Fig. 4.17. The behavior of the GIC can be unstable in this case and it is necessary to ensure a suitable damping of the oscillations. Damping can be provided by modifying the value of $2G_P$ by connecting an appropriate positive or negative conductance in parallel. However, in most cases the circuit is damped by its own parasitic properties and no modification is necessary. Excessive damping is not recommended as it can lead to an exceedingly soft transition of input admittance phase in a very broad band around the cut-off frequency.

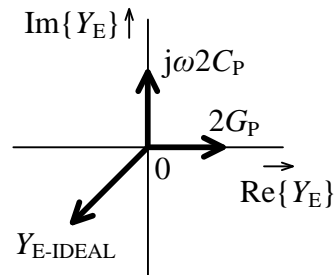


Fig. 4.17 Phasor diagram resulting in zero admittance of node E

iii) Port F

The port F is the overall input node of the GIC and thus $Y_F = Y_{IN} = s^\alpha F_{IN}$. This admittance is specified as the design criterion and thus cannot be modified during optimization. Due to the limited optimization possibilities (in fact involving only changes in parasitics) it is suitable to evaluate and optimize the GIC performance in the port F first. The optimization of other nodes beyond the performance of the port F brings no improvement.

The fractional order α of Y_F is in case of ideal OTAs given by (4.23) and ranges from -2 to 2 . If α is positive, the admittance at port F is capacitive and at high frequencies it reaches high values in magnitude compared to the admittance of parasitics $G_P/2$ and $\omega C_P/2$ present at the port. Thus, the parasitics do not take effect in the port F at high frequencies and the upper frequency of the GIC operation is determined primarily by the properties of node E as described in the part *ii*) above. On the other hand, at low

frequencies Y_F can reach a low magnitude comparable with the parasitic conductance $G_P/2$ present at port F. This is similar to the situation described in the part *i*) for nodes A, B, C, and D. Since the admittance Y_F cannot be changed as mentioned above, the only way to broaden the operation band to lower frequencies is to reduce the parasitic conductance at port F, e.g., using the compensation technique as proposed below in the Subsection 4.3.3. Additionally, the cut-off frequencies of the nodes A, B, C, and D should be determined and if necessary adjusted in accordance with the cut-off frequency of port F.

If α is negative, the admittance at port F is inductive and at high frequencies it can reach a low magnitude that is comparable with the admittance of parasitics $G_P/2$ and/or $\omega C_P/2$. The analysis is then similar to node E, see the part *ii*), with the difference that in this case the magnitude of Y_F cannot be modified. Hence, the optimization can be done only by reducing $G_P/2$ such that it is lower than both $|Y_{IN}|$ and $\omega C_P/2$ at frequency, where these admittances are equal, that is:

$$\omega_{CP/2} = \left(\frac{F_{IN}}{C_P/2} \right)^{\frac{1}{1-\alpha}}, \quad (4.33)$$

and it is the maximum operation frequency of the port F and cannot be increased. Note that when the differential compensation circuit described in the Subsection 4.3.3 with the same OTA is used to reduce parasitic conductance at port F, in (4.33) it is necessary to assume C_P instead of $C_P/2$, as again the compensation circuit (its differential variant) has its own parasitic capacitance $C_P/2$. The subsequent step is verification or prospective optimization of the cut-off frequency of the node E, whereas its value specified by (4.31) or (4.32) is to be at least as high as $\omega_{CP/2}$ given by (4.33). Also note that when the GIC is connected as single-ended, the parasitics in port F should be considered with values G_P and C_P instead of $G_P/2$ and $C_P/2$. The single-ended variant of the compensation circuit with negative conductance can be utilized as presented below. The effectiveness of the described compensation possibilities in individual nodes is demonstrated and discussed by two examples in the Subsection 4.3.5.

4.3.3 OTA-Based Circuit with Negative Conductance

When the parasitic conductance present in a node of the proposed GIC is to be decreased within performance optimization as described in the previous Subsection 4.3.2, simple compensation circuits as shown in Fig. 4.18 can be employed. The single-ended circuit from Fig. 4.18(a) is suitable for compensation of parasitic conductance at the nodes A to E, since compensation conductance in the COMP terminal relative to ground is

$$G_{COMP} = -g_{mC} + G_P, \quad (4.34)$$

whereas the differential circuit in Fig. 4.18(b) can be connected to the port F and its input conductance is

$$G_{\text{COMP}} = -g_{\text{mC}} + \frac{G_{\text{P}}}{2}. \quad (4.35)$$

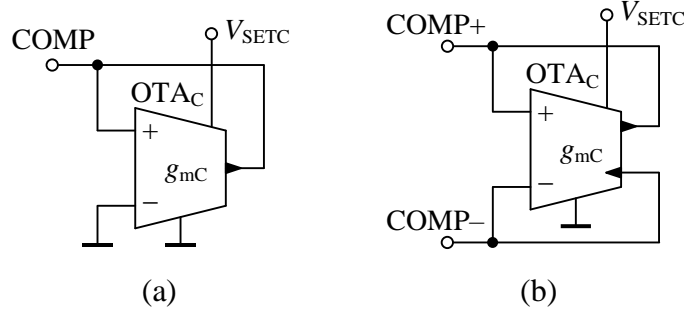


Fig. 4.18 Circuit with negative conductance (a) between terminal COMP and ground; (b) between terminals COMP+ and COMP-

We consider that the utilized OTA_{C} element has the same parasitic terminal properties as the OTAs used in the proposed GIC. The conductance G_{COMP} can be set to an appropriate negative value by setting of g_{mC} using the control voltage V_{SETC} . It should be again noted that when connecting the circuits from Fig. 4.18 to a node or port, the total parasitic capacitance in the node or port increases by the parasitic capacitance of the compensation circuit which is C_{P} or $C_{\text{P}}/2$ in the case of Fig. 4.18(a), (b), respectively. Thus, it is necessary to take this value into account in the relations containing the parasitic capacitance of the node or port being optimized.

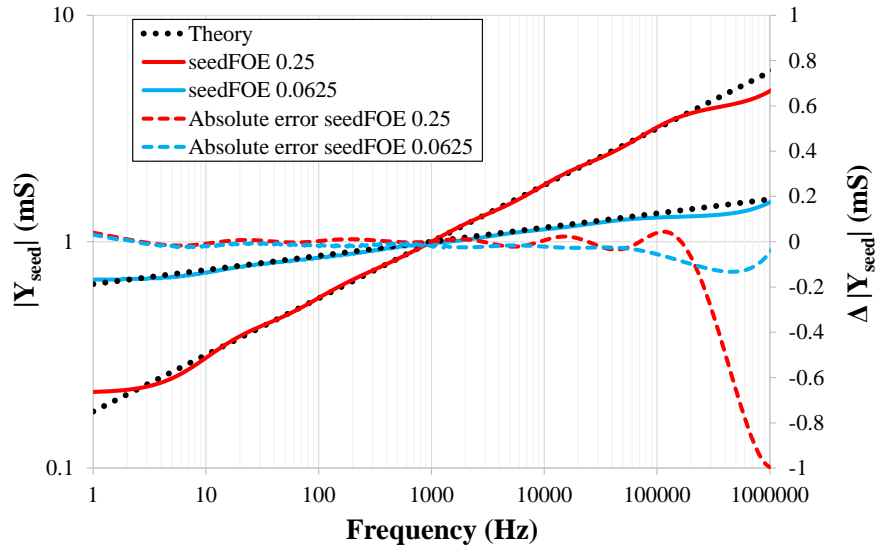
4.3.4 Simulation Results

To prove the functionality of the proposed GIC and mainly to show its advantageous feature in designing a wide set of FOEs using a very limited count of “seed” FOEs, the performance of the GIC was further verified by post-layout simulations in Cadence Virtuoso 6.1.6. First, two “seed” FOEs are designed and further utilized in the proposed GIC, whereas following the recommendations from the Subsection 4.3.2, the optimization steps are also verified to improve the overall performance of the GIC.

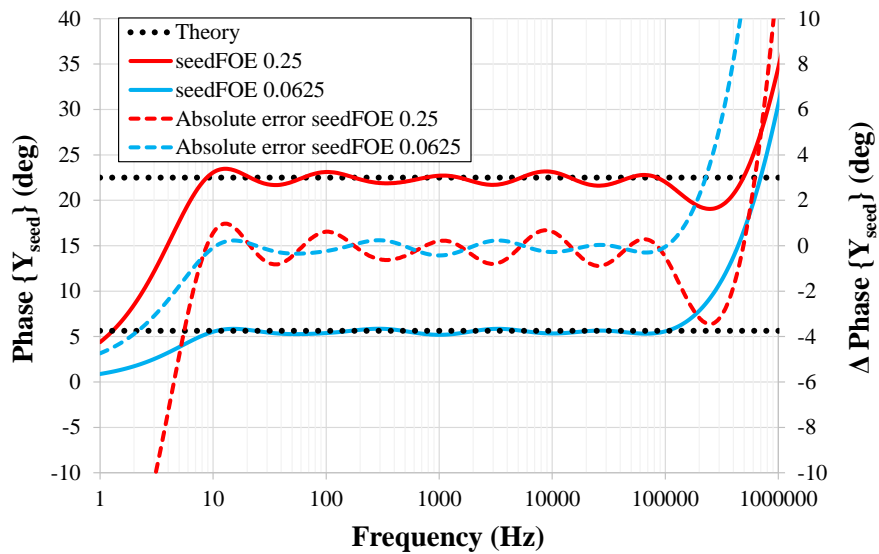
To obtain the set of new FOEs and their fractional order α as listed in Tab. 4.2, the “seed” FOEs with $\alpha_{\text{seed1}} = 0.25$ and $\alpha_{\text{seed2}} = 0.0625$ are required. Due to the commercial unavailability of such FOEs, these “seed” FOEs were approximated by 7th-order Valsa topology with the resistances and capacitances determined using the approach described in [93]. The fractances (pseudo-capacitances) of the two “seed” FOEs are $F_{\text{seed1}} = 112.3 \mu\text{F} \cdot \text{s}^{-0.75}$ and $F_{\text{seed2}} = 578.9 \mu\text{F} \cdot \text{s}^{-0.9375}$, and their admittance at central frequency of approximation 1 kHz is 1 mS. The schematic and resistance and capacitance values of these emulators can be found in the article [24].

In Fig. 4.19 the magnitude and phase admittance frequency characteristics of the approximated “seed” FOEs are shown (solid lines) and compared with ideal “seed” FOEs

(dotted lines). The absolute errors in magnitude and phase of the approximated “seed” FOEs are also depicted (dashed lines), whereas the correct operation may be observed in 4 frequency decades, i.e., from 10 Hz to 100 kHz.



(a)



(b)

Fig. 4.19 Simulation results of admittance of designed “seed” FOEs with central frequency 1 kHz: (a) Magnitude responses; (b) phase responses

To implement the proposed GIC, the OTA cell designed in the 0.18 μm TSMC CMOS process as described in detail in [24] and [97] was used. The overall circuit layout of the proposed GIC is shown in Fig. 4.20. Here, the cells OTA_i ($i = 1, \dots, 7$) correspond to prime active elements of the GIC circuit as shown in Fig. 4.13. The cells OTAC_j ($j = A, B, \dots, F$) represent the single-ended or differential compensation circuit from Fig. 4.18 to

reduce the parasitic conductance G_P present in the nodes A to E, or port F as labeled in Fig. 4.14. Additionally, the block I_{BIAS} is a set of current sources to bias the OTA cells. The labels Y_1, Y_2, Y_3, Y_4 , and Y_{IN+}, Y_{IN-} represent the pins, to which the external discrete elements, i.e., resistors, capacitors, and/or “seed” FOEs are to be connected, or the input terminal of the GIC, respectively.

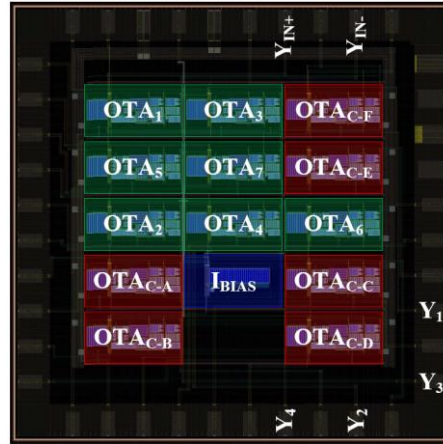
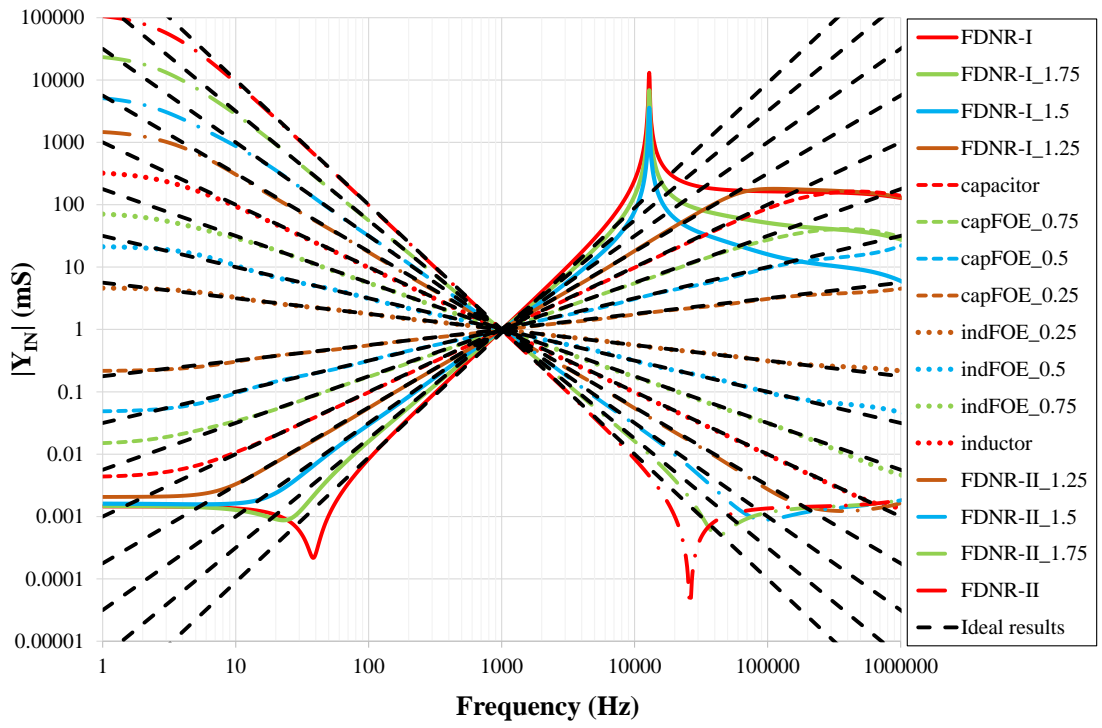


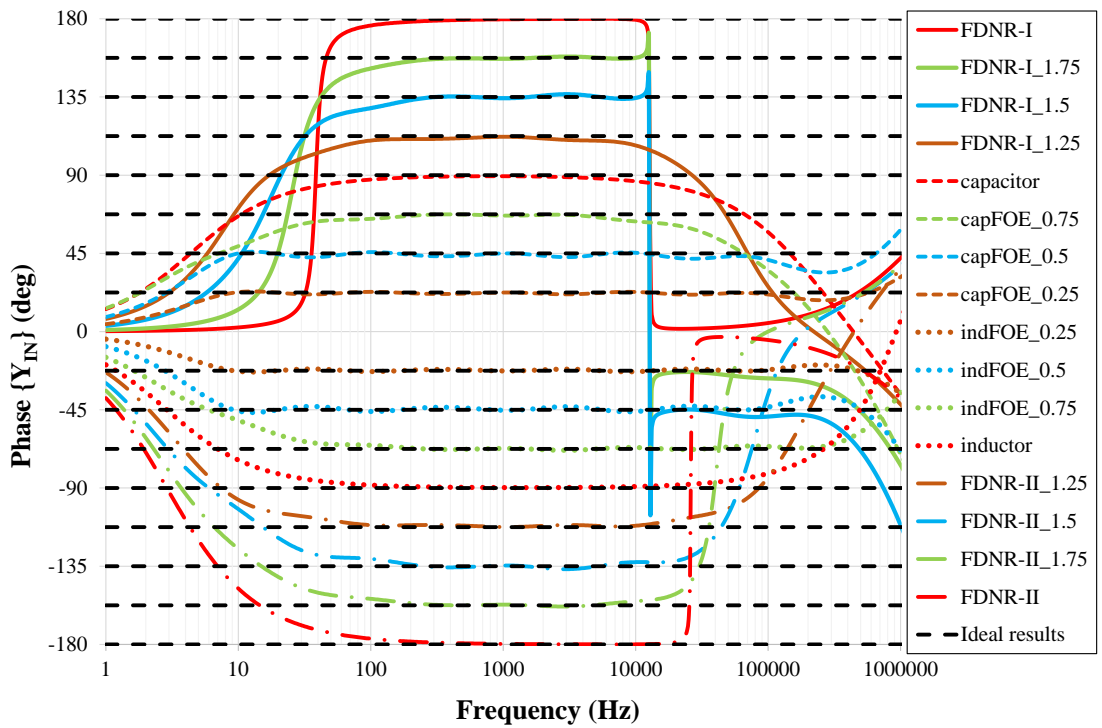
Fig. 4.20 Circuit layout of the proposed GIC

Within the simulations, next to the “seed” FOEs as described in the beginning of this subsection, the external general admittance elements Y_1, Y_2, Y_3 , and Y_4 of the GIC are always replaced by 1 mS conductances (i.e. 1 k Ω resistors) or 159.2 nF capacitors (as at the central frequency 1 kHz their admittance is 1 mS). The transconductances g_m of all prime OTAs are 1 mS (i.e. $V_{SET} = 0.5$ V). The resulting magnitude and phase characteristics of the input admittance of the immittance converter from Fig. 4.13 are presented in Fig. 4.21. The black dashed lines represent the results with ideal elements (OTAs, resistors, capacitors, and “seed” FOEs) employed. To maintain the clarity of the simulation results being displayed in Fig. 4.21, only the α values from the range $[-2, 2]$ with the step 0.25 were selected. Based on the values of external admittances and setting of OTAs, the input admittance magnitude of the GIC is always $|Y_{IN}| = 1$ mS at 1 kHz.

In Fig. 4.21 it is apparent that the input admittance magnitude and phase characteristics are affected by the parasitic properties of OTAs. Most distorted are the characteristics for $|\alpha| > 1$, both at low and high frequencies, whereas peaking is evident in several cases in the magnitude characteristics (Fig. 4.21(a)). This peaking is caused by the resonance of the node E or port F admittance (which has a character of fractional- or integer-order FDNR-I or FDNR-II) with OTA parasitic conductance. Fortunately, damping of the oscillations is always ensured by the OTA parasitic capacitance and thus the circuit is stable. However, the overall bandwidth of correct operation for the highest values of $|\alpha|$ reduces down to two decades only, which is two decades lower than the bandwidth of the “seed” FOE emulators. To broaden the bandwidth of the GIC, optimization is required by the steps as described above in the Subsections 4.3.2 and 4.3.3, which are validated in the next Subsection 4.3.5.



(a)



(b)

Fig. 4.21 Simulation results of input admittance of the proposed GIC with OTA parasitics: (a) Magnitude responses; (b) phase responses

4.3.5 Optimization Examples

The influence of the OTA parasitics on the significant reduction of the operational frequency band of the newly obtained FOEs can be observed in Fig. 4.21, mainly for $|\alpha| > 1$. To reach an operational bandwidth of FOEs at the input of GIC to be at least the same as it is of the “seed” FOEs (i.e., 10 Hz – 100 kHz), optimization is necessary and is demonstrated on two following examples.

i) Optimization Example for $\alpha = 1.75$

In this case, the fractional FDNR-I is obtained at the input of the GIC, i.e., port F, whose fractance is $F_{IN} = 22.55 \text{ nF}\cdot\text{s}^{0.75}$. Decreasing frequency, the input admittance magnitude also decreases until the parasitic conductance $G_P/2$ starts to prevail. This happens at a lower cut-off frequency at approximately 23.8 Hz (Fig. 4.21(a)) generally determined by (4.28), where G_P was substituted by $G_P/2$ (note that (4.28) is originally valid for nodes A, B, C, D where parasitic conductance G_P is present).

Within optimization, using the circuit from Fig. 4.18(b) to compensate the parasitic conductance at port F, the lower cut-off frequency is decreased down to 1 Hz to maintain a sufficient margin to frequency 10 Hz due to soft admittance phase transition (Fig. 4.21(b)). To reach this new lower cut-off frequency, the input conductance G_{COMP} was set to $-1.439 \mu\text{S}$, whereas according to (4.35) compensation transconductance g_{mC} equals to $2.885 \mu\text{S}$.

The upper cut-off frequency is determined by the parasitics of the node E as described in the respective part of Subsection 4.3.2. To increase this upper cut-off frequency, it is necessary either to increase the product $g_{m2}g_{m4}g_{m6}$ or to decrease F_2F_4 (in this case capacitances C_2 and C_4 as $\alpha_2 = \alpha_4 = 1$). Since the transconductances g_m of all OTAs are already set to 1 mS (which is maximum value of the utilized OTA structure [24]), the product $g_{m2}g_{m4}g_{m6}$ cannot be further increased. Hence, having selected the upper cut-off frequency to be 100 kHz, using (4.31) new capacitances C_2 and C_4 (considering them equal) were determined to be 20.9 nF. Note that here the margin from the required 100 kHz was not considered, as the damping in the node E is low and the admittance phase shows the transition in a narrow band. Moreover, the excessive increase of the upper cut-off frequency in node E would lead to lower capacitances C_2 and C_4 and undesirable deterioration of the cut-off frequency in nodes B and D.

Within the optimization of the upper cut-off frequency, the ratio $g_{m2}g_{m4}g_{m6}/(F_2F_4)$ was increased. Hence, to keep the original value of the input fractance F_{IN} unaffected, according to general formula (4.26), the ratio $G_1F_{seed1}/(g_{m1}g_{m3}g_{m5}g_{m7})$ must decrease. As again the transconductances g_m of all OTAs are already set to their maximum values (i.e., 1 mS) and the “seed” FOE is not expected to be modified, the only possibility is to decrease G_1 to $17.3 \mu\text{S}$.

ii) Optimization Example for $\alpha = -1.75$

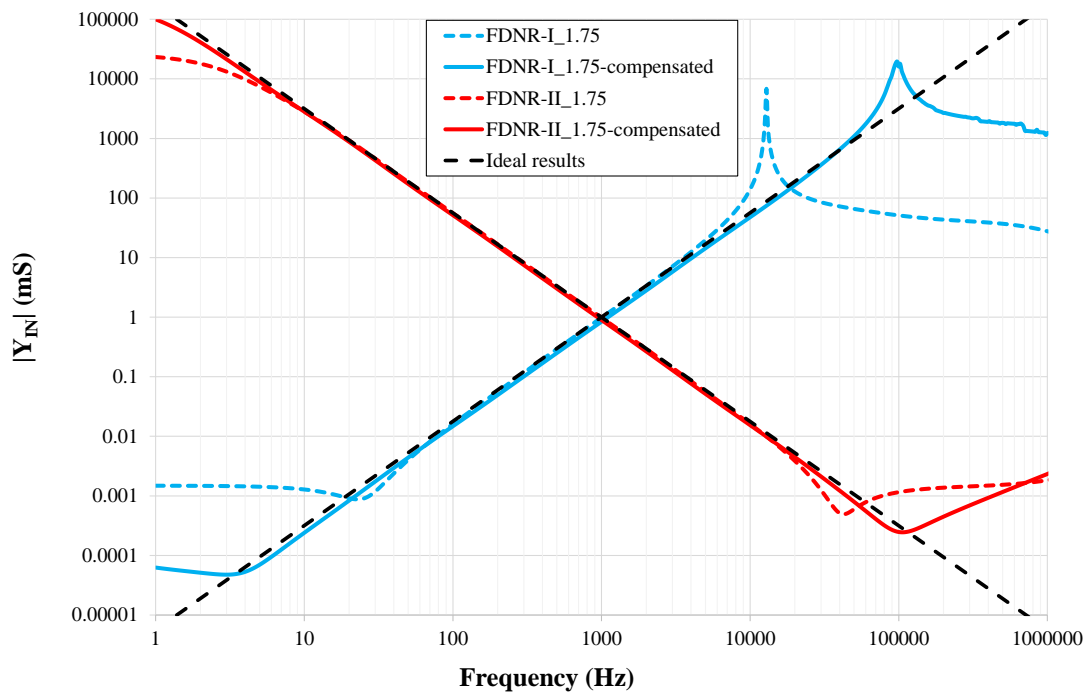
For this case, the fractional FDNR-II with fractance $4\,434 \text{ F}\cdot\text{s}^{-2.75}$ is obtained at the input

of the GIC. The admittance magnitude decreases with increasing frequency, where the parasitics at port F define the upper cut-off frequency of approximately 42 kHz (Fig. 4.21(a)) generally determined by (4.28), where again G_P was substituted by $G_P/2$. The only solution to increase the upper cut-off frequency is to reduce the parasitic conductance of the port F by using the compensation circuit from 4.18(b). In this case it is possible to decrease the port F parasitic conductance almost to zero, thus the transconductance of the compensation circuit is set slightly lower than G_P , i.e., $g_{mC} = 2.888 \mu\text{S}$.

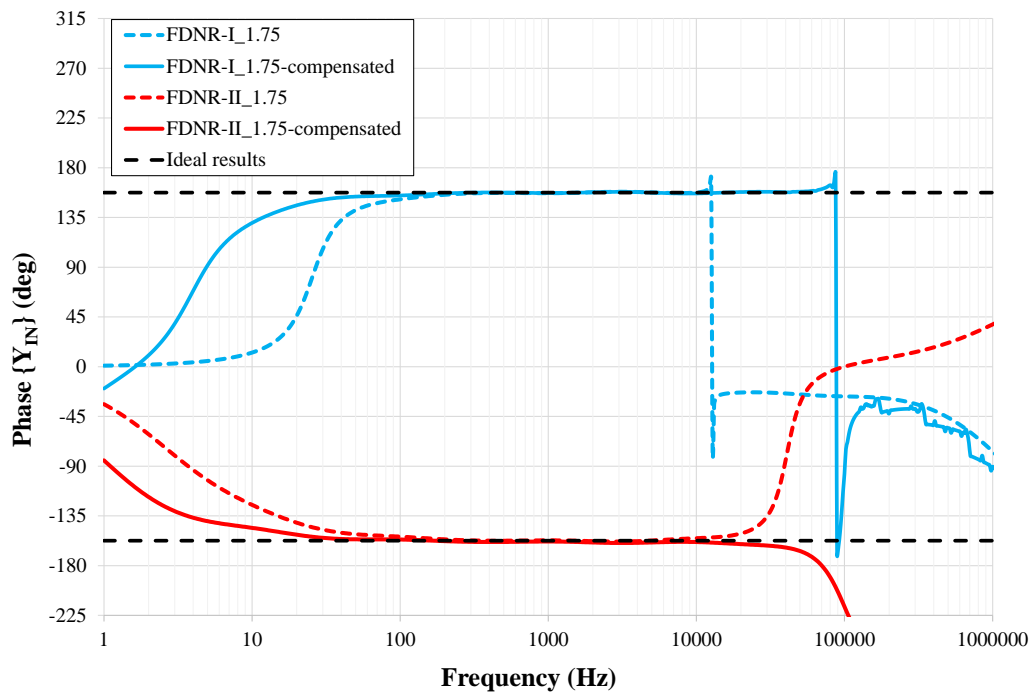
To reduce the lower cut-off frequency, it is necessary to increase capacitances C_1 and C_3 in the nodes A and C according to (4.28). The optimized lower cut-off frequency is set to 1 Hz to have again sufficient margin to 10 Hz due to soft phase transition. Hence, the new value of capacitances C_1 and C_3 is 460 nF. Within the optimization of the lower cut-off frequency the product C_1C_3 was increased. Thus, the ratio $g_{m2}g_{m4}g_{m6}/(G_2F_{\text{seed1}}g_{m1}g_{m3}g_{m5}g_{m7})$ must decrease according to general formula (4.26) to keep the original value of the input fractance F_{IN} unchanged. For this purpose, the transconductances g_{m2} , g_{m4} , and g_{m6} were set to 0.493 mS, whereas g_{m1} , g_{m3} , g_{m5} , g_{m7} , G_2 , and mainly F_{seed1} are kept the same. As the transconductances g_{m2} , g_{m4} , and g_{m6} were changed, it is necessary to check the upper cut-off frequency of the node E if it is large enough. According to (4.32) the value of $f_{2\text{CP}}$ is 4.2 MHz, which is much more than the required upper cut-off frequency of 100 kHz. Hence no further optimization is needed.

For the both optimized examples described, the resulting admittance magnitude and phase frequency characteristics are shown in Fig. 4.22 along with the characteristics of the non-optimized GIC taken from Fig. 4.21. It is evident that the optimized circuit provides a higher frequency bandwidth of the admittance characteristics covering the required 4 decades. The fractional FDNR-I (blue lines) reaches an upper cut-off frequency almost equal 100 kHz as considered during the optimization. The lower cut-off frequency reached approximately 5 Hz, which is higher than the projected value of 1 Hz, however, here the GIC function is affected by parasitics of multiple nodes and also the “seed” FOE emulator shows a higher error (see Fig. 4.19). The fractional FDNR-II (red lines) has also been optimized successfully. Its upper cut-off frequency is around 100 kHz and lower cut-off frequency is below 1 Hz. Additionally, as seen from Fig. 4.22(a), the dynamic range of the admittance magnitude has also increased thanks to the optimization.

In conclusion, it should be noted that the described GIC with OTA cells designed in 0.18 μm TSMC CMOS process as described in detail in [24] and [97] was already available at the time of writing this thesis as a custom integrated circuit “FGIC44 – Fully Controllable Immittance Converter” [104]. It was designed and fabricated within the Czech Science Foundation project GA19-24585S in the framework mini@sic of Europractice IC Service (IMEC, Belgium). The experimentally determined performance of FGIC44 and the OTAs forming its core are presented in [105]. The electronic controllability of the structure, its wide frequency range and also the possibility of compensation of parasitic internal conductances of the terminals are demonstrated in [24].



(a)



(b)

Fig. 4.22 Simulation results of input admittance of proposed GIC with compensated OTA parasitics: (a) Magnitude responses; (b) phase responses

5. IMPEDANCE MODELS EMPLOYING FOE

A frequent use of FOE is modeling the impedance characteristics of biological tissues and biochemical materials using substitute circuits also called phantoms. This is especially important in the case of biological materials that degrade rapidly over time or are difficult to obtain. Preservation of sample properties using circuit models is also important for the development of new measurement techniques of these samples and comparison of various results reached by different researchers dealing with the same topic and using different measurement methods.

The author of this thesis also contributed to the development of knowledge in this field. He dealt with modeling of electrical properties of the cell membrane using FOC in the article [106] or realization of synthetic FOI for an electrical model of the human respiratory system in the work [96]. The following section is based on the first of these articles.

5.1 FOE in Cardiac Cell Membrane Model

The Cole impedance model shown in Fig. 5.1 is commonly used for characterizing bioimpedance properties [43]. It consists of a resistor R_∞ that represents the model resistance at very high frequency, a resistor R_1 , and capacitor with capacitance C or FOC with fractance F and order α which is also known as the dispersion coefficient in this branch. The relations above the capacitor in Fig. 5.1 express its impedance. The resistance of the model at very low frequency is expressed as $R_\infty + R_1$. Many research studies confirmed that employing FOC instead of classic capacitor in the Cole model brings improvement in the modeling accuracy [10] and the author of this thesis attempted to validate this statement also for cardiac cells.

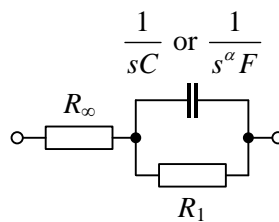


Fig. 5.1 Single-dispersion Cole impedance model

For accurate characterization of a particular object by the Cole model with FOC, it is necessary to determine the four parameters R_∞ , R_1 , α , and F from measured data. Early methods extracted the parameters from real-imaginary impedance plot, later numerical methods have been proposed that select the model parameters such that the analytical response of the model fits the experimental data with minimal least squares error [10]. The utilized response may be in frequency domain (impedance or its selected component) or time domain (voltage or current response to a defined waveform). The method

described in this section uses time-domain current measurements with voltage excitation, whereas related techniques for extracting the Cole model parameters using current input signal and least squares fitting can be found in [107] and [108].

According to the best of author's knowledge, the Cole model with FOC has not yet been used in modeling the electrical properties of the cardiac cell membrane. Usually, an equivalent circuit corresponding to Fig. 5.1 is used for this modeling, but instead of FOC, a standard capacitor is used [109], [110]. Hence, the objective and scientific novelty of this section is to determine whether the electrical impedance properties of the cell membrane show a fractional character, and thus whether it is possible to model them more accurately with the Cole circuit, where the α value is not equal to one, but is lower.

It should be noted that so-called fractal behavior of a cell membrane is discussed in [111] where it is found that fractal dimension FD is a measure of the membrane morphological complexity. The fractal single-shell model describing dielectrics of mammalian cells proposed in [111] is in fact based on FOC with $\alpha = 1/(FD - 1)$.

5.1.1 Cell Membrane Measurement Technique

Fig. 5.2 shows experimental setup comprising an isolated cardiac cell (orange color) connected to a glass patch microelectrode [112], [113]. For the measurements, the cardiomyocytes were obtained by enzymatic isolation from right ventricles of adult male anesthetized Wistar rats. The isolated cardiomyocytes were placed in a measuring chamber containing Tyrode solution. Glass patch pipettes were pulled from borosilicate glass capillary tubes. Recordings of current responses have been performed using the whole-cell patch-clamp technique in the voltage-clamp mode using the Axopatch 200B equipment (Axon Instruments Inc., USA) and pCLAMP 10.2 software.

Apparently, the schematic symbols indicated in Fig. 5.2 form an electrical equivalent circuit corresponding to the Cole model in Fig. 5.1.

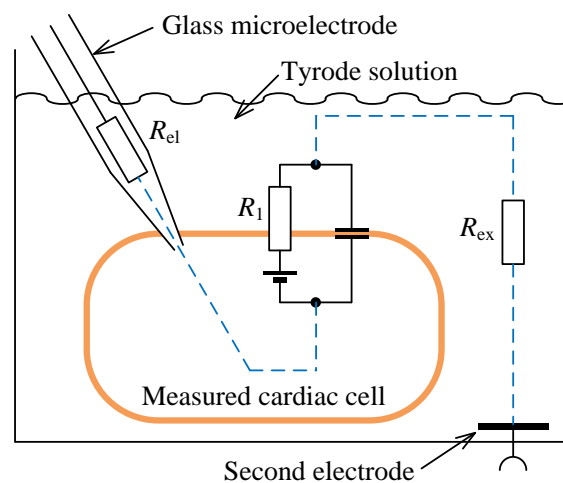


Fig. 5.2 Experimental setup for measuring current step response of cell membrane

The access resistance corresponding to the sum of glass electrode resistance (R_{el}) and resistance of extracellular solution between the second electrode and the measured cell (R_{ex}) are modelled by R_{∞} in Fig. 5.1. The parallel RC circuit across the membrane can be represented in the model by the elements R_1 and FOC.

Measurement techniques used in cellular electrophysiology are based on the measurement of membrane currents and action potential of cells. The patch-clamp technique, a specialized version of the voltage-clamp, is used to measure membrane currents. This measurement method is based on evaluating current responses to changes in membrane voltage, most commonly rectangular pulses or harmonic waveforms. Small voltage pulses around the resting membrane voltage (represented by the voltage source in Fig. 5.2) are usually used to study the electrical properties of the membrane. In the subthreshold range of the imposed membrane voltage, the parameters of the model elements are regarded as constants [109]. Determination of the membrane parameters from the recorded responses is based on the analytical formulas describing the electrical equivalent circuit of the cell connected to the measuring device in time or frequency domain. The measurement in time domain using continuous rectangular wave stimulation allows for high-resolution determination of membrane model parameters [110], [114] and will also be used here to find the parameters of the Cole model.

The typical waveforms of the imposed rectangular voltage and the membrane current responses are schematically sketched in Fig. 5.3. Only positive pulses are depicted, as only the time interval from t_0 to t_f will be further utilized for the extraction of model parameters.

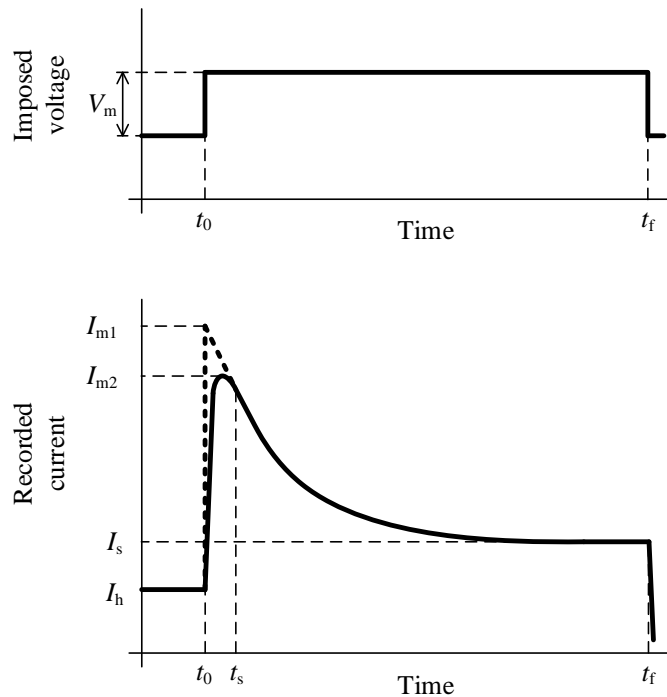


Fig. 5.3 Imposed voltage pulse and response of the membrane current

To simplify the following steps, it is convenient to shift the recorded current down by the value of the holding current I_h . Thus, the average holding current was detected and subtracted from the recorded current. This makes it possible to consider the current I_h equal to zero and the voltage oscillating between 0 V and V_m in the subsequent steps. Similarly, the time t_0 will be considered zero to shift the rising edge of the input voltage to the base position. Note the initial transient event in the current response between t_0 and t_s associated with the limited slew rate of the setup where the recorded current differs from the expected theoretical response indicated by the dashed line. The maximum current value I_{m1} cannot be determined exactly from the measured data and only approximate value I_{m2} is available.

5.1.2 Analytical Formulas and Least Squares Fitting

The input impedance of the Cole model in Fig. 5.1 is given in Laplace transform by

$$Z(s) = R_\infty + \frac{R_1}{s^\alpha FR_1 + 1}. \quad (5.1)$$

The current through the model can be computed by the Ohm's law as $I(s) = V(s)/Z(s)$, whereas the voltage $V(s)$ is in this case Laplace transform of voltage step with amplitude V_m , i.e. $V(s) = V_m/s$. After substitution, the current is

$$I(s) = \frac{V(s)}{Z(s)} = \frac{V_m}{s \left(R_\infty + \frac{R_1}{s^\alpha FR_1 + 1} \right)}. \quad (5.2)$$

After rearranging, the relation (5.2) becomes a format

$$I(s) = V_m \left(\frac{s^{\alpha-1} \frac{1}{R_\infty}}{s^\alpha + \frac{R_1 + R_\infty}{FR_1 R_\infty}} + \frac{s^{-1} \frac{1}{FR_1 R_\infty}}{s^\alpha + \frac{R_1 + R_\infty}{FR_1 R_\infty}} \right), \quad (5.3)$$

which is suitable for inverse Laplace transform leading to analytic description of transient response. For this purpose, the following formula is utilized [115]

$$\mathcal{L}^{-1} \left\{ \frac{s^{\alpha-\lambda}}{s^\alpha + \gamma} \right\} = t^{\lambda-1} E_{\alpha,\lambda}(-\gamma t^\alpha), \quad (5.4)$$

where $E_{\alpha,\lambda}(-\gamma t^\alpha)$ is the Mittag-Leffler function with two parameters defined as

$$E_{\alpha,\lambda}(z) = \sum_{i=0}^{\infty} \frac{z^i}{\Gamma(\alpha i + \lambda)}, \quad (5.5)$$

where $\Gamma(\cdot)$ is the Gamma function. The resulting time domain expression of the Cole model current response due to the voltage step is

$$i(t) = V_m \left[\frac{1}{R_\infty} E_{\alpha,1} \left(-\frac{R_1 + R_\infty}{FR_1 R_\infty} t^\alpha \right) + \frac{1}{FR_1 R_\infty} t^\alpha E_{\alpha,\alpha+1} \left(-\frac{R_1 + R_\infty}{FR_1 R_\infty} t^\alpha \right) \right]. \quad (5.6)$$

In case of replacing the FOC in the model by classic capacitor with capacitance C , the relation (5.6) simplifies to the following form containing exponential function

$$i_{\text{int}}(t) = \frac{V_m}{R_1 + R_\infty} \left[\frac{R_1}{R_\infty} e^{-\frac{R_1 + R_\infty}{CR_1 R_\infty} t} + 1 \right]. \quad (5.7)$$

The relations (5.6) and (5.7) will be used to obtain the parameters of the model by minimizing the error against the recorded current response. According to the resulting error, it will be evaluated whether FOC in the model brings an improvement in the modeling of the electrical properties of the cell compared to classic capacitor.

Non-linear least squares fitting of the recorded current decay is used to find element values of the Cole model containing either FOE or classic capacitor. This numerical method aims to minimize the following Least Squares Error (*LSE*)

$$LSE = \sum_{i=1}^M [i(X, t_i) - \text{RecCur}(t_i)]^2, \quad (5.8)$$

where X is the sought vector of Cole model parameters (R_∞, R_1, α, F), $i(X, t_i)$ is the time-domain response calculated by (5.6) using X , and $\text{RecCur}(t_i)$ is the recorded current response. A total of $M = 60$ time instants t_i are chosen from the interval between t_s and t_f . These instants are logarithmically distributed over time so that the fitting considers more datapoints at the beginning of the response where the current changes faster.

The fitting was carried out by the MATLAB function *fminsearch* with the argument given by (5.8). This function finds the minimum of a user supplied unconstrained multivariable function using a nonlinear derivative-free method. The Mittag-Leffler function was evaluated with accuracy 10^{-10} by the routine [116]. The *fminsearch* function requires initial guess of the sought parameters X . Generally, the resistance R_∞ would be determined as $R_\infty = V_m/I_{m1}$. However, as already mentioned at the end of Subsection 5.1.1, the maximum current value I_{m1} cannot be detected from the measured response. Anyway, the achieved maximum I_{m2} is sufficient for the initial guess of the resistances in the Cole model. Thus, the relations $R_{\infty G} = V_m/I_{m2}$ and $R_{1G} = V_m/I_s - V_m/I_{m2}$ can be used to get the initial guesses of the model resistances.

Due to the fact that the cell membrane shows a current response close to standard exponential function, a relatively high value of α approaching one can be expected. Therefore, it is appropriate to choose $\alpha_G = 0.9$ as the initial guess. As an initial estimate of fractance F , it is possible to use a capacitance value C_G determined by a method for extraction of classic membrane capacitance from exponential response, such as [117].

To minimize probability of finding a local minimum, the function *fminsearch* is executed multiple (100) times, each time with randomly selected initial guesses from the intervals:

- R_∞ randomly selected from $0.1R_{\infty G}$ to $R_{\infty G}$ (since I_{m2} is lower than I_{m1} , the resistance R_∞ must be lower than $R_{\infty G}$),
- R_1 randomly selected from $0.1R_{1G}$ to $10R_{1G}$,
- α randomly selected from 0.6 to 1,
- F randomly selected from $0.1C_G$ to $10C_G$.

The resulting X parameters are then taken from the run with the lowest *LSE*. The pseudocode of the proposed method is presented in Algorithm 5.1.

Algorithm 5.1 Pseudocode of the parameter extraction method

```

Input: abf datafile,  $C_G$ 
Output:  $X_{\text{final}}$ ,  $LSE_{\text{final}}$ ,  $i_{\text{final}}$ 
load Data from recorded abf datafile by abf2load function
RecCur  $\leftarrow$  current waveform shifted to base position, i.e.  $I_h = 0$ ,  $t_0 = 0$  and selected 60 log-spaced samples between  $t_s$  and  $t_f$  ( $t_s$  determined empirically from graph)
 $V_m$ ,  $I_{m2}$ ,  $I_s \leftarrow$  detect values from Data and RecCur
for  $i = 1$  to 100
  Guess  $\leftarrow$  generate random initial guess of  $X$  parameters
  minimize the LSE error (eq. (5.8)) using fminsearch function with initial Guess
  if actual LSE is lower than LSE from previous cycle
     $X_{\text{final}} \leftarrow X$ 
     $LSE_{\text{final}} \leftarrow LSE$ 
  end if
end for
 $i_{\text{final}} \leftarrow$  compute current response (eq. (5.6)) using  $X_{\text{final}}$ 
display  $X_{\text{final}}$ ,  $LSE_{\text{final}}$ ,  $i_{\text{final}}$ 

```

5.1.3 Results and Discussion

To verify the proposed method, the records of membrane current responses in rat cardiomyocytes to voltage rectangular pulse in Tyrode solution are used [112], [113]. The measurement has been performed by the setup described in Subsection 5.1.1 and averaged from last 20 pulses of a batch of total 200 pulses.

Since the techniques of cell capacitance measurement are usually based on the application of small subthreshold voltage steps around the resting membrane voltage of the cell, the voltage levels of the rectangular stimulus signal are chosen -80 mV and -75 mV, thus the amplitude V_m is 5 mV. This limited amplitude prevents membrane depolarization and ensures constant parameters of the membrane electrical model shown

in Fig. 5.2. If the membrane was depolarized, the voltage-dependent ionic channels would be activated and the capacitance of cell membrane could not be measured [109].

The positive pulse width ($t_f - t_0$) of the imposed voltage is 20 ms and sampling time is 5 μ s. The transient response of the recorded current with the initial point (t_0, I_h) shifted to zero is shown in black in Fig. 5.4. The circle marker on the trace indicates the sample at the time $t_s = 185 \mu$ s where the initial transient event decayed and from which the response was subjected to processing. A logarithmic scale is used on the horizontal axis for better visibility of the waveforms at the time period close to origin.

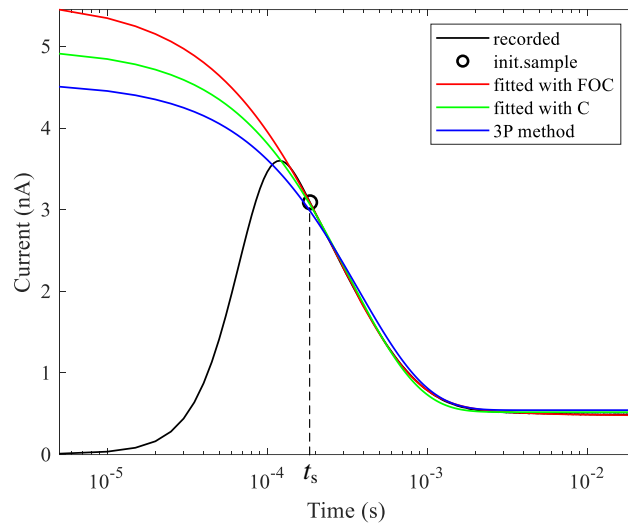


Fig. 5.4 Current transient responses: recorded (black), fitted with FOC (red), fitted with classic capacitor (green), and response with model parameters detected by 3P method [117] (blue)

The red line in Fig. 5.4 represents the current response computed by the relation (5.6) corresponding to the Cole model with FOC and other parameters detected by the described fitting method. A very good agreement with the measured black response can be observed. Comparison of the results with the model corresponding to the Cole circuit but containing classic capacitor is also present. The parameters of this IO model are extracted by two methods. The first one employs the fitting procedure presented in this work, however the relation (5.7) instead of (5.6) is used in the *LSE* computation for the *fminsearch* function. The response resulting from this method is shown by green line in Fig. 5.4. The second method used for comparison stems from the work [117] where a three-point (3P) approach for detecting the model parameters is proposed. The element values computed by the 3P method and substituted into (5.7) result in the blue response in Fig. 5.4. The curves in Fig. 5.4 differ most from each other in the initial times, below 100 μ s. However, we have to recall that the fitting could be done first in the observed steady state starting with the circled initial sample at $t_s = 185 \mu$ s. For higher times (after the initial sample), the curves begin to converge, but the differences between them are

still noticeable. To better assess the results in this area, the relative errors of the fitted current responses against the recorded one are plotted in Fig. 5.5.

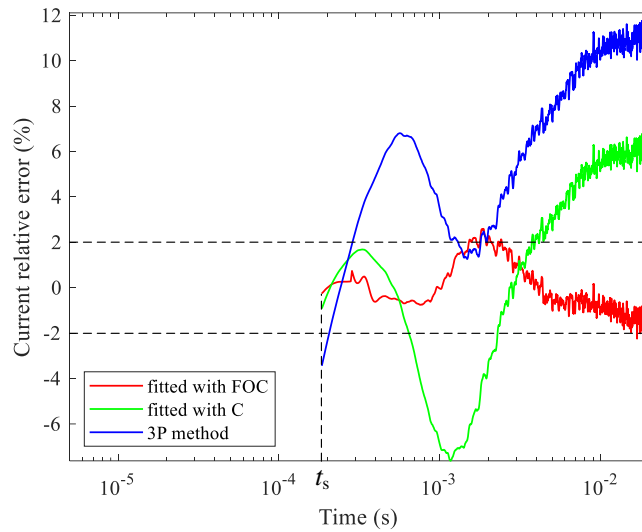


Fig. 5.5 Relative errors of responses fitted with FOC (red), fitted with classic capacitor (green), and model parameters detected by 3P method [117] (blue) against the recorded response

It is apparent from the graph that the response obtained with Cole model with FOC and parameters extracted by the proposed method results in the lowest relative error mostly below $\pm 2\%$. The error of the model with extracted classic capacitance reaches its worst-case value of -7.6% and the model corresponding to the 3P method provides the highest error about 12% . Note that at the times lower than t_s , it is not possible to evaluate the relative error because this interval is affected by the initial transient event. The extracted model parameters, LSE values and maximum absolute values of the relative errors for the three considered methods are summarized in Tab. 5.1.

Table 5.1 Extracted parameter values and errors for the considered extraction methods

Method	Extracted model parameters				LSE (A^2)	Max. abs. relative error (%)
	R_∞ ($M\Omega$)	R_1 ($M\Omega$)	F or C	α		
This work FOC	0.8979	9.609	582.0 pF \cdot s $^{\alpha-1}$	0.9363	$2.508\cdot 10^{-21}$	2.599
This work classic cap.	1.004	8.612	366.0 pF	1	$4.109\cdot 10^{-20}$	7.626
3P method [117]	1.096	8.091	384.2 pF	1	$2.256\cdot 10^{-19}$	12.11

From Tab. 5.1, it is seen that the three methods differ even more when compared in terms of the *LSE* parameter. Regarding *LSE*, the described method with FOC is again the best, followed by the same method with classic capacitor and the 3P method.

It can be concluded that the Cole model containing FOC is able to better approximate the recorded current response compared to the corresponding models with classic capacitor. The extracted value of fractional order α is 0.9363, which may appear to be close to the value of 1 of a classic capacitor, but the maximum relative approximation error of the current response is reduced approximately three times when using FOC instead of classic capacitor. The method proved to be very robust, as it is able to deal with a recorded current response where it is not possible to perform the fitting from the beginning of the rise time due to the initial parasitic transient event.

From the relatively high detected α value close to 1, it can be presumed that the membrane has a geometrically simple structure close to the arrangement of a classic capacitor. A lower α value can be expected for more morphologically complex structures. A lower α value was also observed when measuring responses of entire tissues composed of many cells, where numerous intracellular, extracellular, and cellular membrane resistances and capacitances appear. As the parameter α is also referred to a dispersion coefficient, it may be considered as a measure of heterogeneity of cell sizes and shapes [10].

Future research may address the relationship between the detected α value and various cell membrane properties. For example, the mentioned connections with the morphological complexity of the membrane or its various pathological phenomena can be investigated.

6. FO ANALOG FREQUENCY FILTERS

As discussed in Section 2.2 dealing with state of the art, FO frequency filters provide more general characteristics compared to their IO counterparts. Above all, it is a possibility to adjust the slope of the magnitude frequency response continuously, not only in steps defined by an integer order. This is also related to the possibility of fine-tuning the phase frequency response, group delay and time characteristics such as the step response. Section 2.2 also stated that numerical methods are used to find the coefficients of FO filter TF so as to minimize the deviation of the filter magnitude frequency response from the selected target function, e.g. according to maximally flat Butterworth. These methods can lead either to a true s -domain FO TF, or to a TF of higher integer order approximating the fractional behavior. The author of this work dealt particularly with the first approach and his main contributions in this field are described in detail in the following Sections 6.1, 6.2, 6.3, 6.4.1, and 6.4.2. However, he also dealt with the second approach, i.e. the search for IO TF approximating different types of FO filter functions. As he participated in these works as a co-author, their content will be only briefly described in the Subsection 6.4.3.

6.1 FO Filters with Arbitrary Quality Factor

When considering the design of IO TF to realize filtering functions, obtaining the TF coefficients is very well described. On the other hand, getting the coefficients of FO TFs is not yet elaborated as deeply. Thus, there is a need to improve the methods of obtaining these coefficients for various FO TFs to improve their usability. In the work [52], the author of this thesis contributed to this topic by presenting design equations and coefficients of three FO LP TFs to aid in their design based on their arbitrary quality factor Q . The coefficients are found by minimizing the error between these FO TFs and the second-order TF using numerical optimization.

6.1.1 Transfer Functions and Coefficient Search

FO LP filters of order $(1 + \alpha)$, where $0 < \alpha < 1$, are typically designed by replacing the classic capacitor(s) in active second-order filter topologies by FOC as demonstrated e.g. in [44]. After this substitution the TFs of these FO circuits are determined, which can take different forms depending on which of the two capacitors were replaced (first, second, or both). Three general forms of FO TFs, resulting from different replacements, are given by

$$H_{1+\alpha}^{\text{LP-A}}(s) = \frac{1}{b_{A0} + s^\alpha b_{A1} + s^{1+\alpha} b_{A2}}, \quad (6.1)$$

$$H_{1+\alpha}^{\text{LP-B}}(s) = \frac{1}{b_{B0} + sb_{B1} + s^{1+\alpha}b_{B2}}, \quad (6.2)$$

$$H_{1+\alpha}^{\text{LP-C}}(s) = \frac{1}{b_{C0} + s^{\alpha_2}b_{C1} + s^{\alpha_1+\alpha_2}b_{C2}} = \frac{1}{b_{C0} + s^{0.5(1+\alpha)}b_{C1} + s^{1+\alpha}b_{C2}}, \quad (6.3)$$

where in (6.3) the FOC orders α_1 and α_2 are the same for simplicity and it holds $\alpha_1 + \alpha_2 = 1 + \alpha$. The TFs given by (6.1) and (6.2) correspond to cases when only one capacitor is replaced with its FO counterpart, with (6.3) corresponding to when both are replaced. These TFs describe LP filters with fractional orders between one and two. When designing a filter using (6.1) – (6.3), the coefficients b_{A0} , b_{A1} , b_{A2} , b_{B0} , b_{B1} , b_{B2} , b_{C0} , b_{C1} , and b_{C2} should be appropriately selected to obtain the desired characteristics (bandwidth, roll-off, quality factor, etc.) that meet the designers' specifications.

The second-order LP TF with a unity pole angular frequency (1 rad/s) is given by

$$H_2^{\text{LP}}(s) = \frac{1}{s^2 + s\frac{1}{Q} + 1}. \quad (6.4)$$

This TF provides gain equal to the quality factor Q at the pole frequency and thus it is possible to obtain magnitude characteristics with a peaking around the pole frequency for $Q > 0.707$ or a flat characteristic for lower Q . To approximate (6.4) for an arbitrary quality factor, the coefficients b of (6.1) – (6.3) were obtained in MATLAB by applying the *fminsearch* function. The following relation expressing *LSE* was the argument of this function

$$LSE = \sum_{i=1}^M \left[\left| H_{1+\alpha}^{\text{LP}}(X, \omega_i) \right| - \left| H_2^{\text{LP}}(\omega_i) \right| \right]^2, \quad (6.5)$$

where X is the sought vector of the coefficients $[b_{A0}, b_{A1}, b_{A2}]$, $[b_{B0}, b_{B1}, b_{B2}]$, or $[b_{C0}, b_{C1}, b_{C2}]$ according to the respective TF (6.1) – (6.3); $\left| H_{1+\alpha}^{\text{LP}}(X, \omega_i) \right|$ is the magnitude of the $(1 + \alpha)$ FO TF (6.1) – (6.3) calculated using X at the frequency ω_i . This search used $M = 100$ frequency points logarithmically spaced from $\omega_1 = 0.01$ rad/s to $\omega_{100} = 1.4$ rad/s. The upper frequency bound was chosen higher than 1 rad/s to include the entire pass-band peak of the biquad magnitude response for the higher Q cases. This provides better approximation accuracy for TFs with higher Q especially for lower values of α .

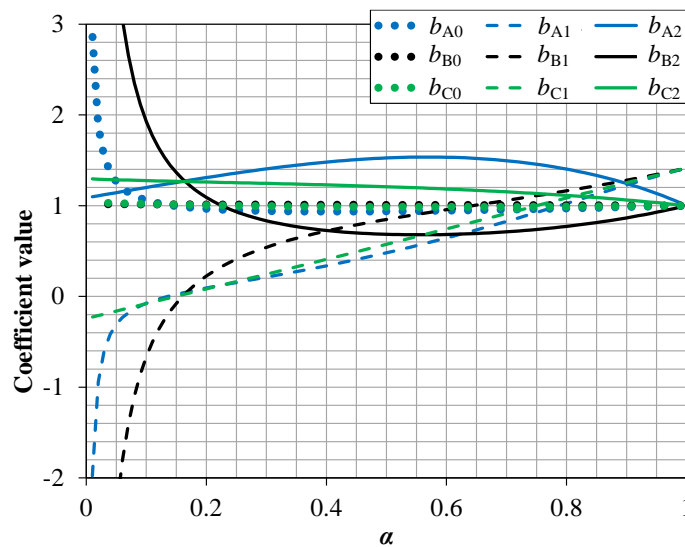
It should be noted that the fractional- and second-order TFs can be substituted into the optimization process also as logarithmic magnitudes (in dB). The logarithmic scale can be more convenient especially when approximating the TFs with high quality factor which feature extremely high magnitudes within the approximation frequency band. The linear scale brings increased accuracy in the area of the peak of the characteristic in this

case, however it can cause higher errors (in dB) at low frequencies where the gain should be around unity.

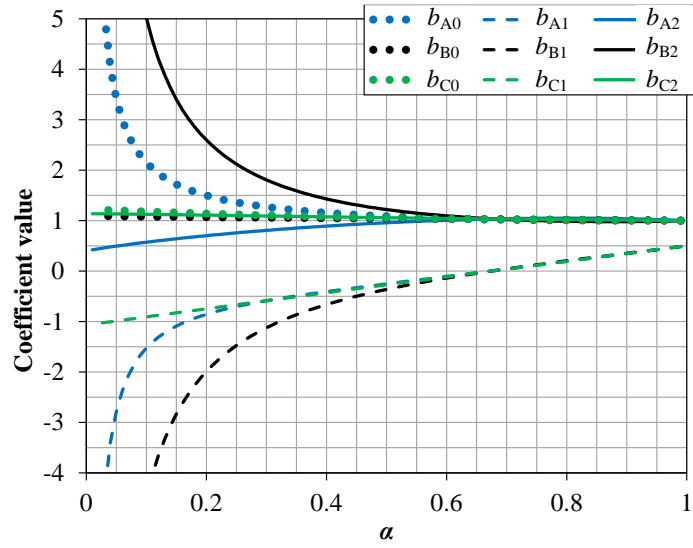
6.1.2 Results and Discussion

The resulting coefficients b that yielded the lowest LSE according to (6.5) for the TFs (6.1) – (6.3) when the order is increased from 1.01 to 1.99 (i.e. α from 0.01 to 0.99) in steps of 0.01 are given in Figs. 6.1 (a), (b), (c) for $Q = 0.707, 2,$ and 5 respectively.

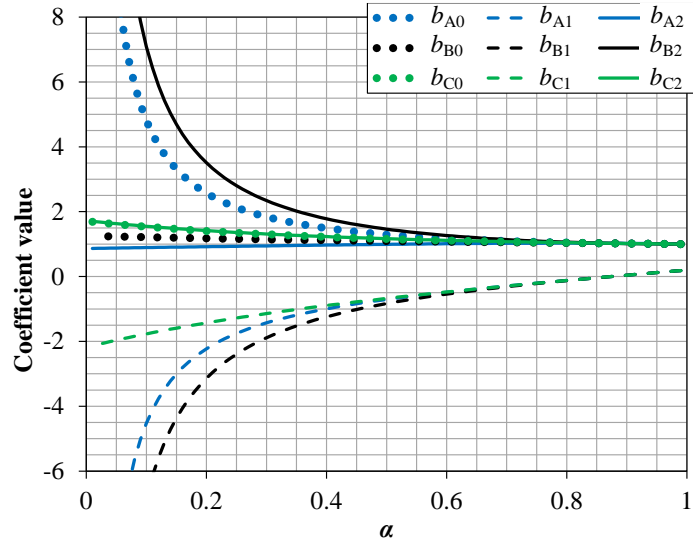
It is apparent from the graphs that the coefficients $b_{A0}, b_{B0}, b_{C0}, b_{A2}, b_{B2},$ and b_{C2} converge to the value one as α approaches 1 and the coefficients $b_{A1}, b_{B1},$ and b_{C1} tend to the value $1/Q$ for high values of α , i.e. for the fractional filter order close to two. This is in agreement with the values of coefficients of the second order TF (6.4). Both coefficients b_{B0} and b_{C0} remain close to one across the whole range of α . This indicates that the pass-band gain is also approximately one for these cases. It also signifies that the TFs (6.2) and (6.3) would approximate (6.4) fairly well also with the coefficients b_{B0} and b_{C0} fixed to one, especially for low Q . On the other hand, the coefficient b_{A0} deviates from one for low α and high Q . Thus, in this case a more distinct deviation of the low-frequency gain from unity can be expected using TF (6.1). The values of b_1 coefficients decrease with decreasing α and increasing Q . Probably the most interesting phenomenon in Fig. 6.1 is that the b_1 coefficients have negative values which are most apparent for high Q and low α . This can evoke doubts regarding the stability of these TFs with such values. It is shown in the source paper [52] that these functions are stable for all coefficient values determined here.



(a)



(b)



(c)

Fig. 6.1 Coefficients b to approximate second-order magnitude response using (6.1) – (6.3) as blue, black, and green lines, respectively, for: (a) $Q = 0.707$; (b) $Q = 2$; (c) $Q = 5$

The interpolated fourth-order equations that describe the coefficients b for (6.1) – (6.3) found using the optimization process as functions of α and Q determined using the numerical data are given by the matrix equation (6.6). The equations given by (6.6) can be used for computing the coefficients b with good accuracy for any Q from 0.5 to 5 and any α from 0.2 to 0.99 (or even in a higher range, see below). In these intervals the maximum errors between b predicted by (6.6) and original b values obtained by the *fminsearch* function are [0.0803, 0.22, 0.266], [0.00682, 0.323, 0.149], and [0.00508, 0.167, 0.23] for $[b_{A0}, b_{A1}, b_{A2}]$, $[b_{B0}, b_{B1}, b_{B2}]$, and $[b_{C0}, b_{C1}, b_{C2}]$ respectively. These

maximum errors occur at the borders of the intervals of Q and α considered. The error is lower in most cases which is illustrated by the average errors of b : [0.00692, 0.0181, 0.0361], [0.000145, 0.0329, 0.0159], and [0.0004, 0.0196, 0.0228].

$$\begin{pmatrix} b_{A0} \\ b_{A1} \\ b_{A2} \\ b_{B0} \\ b_{B1} \\ b_{B2} \\ b_{C0} \\ b_{C1} \\ b_{C2} \end{pmatrix} = \begin{pmatrix} 0.8318 & 0.9584 & -2.3994 & -0.0663 & -2.8642 & 9.9409 & 9.548e-3 & 0.03557 & 3.4256 & -13.31 & -5.76e-4 & -3.02e-3 & 6.92e-3 & -1.5025 & 5.9709 \\ 0.6714 & -2.0255 & 3.3238 & 0.6183 & 1.3900 & -8.088 & -0.1544 & 0.5546 & -3.9013 & 13.381 & 0.0141 & -0.0583 & 2.01e-3 & 1.6753 & -6.3503 \\ 2.9149 & -3.7867 & 1.6699 & 1.9276 & 0.5393 & -2.125 & -0.3869 & -0.4862 & 1.0757 & -0.142 & 0.0270 & 0.0722 & -0.1854 & 0.2115 & -0.3731 \\ 0.9787 & 0.0515 & 0.0347 & 5.478e-3 & -0.0837 & -2.16e-3 & -1.39e-3 & -4.31e-3 & 0.0483 & -0.0153 & 8.34e-5 & 5.76e-4 & 1.43e-3 & -0.0192 & 5.31e-3 \\ 1.704 & -6.6418 & 12.480 & 2.3437 & 7.0029 & -34.95 & -0.426 & -0.8742 & -5.7911 & 39.056 & 0.0300 & 0.04687 & 0.28763 & 1.7890 & -15.061 \\ 1.065 & 3.691 & -12.362 & -0.9675 & -6.5732 & 35.553 & 0.13734 & 0.8258 & 5.3522 & -38.892 & -7.64e-3 & -0.0524 & -0.1895 & -1.9576 & 15.437 \\ 0.9078 & 0.1795 & 0.0341 & -8.17e-3 & -0.3153 & 0.1406 & 1.03e-3 & -5.11e-3 & 0.2359 & -0.1944 & -8.74e-5 & 2.87e-4 & 7.18e-3 & -0.0906 & 0.1088 \\ 0.9886 & -2.2696 & 1.7433 & 0.9810 & -0.6165 & 0.4801 & 0.2223 & 0.4205 & -0.5391 & 0.1536 & 0.01848 & -0.0411 & -0.0306 & 0.2635 & -0.2588 \\ 2.2395 & -1.9628 & -0.1341 & 1.0724 & 0.4850 & -0.6080 & -0.2163 & -0.3792 & 0.5756 & -0.0889 & 0.01509 & 0.04649 & -0.0434 & -0.0642 & 0.03505 \end{pmatrix} \cdot \begin{pmatrix} 1 \\ Q \\ \alpha \\ Q^2 \\ Q\alpha \\ \alpha^2 \\ Q^3 \\ Q^2\alpha \\ \alpha^3 \\ Q^4 \\ Q^3\alpha \\ Q^2\alpha^2 \\ Q\alpha^3 \\ \alpha^4 \end{pmatrix} \quad (6.6)$$

To quantify the differences between each TF realizing the LP responses for arbitrary Q and α , the maximum errors between (6.4) and (6.1) – (6.3) were computed according to the relation

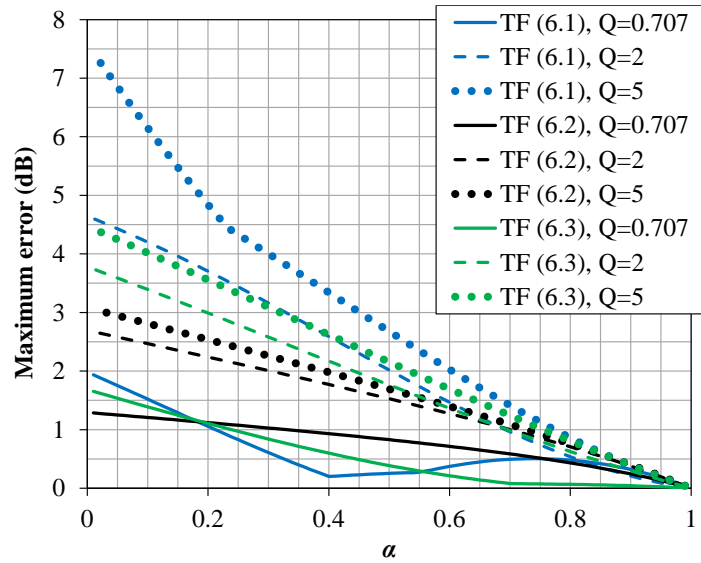
$$\max_{i=1}^M \left\{ \left| 20 \log \left| H_{1+\alpha}^{\text{LP}}(X, \omega_i) \right| - 20 \log \left| H_2^{\text{LP}}(\omega_i) \right| \right| \right\}. \quad (6.7)$$

These maximum errors are shown in Fig. 6.2 for $Q = 0.707, 2, \text{ and } 5$ for $\alpha = 0.01$ to 0.99 in steps of 0.01 . Fig. 6.2(a) demonstrates these errors using the original coefficients b found by the *fminsearch* function whereas Fig. 6.2(b) utilizes b values given by (6.6). This error is computed using the pass-band frequencies of the optimization search, that is $\omega_i = 0.01$ rad/s to 1.4 rad/s with 100 logarithmically spaced datapoints ($M = 100$).

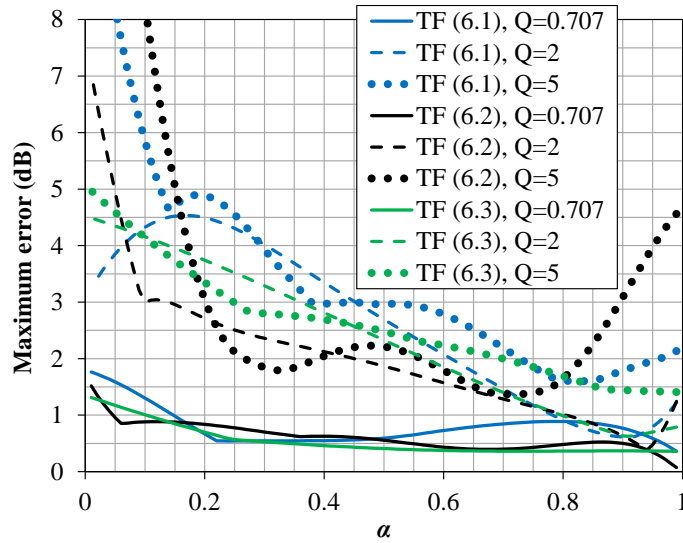
As seen in Fig. 6.2(a), the approximations found by *fminsearch* are most accurate for α close to one and for lower values of Q (given by the solid lines). Though for each TF, the error increases as the value of Q is increased. The TF (6.2) has the lowest relative error even for small values of α and high Q , making it the most appropriate of the three TFs for these situations. Alternatively, the TF (6.1) is the least suitable for approximating high Q transfer functions with the largest relative error for this case. In Fig. 6.2(b) the influence of using (6.6) for computing the b coefficients is apparent. The resulting errors from both graphs (a) and (b) are almost the same for $Q = 0.707$. For Q higher than 2 the error increases, especially at the borders of the α values which is most distinct for the function (6.2) and least distinct for (6.3). This is in agreement with Fig. 6.2(c) where the traces are most curved for b values from (6.2) whereas they are almost linear for b values from (6.3).

Fig. 6.2(b) also shows that the relation (6.6) can be used for computing the b values also for α lower than 0.2 in some cases, while maintaining the approximation error low. For low values of Q up to approx. 1.5 , (6.6) is valid in the full range of α . and no significant increase of error occurs. In the case of computing the coefficients b_{C0}, b_{C1}, b_{C2}

for (6.3), the eq. (6.6) is valid even in full ranges of α and Q considered, i.e. from 0.01 to 0.99 and from 0.5 to 5 respectively.



(a)



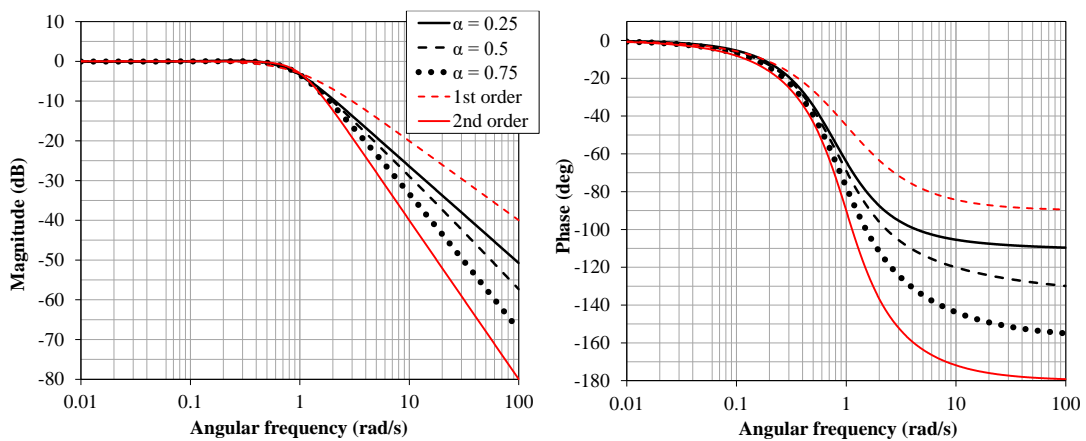
(b)

Fig. 6.2 Maximum errors of approximation of (6.4) by (6.1), (6.2), and (6.3) as blue, black, and green lines, respectively; for $Q = 0.707, 2,$ and 5 as full, dashed, and dotted lines respectively: (a) values of b found by *fminsearch*; (b) values of b approximated by (6.6)

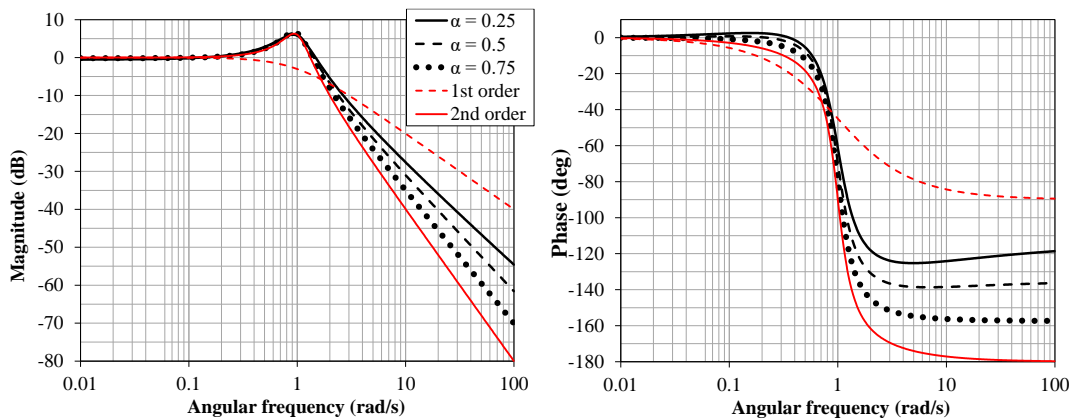
For all further references to (6.1), (6.2), and (6.3) throughout this section, unless stated otherwise, it can be assumed that the coefficients b computed by (6.6) are being used in their respective TFs. Thus, the combination of the following two errors affect the results: one originated from using the *fminsearch* function to approximate the second-order TF and the second due to computing the b coefficients by the fitting polynomials in (6.6). This approach was chosen because readers of this thesis will probably more frequently

use (6.6) than create their own MATLAB script that provides more accurate b coefficients by the search of the minimum error between the TFs.

To confirm that the TF given by (6.2) realizes the expected LP response using the coefficients computed by (6.6), MATLAB simulations of the magnitude and phase responses are given in Fig. 6.3 from 0.01 rad/s to 100 rad/s. These simulations present the cases where $\alpha = 0.25, 0.5,$ and 0.75 (as solid, dashed, and dotted black lines) when $Q = 0.707, 2,$ and 5 in Figs. 6.3 (a), (b), and (c), respectively. Only one TF (6.2) is presented here to improve the clarity of comparison against the IO cases. The magnitude and phase responses of the second-order TF given by (6.4) with the respective quality factor and the first-order TF given by $H(s) = 1/(s + 1)$ are also depicted as solid and dashed red lines, respectively, for comparison. These simulations confirm that the FO magnitude response has a low deviation from the second-order response in the pass-band. In accordance with Fig. 6.2(b) the maximum gain error is less than 2.5 dB for all values of quality factor and filter order. The phase characteristics increase their slope around the cut-off frequency with increasing Q as expected. The phase values at high frequencies in the stop-band tend to $-112.5^\circ, -135^\circ,$ and -157.5° for $\alpha = 0.25, 0.5,$ and 0.75 respectively which is also in accordance with theory.



(a)



(b)

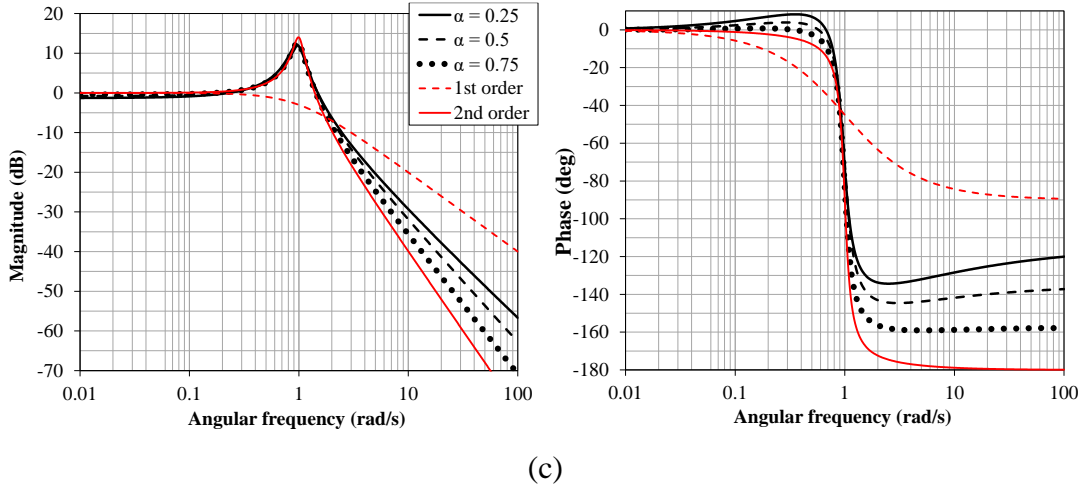


Fig. 6.3 Magnitude and phase of TF (6.2) vs frequency for $\alpha = 0.25, 0.5,$ and 0.75 : (a) $Q = 0.707$; (b) $Q = 2$; (c) $Q = 5$

The TF coefficients b were found to approximate the second-order TF (6.4) with a pole (or characteristic) angular frequency of 1 rad/s. Thus, the FO TFs are considered prototype having characteristic angular frequency approximately equal to 1 rad/s. However, designers must be able to frequency shift the response of the filter to meet the specifications of their target application. If the characteristic frequency of the FO TFs needs to be shifted to an arbitrary value ω_0 then (6.1) to (6.3) can be written as

$$H_{1+\alpha}^{\text{LP-A}}(s) = \frac{1}{b_{A0} + s^\alpha \frac{b_{A1}}{\omega_0^\alpha} + s^{1+\alpha} \frac{b_{A2}}{\omega_0^{1+\alpha}}}, \quad (6.8)$$

$$H_{1+\alpha}^{\text{LP-B}}(s) = \frac{1}{b_{B0} + s \frac{b_{B1}}{\omega_0} + s^{1+\alpha} \frac{b_{B2}}{\omega_0^{1+\alpha}}}, \quad (6.9)$$

$$H_{1+\alpha}^{\text{LP-C}}(s) = \frac{1}{b_{C0} + s^{\alpha_2} \frac{b_{C1}}{\omega_0^{\alpha_2}} + s^{\alpha_1+\alpha_2} \frac{b_{C2}}{\omega_0^{\alpha_1+\alpha_2}}} = \frac{1}{b_{C0} + s^{0.5(1+\alpha)} \frac{b_{C1}}{\omega_0^{0.5(1+\alpha)}} + s^{1+\alpha} \frac{b_{C2}}{\omega_0^{1+\alpha}}}. \quad (6.10)$$

From these relations it should be noted that the coefficients b with subscripts 1 and 2 should be divided by the appropriate power of ω_0 to properly frequency scale the filter response.

6.1.3 Circuit Implementation and Simulation

To verify the previous results, computer simulations of a FO LP filter were carried out in the OrCAD PSpice design environment. For these simulations, a quality factor of $Q = 5$ and fractional order of 1.5, i.e. $\alpha = 0.5$, were selected. Additionally, TF given by (6.2)

was selected because it provides the lowest error of approximation for these values of Q and α . The characteristic angular frequency was shifted to $\omega_0 = 10$ krad/s and the resulting semi-symbolic TF after this scaling is

$$H_{1+\alpha}^{\text{LP-B}}(s) = \frac{1}{1.0965 - s \cdot 7.6738 \cdot 10^{-5} + s^{1.5} \cdot 1.4307 \cdot 10^{-6}}. \quad (6.11)$$

Note the negative coefficient for the s term in the denominator of (6.11) due to the high quality factor. This LP filter response was implemented with two Differential Voltage Current Conveyors (DVCC) [118], two resistors, one IO capacitor C_1 , and one FOC F_2 as shown in the circuit of Fig. 6.4.

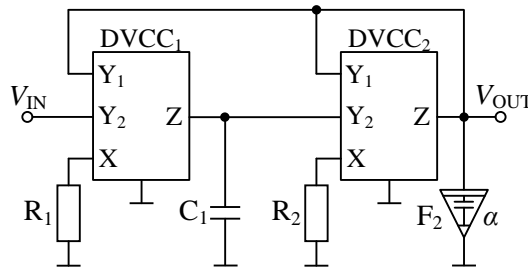


Fig. 6.4 Fractional-order filter with DVCCs

The following relations define the ideal behavior of the four-terminal DVCC: $I_{Y1} = I_{Y2} = 0$, $V_X = V_{Y1} - V_{Y2}$, $I_Z = I_X$. Here the terminal voltages are referenced to ground and the terminal currents are taken as positive when flowing into the element. The TF of the circuit in Fig. 6.4 is given by

$$\frac{V_{\text{OUT}}(s)}{V_{\text{IN}}(s)} = \frac{1}{1 - sR_1C_1 + s^{1+\alpha}R_1R_2C_1F_2}, \quad (6.12)$$

which has the same form as (6.11) and also contains the negative sign for the s term. The circuit can be easily modified to have positive sign at the term with s , achieved by interchanging the terminals Y_1 with Y_2 of both conveyors. The element values required to realize our target filter were computed by comparing the denominators of the TFs (6.11) and (6.12). Note that the circuit provides exactly unity pass-band gain whereas the function (6.11) has the pass-band gain slightly lower than one due to the denominator absolute term higher than one. This difference can be usually neglected as the absolute term b_{B0} (as seen e.g. in Fig. 6.1) is close to one for most values of Q and α considered. If an exact match is required, a block with voltage gain $1/b_{B0}$ should be added in cascade with the filter. Comparing the TFs (6.11) and (6.12) and choosing $R_1 = R_2 = 10$ k Ω the resulting capacitor values are $C_1 = 7.674$ nF, $F_2 = 1.864$ $\mu\text{F} \cdot \text{s}^{\alpha-1}$ and $\alpha = 0.5$.

Simulating FOC using available circuit simulation packages typically requires replacement of this element with RC ladder emulation circuits whose parameters are computed to approximate the impedance characteristics of the element over a target

frequency band [25]. An alternative technique to simulate FOE is possible in OrCAD utilizing the GFREQ behavioral block [119]. This block is a voltage-controlled current source whose transconductance frequency response is given by a table of frequencies and respective magnitudes (in dB) and phases (in degrees). A grounded FOE can be obtained by connecting the GFREQ block as shown in Fig. 6.5. The table of this block contains a set of discrete points of the frequency characteristic of the FO admittance that it models, i.e. for a frequency f and the pseudo-capacitance F_2 the gain is $20\log[(2\pi f)^{\alpha}F_2]$, and the phase is 90α . In the case of ideal FOE modeling it is enough to input two discrete points: one at the start frequency of interest and one at the stop. The values at frequencies in between are computed automatically. For the purpose of these simulations, the following text was used as the parameter TABLE of GFREQ: (1,-106.61,45) (1G,-16.61,45).

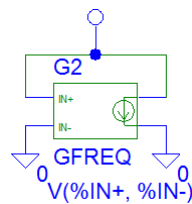


Fig. 6.5 Grounded FOE implemented by GFREQ block in OrCAD

The DVCC element with the grounded resistor connected to its terminal X is emulated in these simulations by the connection of the commercially available integrated circuit AD844. The overall implementation of the DVCC by two AD844s is shown in Fig. 6.6 [120].

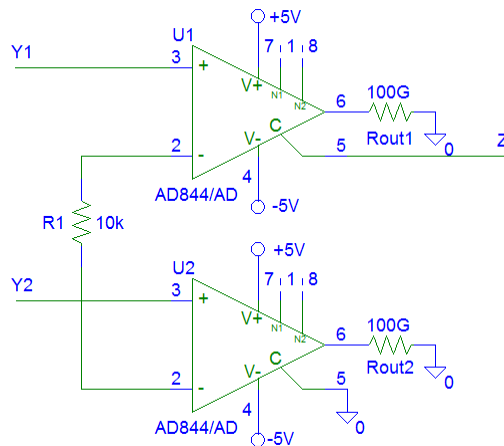


Fig. 6.6 Implementation of DVCC₁ with R₁ by two AD844s

The magnitude and phase characteristics of the filter with AD844s compared to the MATLAB simulations of the ideal response given by (6.11) are depicted in Fig. 6.7 as solid and dotted lines, respectively.

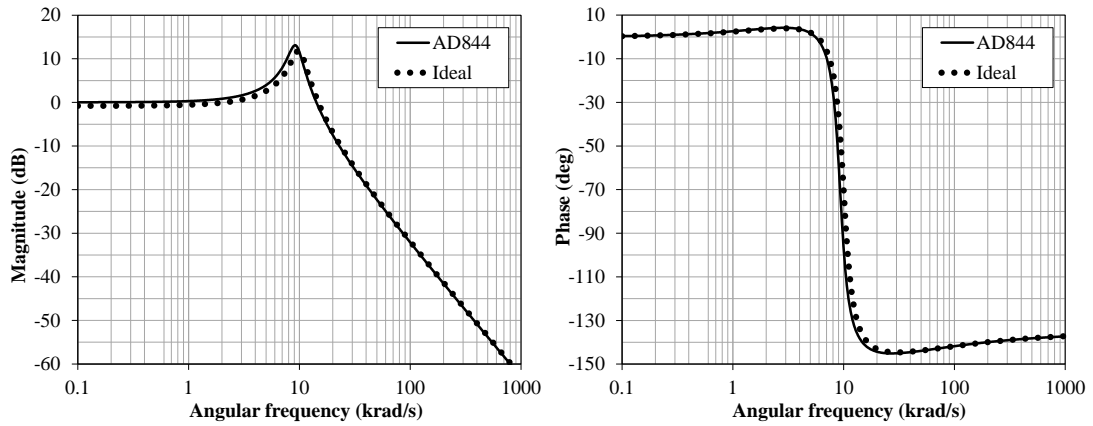


Fig. 6.7 Simulated (solid) and ideal (dotted) magnitude and phase characteristics of the LP filter of the order 1.5 and $Q = 5$

The magnitude and phase characteristics of the filter with DVCCs emulated by AD844 are in a very good agreement with the ideal ones. The slope of the magnitude characteristic in the stop-band is -30.7 dB/dec and -30.9 dB/dec in the case of the filter with AD844 and ideal function (6.11), respectively, which corresponds to the theoretical value -30 dB/dec for 1.5-order filters. The low-frequency pass-band gain of the simulated filter is 0.8 dB higher compared to the value from (6.11) as already discussed. The peaks of the magnitude characteristics reach 13.1 dB and 12.6 dB in the case of the filter with AD844 and ideal function (6.11), respectively. The second-order filter with $Q = 5$ would have the peak 14 dB.

6.1.4 Concluding Remarks

This section has shown that FO TFs with orders between one and two are capable of approximating the quality factor in the pass-band typical of second-order TFs. The maximum value of Q considered was 5 but the optimization search method can be further applied for higher values. The error when comparing the FO response to the second-order response that it approximates increases with higher quality factor, but can stay below several dB for most FO values considered and suitable selection of FO TF. The function (6.2) is the most accurate for high quality factors. It is recommended for each designer to use MATLAB or other software tools to compute the TF coefficients b for particular values of Q and α that may not be considered here.

6.2 FO Band-Pass Filters with Adjustable Slope

Most of the works on FO analog frequency filters published so far is focused largely on LP TFs, with little attention on the investigation of other kinds of FO filter TFs, such as HP or BP. In the works that have investigated FO HP and BP filters [121], [122], the FO TFs have been obtained after applying transformations from LP and using the coefficients determined for the LP function. While this does realize FO HP and BP filters, in the recent

analysis by the author of this thesis discussed in [123] it is shown that the properties of the FO HP and BP TF (e.g. pass-band ripple of magnitude response, characteristic frequency, pass-band gain, etc.) obtained in this way may not exactly correspond to the original FO LP function. As also demonstrated in [123], in the case of FO HP filter the only correct FO LP to HP transformation that maintains the FO LP properties is the standard substitution of s by $1/s$ in the prototype TF. The HP characteristic is then exactly symmetrical to the LP response with regard to the frequency 1 rad/s. In the case of FO BP filter, the traditional IO transformation can also be used; replacing s in FO LP function with $(s^2 + 1)/(s \cdot BW)$, where BW is the desired bandwidth (in rad/s). This transformation maintains the original LP filter properties, however it leads to doubling the filter order (e.g. the order between one and two increases to the order between two and four), increased circuit complexity and symmetrical slopes of magnitude frequency characteristics below and above center frequency, although these slopes can be set continuously for this kind of filters. It should be noted that in many works by other authors that deal with FO BP filters (for example [92], [124], [125]), the coefficients of the TFs are determined without prior definition of the desired filter specifications.

It is obvious that there is an absence of practical methods for the systematic design of FO BP TFs based on predetermined properties, which motivated the author of this thesis to the research presented in the papers [53] and [126]. In the work [53], FO BP filters of order $(\alpha + \beta)$ composed of two fractional components, with $0 < \alpha \leq 1$ and $0 < \beta \leq 1$, are investigated. These TFs allow continuous and independent adjustment of the magnitude characteristic slopes from 0 to +20 dB/dec below and 0 to -20 dB/dec above the center frequency. The following subsections are based on the paper [53] in which the TF coefficients are presented to achieve desired stop-band characteristics with a flat pass-band for two general FO TFs. The related paper [126] describes simplified FO BP TFs with only one fractional component α and thus allowing setting of only one stop-band slope either below or above the center frequency.

6.2.1 Transfer Functions and Coefficient Search

As already mentioned in the beginning of the Subsection 6.1.1, to obtain a FO filter, the commonly used approach is to transform an IO filter by substituting the traditional IO passive elements within a filter topology with elements that have FO impedance. This transformation has also been applied here to second-order active BP filter circuits where both classic capacitors are replaced by FOCs with impedance $1/(s^\alpha F_\alpha)$ and $1/(s^\beta F_\beta)$, where F_α and F_β are fractances (pseudo-capacitances) and α and β are the orders of each individual element. Replacing the two traditional capacitors with FOCs in a BP filter TF results in one of the following FO TFs:

$$H_{\alpha+\beta}^{\text{BP-A}}(s) = \frac{s^\alpha a_{A0}}{b_{A0} + s^\beta b_{A1} + s^{\alpha+\beta}}, \quad (6.13)$$

$$H_{\alpha+\beta}^{\text{BP-B}}(s) = \frac{s^\alpha a_{\text{B0}}}{b_{\text{B0}} + s^\alpha b_{\text{B1}} + s^{\alpha+\beta}}. \quad (6.14)$$

The coefficients a_{A0} , b_{A0} , b_{A1} , a_{B0} , b_{B0} , and b_{B1} are dependent on the circuit element parameters of the topology selected to realize the required BP TF. Both the TFs (6.13) and (6.14) provide stop-band attenuations of $+20\alpha$ dB/dec and -20β dB/dec for frequencies below and above the center frequency. Thus, these TFs realize asymmetric BP magnitude responses with stop-band attenuations that can be independently controlled through appropriate selection of the FO components (α , β) of the filter.

While the TFs given by (6.13) and (6.14) can realize FO BP responses, it is still necessary to determine the coefficients of these TFs to obtain the desired properties for the filters' specific application. Similarly to the Subsection 6.1.1, a numerical optimization method is applied here such that the error between the FO TF and an appropriate target magnitude response is minimized. This error function is in this BP filter case given by

$$LSE = \sum_{i=1}^M \left[\left| H_{\alpha+\beta}^{\text{BP}}(X, \omega_i) \right| - \left| H_{\text{targ}}^{\text{BP}}(\omega_i) \right| \right]^2, \quad (6.15)$$

where X is the sought vector of the coefficients (a_{A0} , b_{A0} , b_{A1}) or (a_{B0} , b_{B0} , b_{B1}) of the FO TF $H_{\alpha+\beta}^{\text{BP}}$ given by (6.13) or (6.14) and $H_{\text{targ}}^{\text{BP}}$ is the chosen target TF that is to be approximated by $H_{\alpha+\beta}^{\text{BP}}$. This search uses M frequency points in the interval from user defined frequencies ω_1 to ω_M which should be selected to include the filter pass-band. Note that the coefficients b_{A0} , b_{A1} , b_{B0} , b_{B1} in (6.13) and (6.14) resulting from this optimization are different from the equally labelled coefficients appearing in the LP TFs (6.1) – (6.3) in the Section 6.1.

During this optimization process, an important consideration is the selection of the target function $H_{\text{targ}}^{\text{BP}}$, as in the case of a FO BP TF it is not as straightforward as for the FO LP function. While IO BP TFs may be used as the target functions, these functions will always have stop-band attenuations with symmetric integer-step attenuations (i.e. $\pm 20n$ dB/dec) that will influence the fitting procedure. An alternative approach which is pursued here to overcome this challenge is to design target functions that better reflect the required design characteristics (in this case the stop-band attenuations) to improve the coefficients returned by the fitting procedure and subsequent designed filter. The target function proposed for this purpose is given by

$$\begin{aligned} \left| H_{\text{targ}}^{\text{BP}}(\omega) \right|_{\text{dB}} &= \left| H_{\text{BP2}}(\omega) \right|_{\text{dB}} + \left(\left| H_{\text{LP1}}(\omega) \right|_{\text{dB}} - \left| H_{\text{BP2}}(\omega) \right|_{\text{dB}} \right) (1 - \alpha) + \\ &+ \left(\left| H_{\text{HP1}}(\omega) \right|_{\text{dB}} - \left| H_{\text{BP2}}(\omega) \right|_{\text{dB}} \right) (1 - \beta), \end{aligned} \quad (6.16)$$

where $|H_{BP2}(\omega)|_{dB}$ is the magnitude (in dB) of the second-order Butterworth BP TF with center frequency 1 rad/s and pass-band gain -3 dB, $|H_{LP1}(\omega)|_{dB}$ and $|H_{HP1}(\omega)|_{dB}$ are the magnitudes (in dB) of the first-order Butterworth LP and HP TFs, respectively, with cut-off frequency 1 rad/s and pass-band gain 0 dB. This provides $|H_{\text{targ}}^{\text{BP}}(\omega)|_{dB}$ target function that has adjustable stop-band magnitude slopes based on the values of α and β . This target function is equal to the second-order BP magnitude $|H_{BP2}(\omega)|_{dB}$ if $\alpha = \beta = 1$. As α decreases from one to zero in (6.16), the value of $|H_{\text{targ}}^{\text{BP}}(\omega)|_{dB}$ increases at frequencies below 1 rad/s up to the value of $|H_{LP1}(\omega)|_{dB}$ and the lower stop-band slope corresponds to $+20\alpha$ dB/dec. Also, as β decreases from one to zero, $|H_{\text{targ}}^{\text{BP}}(\omega)|_{dB}$ transitions from $|H_{BP2}(\omega)|_{dB}$ to the value of $|H_{HP1}(\omega)|_{dB}$ above 1 rad/s and the upper stop-band slope is -20β dB/dec. Therefore, this target function is able to capture variable and asymmetric FO BP magnitude slopes through weighting of the three IO TF magnitudes by the fractional components α and β . Fig. 6.8 illustrates an example of the $|H_{\text{targ}}^{\text{BP}}(\omega)|_{dB}$ target function with $\alpha = 0.75$ and $\beta = 0.25$ (dotted line) along with the IO individual parts $|H_{LP1}(\omega)|_{dB}$, $|H_{HP1}(\omega)|_{dB}$, and $|H_{BP2}(\omega)|_{dB}$, given as solid green, blue, and black lines, respectively. Notice that the target function has FO slopes of $20\alpha = 15$ dB/dec and $-20\beta = -5$ dB/dec in the low and high frequency stop-bands, respectively, highlighting how the values of α and β are used to obtain the desired stop-band attenuation characteristics.

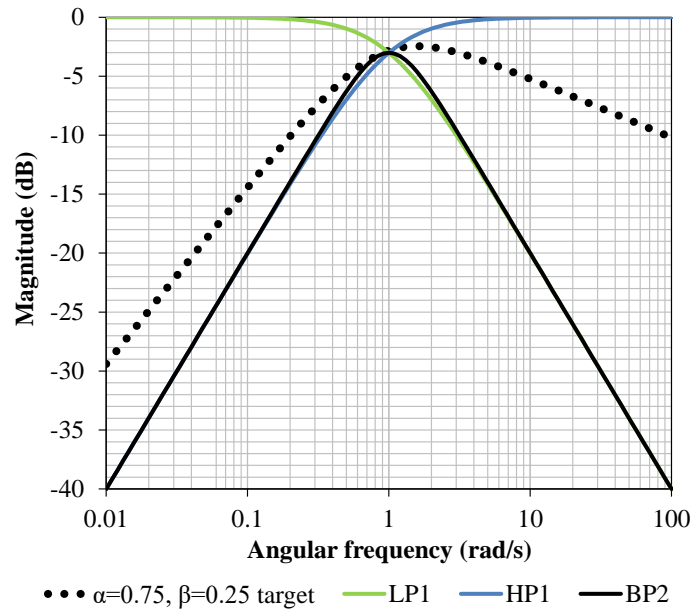


Fig. 6.8 Target function (6.16) given as a dotted line compared to its IO components, specifically the first order LP response (green), first-order HP response (blue), and second-order BP response (black)

Here it should be noted that it is possible to use a target function other than (6.16) for this coefficient search. For example, the second-order Butterworth BP function can be

employed. However, in this case the minimization process must be performed using a sufficiently narrow pass-band around the center frequency. Using a wider frequency band introduces datapoints from the stop-bands with slopes ± 20 dB/dec that cannot be realized with the FO BP TF for the selected fractional order. This results in large error terms at the frequencies of these datapoints in the optimization procedure that has a significant impact on the obtained coefficients; reducing the error at these frequencies will dominate the optimization procedure yielding coefficients that may not be optimal to represent the pass-band of the target function. Hence, using the target function as defined by (6.16) in the optimization process can provide flat FO filter magnitude characteristics which are analogous to the Butterworth characteristics of the IO filters and simultaneously have correct FO stop-band slopes.

To find a set of coefficients that approximate the target function (6.16) for fixed values of α and β , the MATLAB routine *fminsearch* was again used to find the minimum error given by (6.15). Each combination of $0.05 < \alpha, \beta \leq 1$ in 0.01 increments was searched, with $M = 101$ logarithmically spaced datapoints chosen to represent the functions in the frequency range from $\omega_1 = 0.01$ rad/s to $\omega_{101} = 100$ rad/s. By including the unity values of α and β , this search also returned the special cases with one FO component and one IO component. Values of α and β less than 0.05 were not included, as the error from the target function increases for these values and the filter may become unstable. The resulting optimized coefficients for (6.13) and (6.14) can be computed depending on α and β by the following two equations. These equations were created by polynomial fitting the numerical results of the coefficients obtained during the optimization based on (6.15).

$$\begin{pmatrix} a_{A0} \\ b_{A0} \\ b_{A1} \end{pmatrix} = \begin{pmatrix} 0.839 & 1.112 & -0.662 & -0.793 & -0.521 & 1.086 \\ 0.960 & 1.354 & -1.356 & -1.350 & -0.183 & 1.615 \\ -1.002 & 1.253 & 0.400 & 0.056 & -0.166 & 0.982 \end{pmatrix} \cdot \begin{pmatrix} 1 \\ \alpha \\ \beta \\ \alpha^2 \\ \alpha\beta \\ \beta^2 \end{pmatrix}, \quad (6.17)$$

$$\begin{pmatrix} a_{B0} \\ b_{B0} \\ b_{B1} \end{pmatrix} = \begin{pmatrix} 0.918 & -0.353 & 0.709 & 0.507 & -0.179 & -0.605 \\ 1.227 & -2.225 & 1.494 & 1.996 & 0.122 & -1.561 \\ -1.144 & 1.867 & 0.414 & -0.529 & 0.196 & 0.583 \end{pmatrix} \cdot \begin{pmatrix} 1 \\ \alpha \\ \beta \\ \alpha^2 \\ \alpha\beta \\ \beta^2 \end{pmatrix}. \quad (6.18)$$

The average (and maximum in parentheses) absolute interpolation errors of a_{A0} , b_{A0} , b_{A1} , a_{B0} , b_{B0} , and b_{B1} computed from (6.17) and (6.18) against the original values are

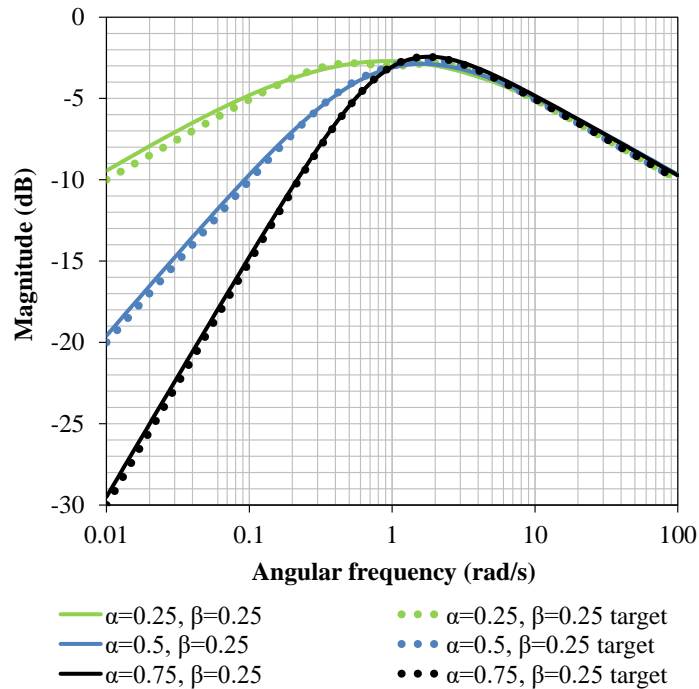
0.082 (1.313), 0.096 (1.315), 0.131 (1.623), 0.054 (1.121), 0.068 (1.101), 0.128 (1.553), respectively for any α and β from the range 0.05 to 1.

It is important to verify the stability of the filters with TFs (6.13), (6.14) and the coefficients determined using (6.17) and (6.18). The stability analysis performed and described in the paper [53] confirmed stable behaviour of the filters for the values α and β from the range 0.05 to 1.

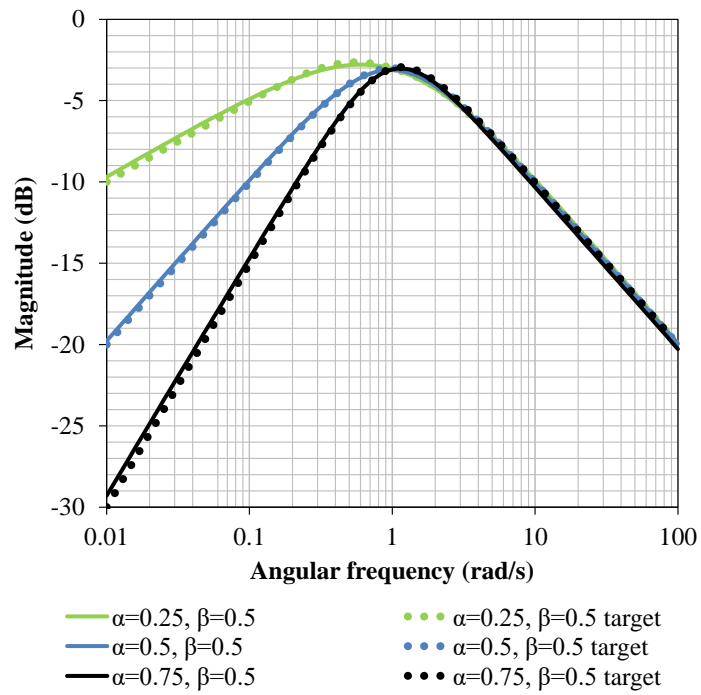
6.2.2 Results and Discussion

To validate that the FO TF given by (6.13) realizes the desired BP filter characteristics, simulations of the magnitude responses of (6.13) with the coefficients from (6.17) are given in Fig. 6.9 for all the combinations of α and β from the set $\{0.25, 0.5, 0.75\}$ as solid lines. For comparison, the target function values given by (6.16) are also shown as dotted lines.

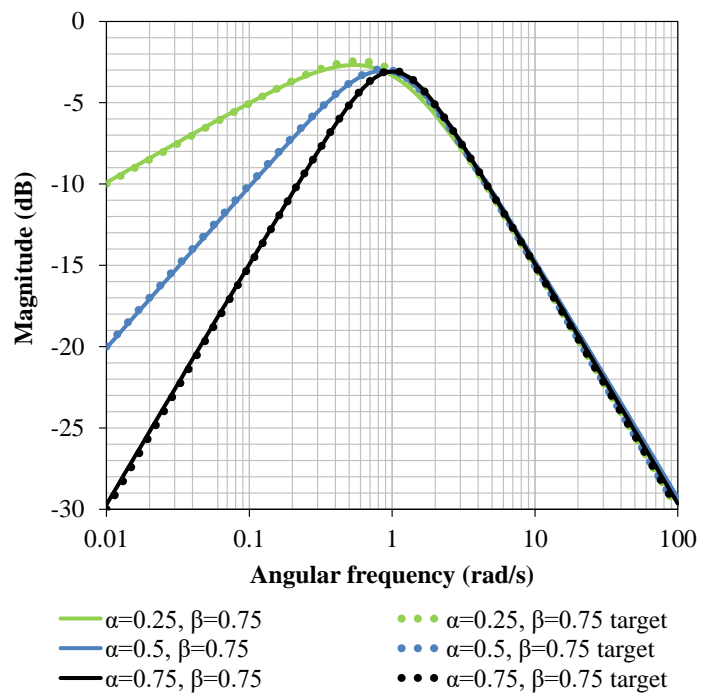
In each case, the simulations of (6.13) using the found coefficients show very good agreement with the target function, confirming the FO asymmetric behavior. To quantify the FO behavior, the stop-band slopes of the TF (6.13) and of the target function (6.16) are summarized in Tab. 6.1. The lower and upper stop-band slopes are identified at frequencies around 0.05 rad/s and 20 rad/s, respectively. The theoretical slopes for the fractional components α and β (i.e. $+20\alpha$ dB/dec in the lower stop-band and -20β dB/dec in the upper stop-band) are also stated for comparison. The stop-band slopes obtained from the magnitude characteristics of (6.13) agree with the slopes of target function (6.16) and the theoretically predicted values. The error is several tenths of dB/dec and thus very small.



(a)



(b)



(c)

Fig. 6.9 Magnitude frequency characteristics of the TF (6.13) with new coefficients from (6.17) (solid lines), and the target function (6.16) (dotted lines) for $\alpha = 0.25$ (green), 0.5 (blue), and 0.75 (black) and (a) $\beta = 0.25$; (b) $\beta = 0.5$; (c) $\beta = 0.75$

Table 6.1 Stop-band slopes (dB/dec) of the TF (6.13), of the target function (6.16), and theoretical slope values

	$\alpha = 0.25$ $\beta = 0.25$	$\alpha = 0.5$ $\beta = 0.25$	$\alpha = 0.75$ $\beta = 0.25$	$\alpha = 0.25$ $\beta = 0.5$	$\alpha = 0.5$ $\beta = 0.5$	$\alpha = 0.75$ $\beta = 0.5$	$\alpha = 0.25$ $\beta = 0.75$	$\alpha = 0.5$ $\beta = 0.75$	$\alpha = 0.75$ $\beta = 0.75$
(6.13) lower stop-band	4.42	9.77	14.69	4.69	9.86	14.53	4.85	9.91	14.70
(6.16) lower stop-band	4.92	9.93	14.94	4.93	9.94	14.96	4.94	9.96	14.97
Theoretical lower stop-band	5	10	15	5	10	15	5	10	15
(6.13) upper stop-band	-4.57	-4.66	-4.88	-9.97	-9.88	-9.93	-14.64	-14.50	-14.71
(6.16) upper stop-band	-4.93	-4.94	-4.95	-9.94	-9.95	-9.96	-14.95	-14.96	-14.98
Theoretical upper stop-band	-5	-5	-5	-10	-10	-10	-15	-15	-15

To evaluate the accuracy of the TF (6.13) using the new coefficients for any α and β from the range between 0.05 and 1, the mean and maximum absolute dB magnitude errors of (6.13) compared to the target function (6.16) were computed according to the following two relations

$$\text{mean } |\Delta| = \frac{1}{M} \sum_{i=1}^M \left| \left| H_{\alpha+\beta}^{\text{BP-A}}(\omega_i) \right|_{\text{dB}} - \left| H_{\text{targ}}^{\text{BP}}(\omega_i) \right|_{\text{dB}} \right|, \quad (6.19)$$

$$\text{max } |\Delta| = \max_{i=1}^M \left| \left| H_{\alpha+\beta}^{\text{BP-A}}(\omega_i) \right|_{\text{dB}} - \left| H_{\text{targ}}^{\text{BP}}(\omega_i) \right|_{\text{dB}} \right|. \quad (6.20)$$

The mean errors calculated using (6.19) are presented in Fig. 6.10(a) and the maximum errors calculated using (6.20) are presented in Fig. 6.10(b) as surface plots depending on α and β . For these error calculations, a total of $M = 101$ frequency points in the range 0.01 rad/s to 100 rad/s were utilized.

From Fig. 6.10(a), the mean error is less than 1.1 dB for all cases and the maximum error from Fig. 6.10(b) is less than 3 dB, however most combinations of α and β exhibit much smaller error values. Based on these errors, the target function is best approximated by (6.13) when both α and β are simultaneously in the range from approximately 0.4 to 0.6. Small errors are also obtained for approximately equal values of α and β and also for the values $\alpha \approx 1 - \beta$ in the whole range of α and β . The largest errors occur when α is around the middle of its range and β is on the edge of its range and vice-versa.

The identical analysis for the FO TF given by (6.14) can be found in the source paper [53] resulting in similar observations and error values. However, it should be emphasized

that the coefficients found for the FO BP TFs (6.13) and (6.14) are different for each of the functions.

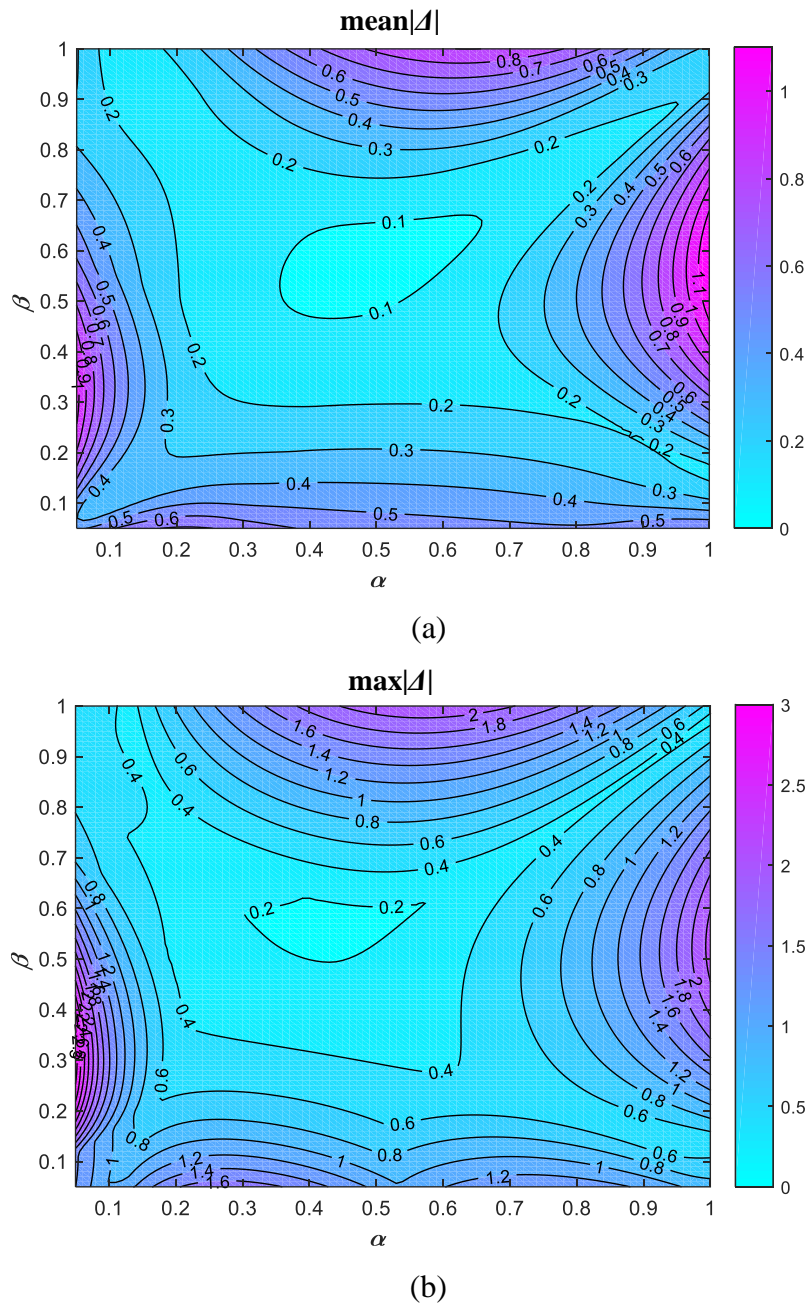


Fig. 6.10 Mean (a) and maximum (b) absolute dB magnitude errors of the function (6.13) with the new coefficients compared to the target function (6.16) depending on α and β

It should be noted that lower errors in magnitudes and slopes could be obtained by a higher degree of interpolation of the numerical values of coefficients, i.e. by a higher degree of matrix equations (6.17) and (6.18). Obviously, the most accurate results can be obtained using the original coefficient values from the numerical optimization, but this requires the reader to code the optimization procedure e.g. in MATLAB. The presentation

of the coefficients as their interpolated functions is aimed at simplifying the process for readers to reproduce the presented results and use for their own filter designs.

6.2.3 Circuit Implementation and Simulation

To verify the previous results, the FO TF given by (6.14) is further experimentally realized in hardware. This TF can be implemented using the Tow-Thomas filter topology when both traditional capacitors are replaced with FOCs as shown in Fig. 6.11 [122]. Note that in the case of implementing the function (6.13) the multi-loop feedback circuit presented in [127] can be employed.

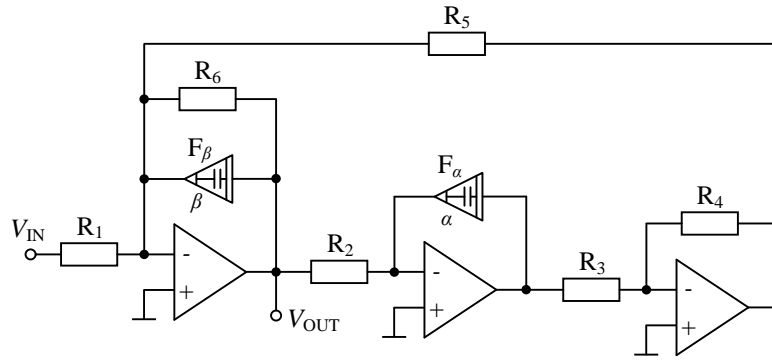


Fig. 6.11 Tow-Thomas FO BP filter topology

However, before this circuit can be validated, the circuit components necessary to realize (6.14) using the computed coefficients need to be determined. Prior to calculating these values, it is necessary to shift the center frequency from 1 rad/s to a required value ω_0 by frequency scaling to the TF (6.14) resulting in

$$H_{\omega_0}^{\text{BP-B}}(s) = \frac{s^\alpha a_{B0} \omega_0^\beta}{b_{B0} \omega_0^{\alpha+\beta} + s^\alpha b_{B1} \omega_0^\beta + s^{\alpha+\beta}}. \quad (6.21)$$

The filter center frequency is chosen $f_0 = \omega_0/(2\pi) = 10$ kHz and the parameters of FOCs $\alpha = 0.8$, $F_\alpha = 62 \text{ nF} \cdot \text{s}^{-0.2}$, $\beta = 0.2$, $F_\beta = 46.9 \text{ } \mu\text{F} \cdot \text{s}^{-0.8}$. Because FO passive elements are not available commercially for physical realizations, these devices need to be approximated. The 5th-order Foster I RC network used for this purpose is described in detail in the source paper [53]. The TF of the Tow-Thomas FO BP filter from Fig. 6.11 in terms of the element parameters obtained by routine circuit analysis is given as

$$H^{\text{T-T}}(s) = \frac{-s^\alpha \frac{1}{F_\beta R_1}}{\frac{R_4}{F_\alpha F_\beta R_2 R_3 R_5} + s^\alpha \frac{1}{F_\beta R_6} + s^{\alpha+\beta}}. \quad (6.22)$$

Based on the specified values of $\alpha = 0.8$ and $\beta = 0.2$, the TF coefficients computed by (6.18) are $a_{B0} = 1.049$, $b_{B0} = 0.9803$, $b_{B1} = 0.1485$. Thus, all the coefficients in (6.21) are

known and the relations for the passive element parameters in the Tow-Thomas filter can be derived by comparing (6.21) and (6.22). Choosing $R_3 = R_4 = 1 \text{ k}\Omega$ and $R_2 = R_5$, these element values are $R_1 = 2\,231 \text{ }\Omega$, $R_6 = 15\,759 \text{ }\Omega$, $R_2 = R_5 = 2\,341 \text{ }\Omega$. The Tow-Thomas filter in Fig. 6.11 was simulated using the calculated component values and LT1361 operational amplifiers by OrCAD PSpice. Additionally, this circuit was designed in hardware and its characteristics were measured. The simulated and experimental magnitude responses are presented in Fig. 6.12 as dotted blue and solid black lines, respectively. The ideal simulation of (6.21) is also presented for comparison as a dashed green line.

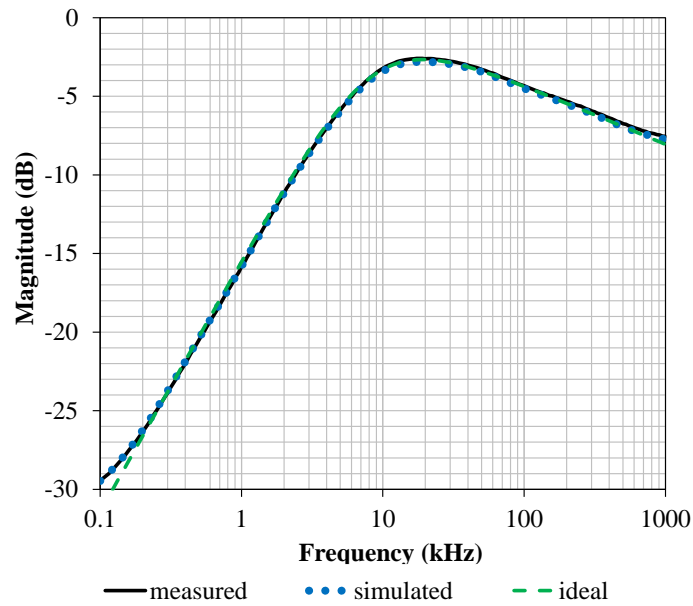


Fig. 6.12 Simulated and measured magnitude frequency characteristics of the Tow-Thomas filter in Fig. 6.11 with $\alpha = 0.8$ and $\beta = 0.2$

From Fig. 6.12 it can be seen that both simulated and measured magnitude responses correspond very well to the ideal response. The deviations at the borders of the displayed frequency band are caused by the limited validity of the FOC emulator.

6.2.4 Concluding Remarks

The simulations and measurements validate that the Tow-Thomas biquad filters do realize the proposed asymmetric FO characteristics using FOCs and the determined TF coefficients. This optimization method can also be extended for other target TFs, for example with a narrower peak in the pass-band around the center frequency, i.e. corresponding to a higher quality factor as described for the FO LP filter case in Section 6.1 and in [52]. Also, examination of the influence of the frequency band utilized for the optimization search can be further investigated, as was previously done with the FO elliptic LP filter in the author's paper [51], to quantify its effects on determined coefficients and filter characteristics.

6.3 $(n + \alpha)$ -Order Transfer Functions

The limitation of most of the works dealing with FO analog filter design is that they are aimed at the order value between one and two only. Partial attention is paid to higher FO TFs in [44], [55], [57], where the product of a TF with fractional order $1 < (1 + \alpha) < 2$ and a TF with integer order $(n - 1)$ is considered to realize $(n + \alpha)$ -order FO filter by cascade approach. The problem is that both partial TFs are chosen as Butterworth and thus the resulting filter is no longer Butterworth with maximally flat magnitude in the pass-band. In a correct cascade synthesis of Butterworth filters the partial blocks differ in their quality factors. In addition, when the partial filters have the same -3 dB cut-off frequency, their cascade shows a decrease of 6 dB at this frequency.

Therefore, the author of this thesis explored TFs with Butterworth maximally flat response and fractional order $(n + \alpha)$ higher than two (i.e. with the integer component $n \geq 2$) in the paper [128], which is also the main source for this section. To better understand the origin of the higher-order FO TF format as defined in the following Subsection 6.3.1, the usual description of $(1 + \alpha)$ FO TF is reminded here again. As described in Subsection 6.1.1 or e.g. in [44], the second-order LP filter circuits can be transformed to the fractional domain by replacing classic IO capacitor by FOE resulting in one of the basic forms of FO LP TFs (6.1) or (6.2). The order of both these TFs is $1 < (1 + \alpha) < 2$ assuming $0 < \alpha < 1$ and the coefficients determine the magnitude and phase frequency response of the filter and can be used to compute the element parameters of the filter circuit. The TFs (6.1) and (6.2) differ in the order (i.e. exponent of s) of the denominator middle term depending on which of the capacitors in the second-order filter structure is replaced by FOE. The coefficients in (6.1) and (6.2) have been numerically found in [44] to approximate the target Butterworth magnitude response with -3 dB cut-off frequency 1 rad/s and the differences between (6.1) and (6.2) have been analyzed to find out which one is most suitable for approximating the target response.

In this section, the theory of FO analog frequency filter TFs and their variant solutions is further extended and performance and accuracy analyses are provided. The main contribution is the mathematical description and analysis of fractional higher-order TF designated for non-cascade circuit implementation, namely inverse follow-the-leader feedback (IFLF) structure [129]. For each $(n + \alpha)$ -order, all possible variants of all-pole FO LP TF are examined to quantify the differences between them and to determine the most suitable $(n + \alpha)$ -order TFs for the approximated Butterworth magnitude responses. The coefficients of these selected TFs are numerically found and expressed in the form of interpolated matrix equations to enable the reader design of FO filter of up to the $(5 + \alpha)$ -order.

6.3.1 Transfer Functions and Coefficient Search

To introduce the $(n + \alpha)$ -order filter TF format, let us start from the $(n + 1)$ -order IFLF LP filter structure presented in Fig. 6.13 [129]. Its all-pole rational TF between the input

IN and output LP OUT is given by (6.23).

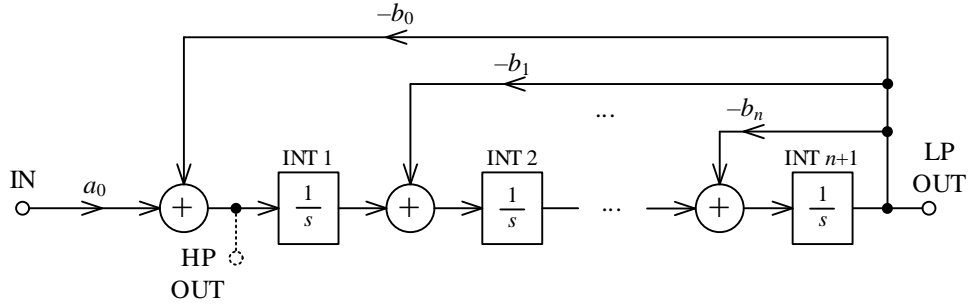


Fig. 6.13 Inverse follow-the-leader feedback (IFLF) structure implementing (6.23)

$$H_{n+1}^{\text{LP}}(s) = \frac{a_0}{\sum_{i=0}^{n+1} b_i s^i}. \quad (6.23)$$

Note that the filter order was intentionally chosen $(n + 1)$ here for a more convenient notation of the order after extending (6.23) to fractional domain. Without loss of generality, it holds $b_{n+1} = 1$ throughout the whole Section 6.3. If the k -th IO integrator in the structure in Fig. 6.13 is interchanged to a fractional one (i.e. with its TF being $1/s^\alpha$) and the other integrators remain unchanged, the TF of the IFLF filter modifies to the FO form

$${}_k H_{n+\alpha}^{\text{LP}}(s) = \frac{a_0}{\sum_{i=0}^{k-1} b_i s^i + \sum_{i=k}^{n+1} b_i s^{i-1+\alpha}}. \quad (6.24)$$

The comparison of (6.23) and (6.24) reveals that the first k terms in denominator (i.e. with $i \in [0, k - 1]$) remained with integer exponent of the Laplace variable s . On the other hand, the terms with higher indexes i , i.e. $i \in [k, n + 1]$ now contain non-integer exponent $(i - 1 + \alpha)$ of s . The number of fractional terms in (6.24) is thus $(n + 2 - k)$. The order of the filter described by TF (6.24) is $(n + \alpha)$, i.e. in the range between two integer numbers n and $(n + 1)$ when considering $0 < \alpha < 1$. As this section deals with the filter order higher than two, it holds $n \geq 2$. Since the value of k indicates the number of the integrator converted to fractional order in Fig. 6.13, the possible range of k is from 1 to $(n + 1)$. The parameter k represents another degree of freedom and extends the variety of TF formats for each filter order $(n + \alpha)$. The suitable choice of k thus must be examined in terms of implementation of the required target frequency response. The described transformation of the IO filter to fractional domain is advantageous, as only one FO integrator based on only one FOE is required for the circuit implementation. Note that the IFLF topology is

chosen here as an example, but also other multiple-feedback state-variable structures can provide the TF (6.24).

The coefficients $a_0, b_0, b_1, \dots, b_n$ (recall that $b_{n+1} = 1$) of the general $(n + \alpha)$ -order TF (6.24) are found using a numerical optimization algorithm to match the target Butterworth LP magnitude response. For each value of the selected filter order $(n + \alpha)$ and possible value of k an individual search run is carried out resulting in a unique vector of the coefficients $(a_0, b_0, b_1, \dots, b_n)$. An optimal k value is found for each considered filter order (combination n and α) providing the lowest approximation error between the magnitude of (6.24) with the found coefficients and the target function. This optimal value of k then determines that the k -th integrator in the filter structure should be chosen as fractional and specifies which of the terms in denominator of the TF (6.24) are with integer and fractional exponent of s . Correspondingly, the process can be applied to other approximation types (such as Bessel, Chebyshev, etc.) as well.

The relation for the magnitude of the Butterworth LP TF generalized to fractional order $(n + \alpha)$ that represents the target response is as follows [58], [60]:

$$\left| B_{n+\alpha}^{\text{LP}}(\omega) \right| = \frac{1}{\sqrt{1 + \omega^{2(n+\alpha)}}}. \quad (6.25)$$

This function provides magnitude of -3 dB at cut-off angular frequency 1 rad/s, unity pass-band gain, and stop-band roll-off $-20(n + \alpha)$ dB/dec typical for FO LP filters. Numerical optimization has been employed to find the coefficients of TF (6.24) such that the maximum absolute error between magnitude in dB of (6.24) and (6.25) is minimized. For this purpose, the MATLAB function *fminsearch* was applied with the argument

$$\max_{i=1}^M \left| 20 \log \left| {}_k H_{n+\alpha}^{\text{LP}}(X, \omega_i) \right| - 20 \log \left| B_{n+\alpha}^{\text{LP}}(\omega_i) \right| \right|. \quad (6.26)$$

Here X is the sought vector of the coefficients $(a_0, b_0, b_1, \dots, b_n)$. Each search used $M = 100$ frequency points logarithmically spaced in the wide frequency range from $\omega_1 = 0.01$ rad/s to $\omega_{100} = 100$ rad/s, covering both pass-band and stop-band of (6.25). For given n and k , the individual runs of *fminsearch* function were performed for the fractional component α decreasing from 0.99 to 0.01 with a linear step of 0.01. The first search was always performed with the highest $\alpha = 0.99$ because in this case the non-integer exponents of s in (6.24) are closest to the integer exponents in (6.23) and the initial estimation of the sought coefficients (required input of *fminsearch* function) can be done on the basis of the well-known coefficients of the Butterworth TF of the integer order $(n + 1)$. The next optimization run (with one step lower α) always uses the values of the coefficients determined in the previous run as initial estimation. Note that also other minimization criteria, such as *LSE* as used e.g. in (6.15), and techniques, e.g. metaheuristic algorithms, can be employed.

6.3.2 Results and Discussion

The first minimization of (6.26) was carried out for $n = 2$, thus for fractional order $(n + \alpha) \in (2, 3)$. All the possible k values (i.e. 1, 2, 3) are considered. To evaluate the performance of this optimization it is appropriate to use again the maximum absolute error in dB defined by (6.26). The resulting values of this error depending on α and k are shown in Fig. 6.14.

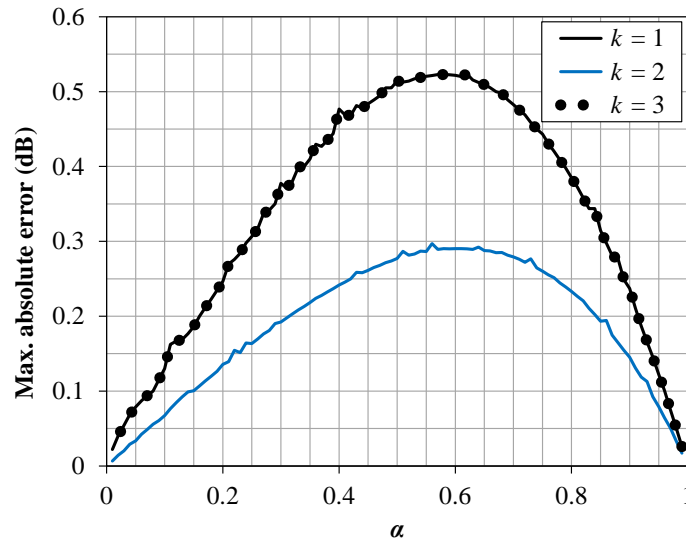


Fig. 6.14 Maximum absolute error between magnitude in dB of (6.24) and (6.25) for $n = 2$

It is apparent that the magnitude of (6.24) approximates the value of the target function (6.25) with the lowest error for $k = 2$ and values of α close to zero and one. The best results reached for the boundary values of α could be expected, as here TF (6.24) tends to integer order. The maximum error occurs for α around 0.6. Interestingly, the errors for $k = 1$ and $k = 3$ are identical. The value $k = 1$ signifies only one IO term in TF (6.24) and the first integrator of fractional order in Fig. 6.13, whereas $k = 3$ denotes only one FO term in (6.24) and the last integrator of fractional order in Fig. 6.13. From this point of view, it is possible to observe a certain symmetry of the results.

Similarly, optimizations were performed for $n = 3$, $n = 4$, and $n = 5$, i.e. for filter orders $(n + \alpha) \in (3, 4)$, $(n + \alpha) \in (4, 5)$, and $(n + \alpha) \in (5, 6)$, respectively, and always with assuming all possible values of k , i.e. $k \in [1, n + 1]$. The reached maximum absolute errors computed by (6.26) are depicted in Figs. 6.15 to 6.17. Also, for n values from 3 to 5, the largest approximation errors occur for the boundary (highest and lowest considered) k values. The error is lowest for middle values of k , i.e. $k = 2$ and $k = 3$ for $n = 3$, and $k = 3$ for $n = 4$. Up to $n = 4$, the error values show the symmetry with respect to the selected value of k observed already for the case $n = 2$. From the last Fig. 6.17 with $n = 5$ it is seen that it is no more possible to unambiguously determine for which value of k from 2 to 5 the error of approximation reaches the lowest value, as the dependences on α are similar

for all error curves. Regardless of n , the boundary values of α provide lower error, whereas the highest error is obtained slightly above the middle of the range of α . The achieved absolute error values are almost always below 0.5 dB and for selected optimal values of k they stay below 0.3 dB in the whole range of α , which is a reasonable value.

The findings can be generalized that it is appropriate to choose k value as follows:

$$k = \begin{cases} n/2 + 1, & \text{when } n \text{ is even} \\ (n+1)/2 \text{ or } (n+3)/2, & \text{when } n \text{ is odd.} \end{cases} \quad (6.27)$$

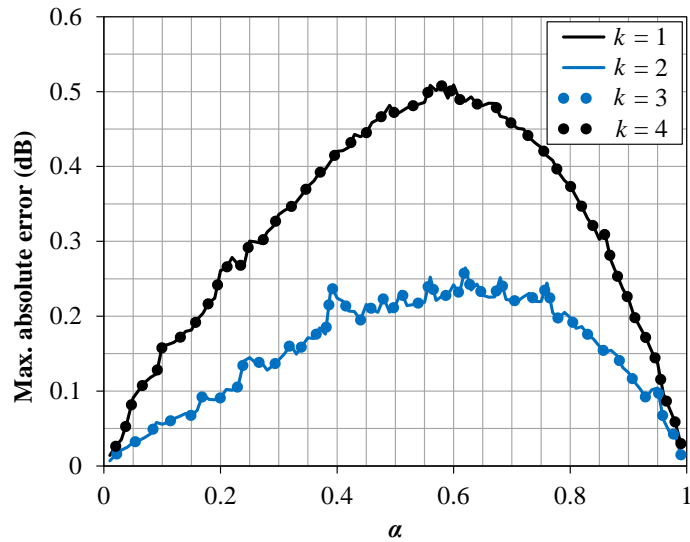


Fig. 6.15 Maximum absolute error between magnitude in dB of (6.24) and (6.25) for $n = 3$

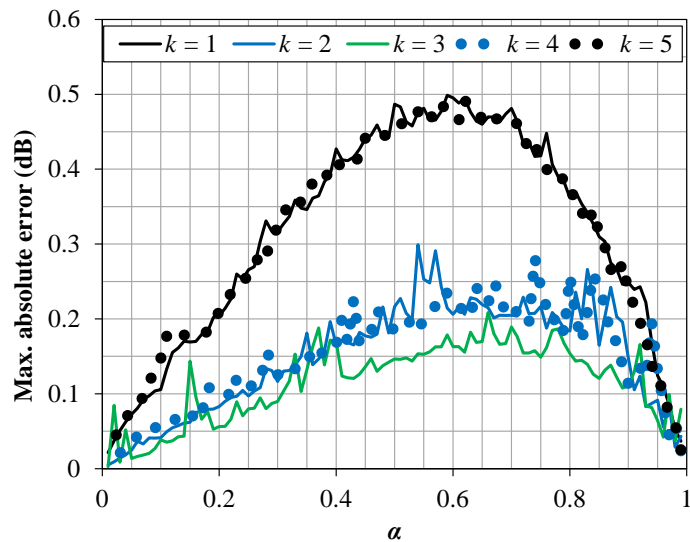


Fig. 6.16 Maximum absolute error between magnitude in dB of (6.24) and (6.25) for $n = 4$

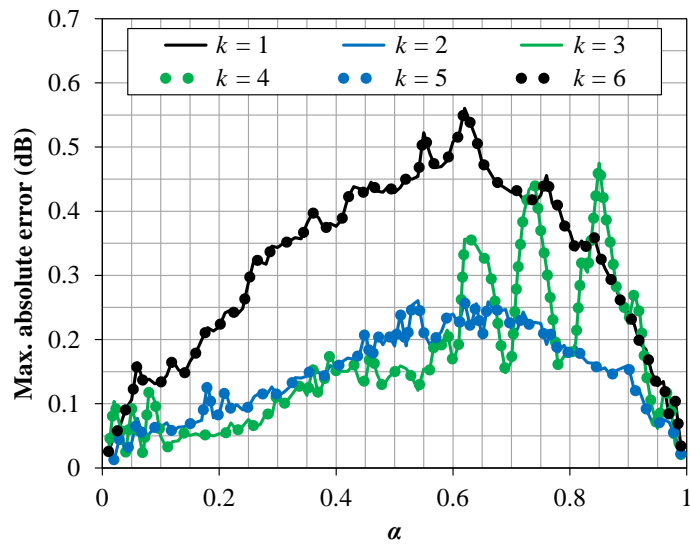


Fig. 6.17 Maximum absolute error between magnitude in dB of (6.24) and (6.25) for $n = 5$

This optimization therefore helps to find the appropriate distribution of IO and FO terms in TF (6.24) and also location of FO integrator in the implementing structure, e.g. in Fig. 6.13.

The coefficients resulted from the numerical optimization for the TF (6.24) with $n = 2$ and $k = 2$ depending on α are graphically presented by solid lines in Fig. 6.18.

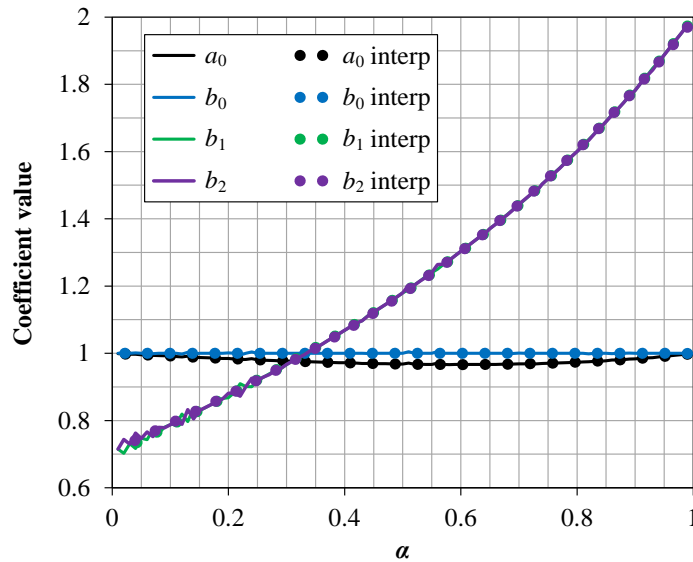


Fig. 6.18 Coefficients of TF (6.24) with $n = 2$ and $k = 2$ found by *fminsearch* function (solid lines) and interpolated by (6.28) (dotted lines)

The coefficients b_1 and b_2 are almost identical, thus their curves (green and violet) overlap. For $\alpha = 0.99$ the values are close to the coefficients of the third-order Butterworth TF which, as already mentioned, have been used as initial estimation of the *fminsearch* function. When decreasing α , the coefficients change continuously and for $\alpha = 0.01$ they

approach the coefficients of the second-order Butterworth TF providing that the sum of b_1 and b_2 corresponds to the coefficient of the first power of s in denominator, i.e. 1.414.

The following interpolated equations as functions of α have been derived for computing the coefficients $a_0, b_0, b_1, \dots, b_n$. Only one value of k providing the best approximation result is selected for each of the values $n = 2, 3, 4$, and 5. The coefficient values computed by (6.28) are also displayed in Fig. 6.18 by dotted lines to demonstrate the accuracy of interpolation.

- $n = 2, k = 2$

$$\begin{pmatrix} a_0 \\ b_0 \\ b_1 \\ b_2 \end{pmatrix} = \begin{pmatrix} 0.9992 & -0.0720 & -0.0347 & 0.1063 \\ 0.9999 & 0.0005 & 0.0010 & -0.0017 \\ 0.6967 & 0.8991 & -0.1453 & 0.5452 \\ 0.7091 & 0.8101 & 0.0337 & 0.4388 \end{pmatrix} \begin{pmatrix} 1 \\ \alpha \\ \alpha^2 \\ \alpha^3 \end{pmatrix}. \quad (6.28)$$

- $n = 3, k = 2$

$$\begin{pmatrix} a_0 \\ b_0 \\ b_1 \\ b_2 \\ b_3 \end{pmatrix} = \begin{pmatrix} 0.9974 & 0.0421 & 0.0623 & -0.1003 \\ 0.9984 & 0.0973 & 0.1077 & -0.2003 \\ 1.0418 & 1.7942 & -1.0600 & 0.8673 \\ 0.9625 & 0.5066 & 2.8741 & -0.9453 \\ 1.9850 & 1.2112 & 0.0066 & -0.5818 \end{pmatrix} \begin{pmatrix} 1 \\ \alpha \\ \alpha^2 \\ \alpha^3 \end{pmatrix}. \quad (6.29)$$

- $n = 4, k = 3$

$$\begin{pmatrix} a_0 \\ b_0 \\ b_1 \\ b_2 \\ b_3 \\ b_4 \end{pmatrix} = \begin{pmatrix} 0.9958 & 0.0536 & -0.0019 & -0.0487 \\ 0.9917 & 0.1046 & -0.2383 & 0.1461 \\ 2.6217 & 0.9962 & 0.4211 & -0.7971 \\ 1.5721 & 3.1363 & -0.7767 & 1.3395 \\ 1.8296 & 1.1265 & 3.0882 & -0.8161 \\ 2.5946 & 1.2991 & -0.2245 & -0.4183 \end{pmatrix} \begin{pmatrix} 1 \\ \alpha \\ \alpha^2 \\ \alpha^3 \end{pmatrix}. \quad (6.30)$$

- $n = 5, k = 2$

$$\begin{pmatrix} a_0 \\ b_0 \\ b_1 \\ b_2 \\ b_3 \\ b_4 \\ b_5 \end{pmatrix} = \begin{pmatrix} 0.9932 & 0.0931 & -0.1625 & 0.0726 \\ 0.9982 & 0.1058 & -0.0286 & -0.0792 \\ 1.6469 & 3.6925 & -4.2764 & 2.8262 \\ 1.5940 & 0.2503 & 7.0473 & -1.5161 \\ 5.1582 & 5.7095 & -0.7549 & -1.0162 \\ 5.2433 & 1.5986 & -0.0957 & 0.6862 \\ 3.2145 & 1.1127 & -0.1779 & -0.3084 \end{pmatrix} \begin{pmatrix} 1 \\ \alpha \\ \alpha^2 \\ \alpha^3 \end{pmatrix}. \quad (6.31)$$

It is very important to verify the stability of the TF (6.24). It has been examined in the source paper [128] and the filters described by the TF (6.24) with the coefficients determined by (6.28) to (6.31) and the respective values of n and k are found to be always stable.

6.3.3 Extension to High-Pass Filters

Applying the transformation $s \rightarrow 1/s$, the FO LP TF (6.24) can be transformed to FO HP TF given by the relation

$${}_k H_{n+\alpha}^{\text{HP}}(s) = \frac{a_0 s^{n+\alpha}}{\sum_{i=0}^{k-1} b_i s^{n+\alpha-i} + \sum_{i=k}^{n+1} b_i s^{n+1-i}}. \quad (6.32)$$

Compared to the TF (6.24), there are k fractional terms in the denominator of (6.32) and the term in numerator is also fractional. The order of the coefficients b in the denominator is reversed (b_0 is in the term with highest exponent of s). This HP TF can be realized by the IFLF structure in Fig. 6.13, where the output of the filter is at the output of the first summation block (labeled HP OUT) and $(n + 2 - k)$ -th integrator is fractional. The coefficients a and b determined for LP TF (6.24) can be used in HP TF (6.32) too and therefore no extra numerical search for HP coefficients is required. It is also not necessary to determine for which value of k the smallest deviation of the TF (6.32) from HP Butterworth response is achieved as it is the same as for LP FO TF.

6.3.4 Circuit Implementation and Simulation

As an example, an IFLF filter design with order 2.25 and parameters $n = 2$, $\alpha = 0.25$, $k = 2$ will be given. The coefficients of TF (6.24) were found for cut-off angular frequency 1 rad/s. This frequency will be shifted to a more practical value $\omega_0 = 10$ krad/s, i.e. $f_0 = 1592$ Hz, using the frequency scaling demonstrated by the following relation

$${}_2 H_{2.25}^{\text{LP}}(s) = \frac{a_0}{b_0 + \frac{b_1}{\omega_0} s + \frac{b_2}{\omega_0^{1.25}} s^{1.25} + \frac{1}{\omega_0^{2.25}} s^{2.25}} = \frac{a_0 \omega_0^{2.25}}{b_0 \omega_0^{2.25} + b_1 \omega_0^{1.25} s + b_2 \omega_0 s^{1.25} + s^{2.25}}. \quad (6.33)$$

After substitution of the coefficients computed by (6.28) and the selected ω_0 value into (6.33) we get

$${}_2 H_{2.25}^{\text{LP}}(s) = \frac{9.8032 \cdot 10^8}{1 \cdot 10^9 + 9.1933 \cdot 10^4 s + 9.1926 \cdot 10^3 s^{1.25} + s^{2.25}}. \quad (6.34)$$

This TF is realized by the multiple-feedback filter shown in Fig. 6.19 containing three OTAs, two resistors, two standard capacitors, and one FOC with fractance F_2 and order $\alpha = 0.25$. The LT1228 amplifier [130] was used as OTA in the OrCAD PSpice simulations presented here.

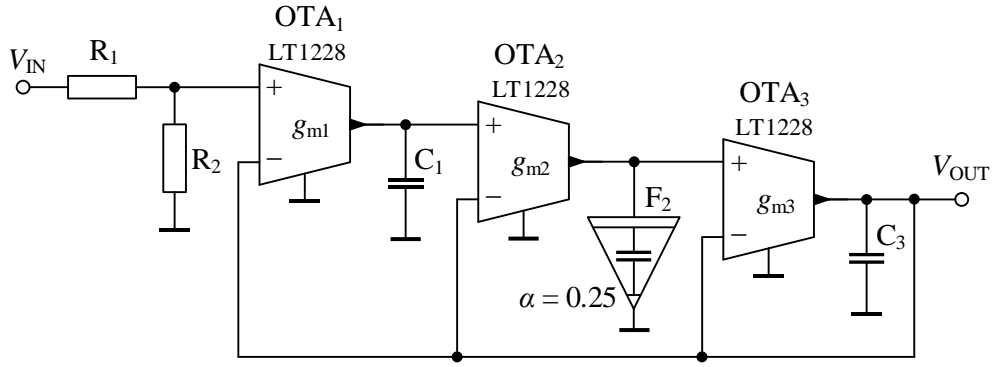


Fig. 6.19 OTA-based 2.25-order LP filter

The TF of the structure in Fig. 6.19 in terms of element parameters is

$${}_2H_{2.25}(s) = \frac{\frac{R_2}{R_1 + R_2} \frac{g_{m1} g_{m2} g_{m3}}{C_1 F_2 C_3}}{\frac{g_{m1} g_{m2} g_{m3}}{C_1 F_2 C_3} + \frac{g_{m2} g_{m3}}{F_2 C_3} s + \frac{g_{m3}}{C_3} s^{1.25} + s^{2.25}}. \quad (6.35)$$

Choosing $C_1 = C_3 = 47$ nF and $F_2 = 63.162 \mu\text{F} \cdot \text{s}^{-0.75}$, by comparing the coefficients in denominators of (6.34) and (6.35) we get the transconductances $g_{m1} = 0.5112$ mS, $g_{m2} = 0.6317$ mS, and $g_{m3} = 0.4321$ mS. The DC gain $a_0/b_0 = 0.98032$ is ensured by simple resistive divider $R_1 = 240 \Omega$, $R_2 = 12$ k Ω at the filter input.

Due to the commercial unavailability of FOC, this element was emulated by 7th-order Valsa ladder RC network as described in detail in the source paper [128]. The emulator operates correctly in the frequency band 80 Hz to 1 MHz (more than 4 decades) providing the admittance phase angle $90^\circ \cdot \alpha = 22.5^\circ$ with maximum deviation $\pm 1^\circ$.

The PSpice simulated magnitude frequency characteristic of the filter from Fig. 6.19 with LT1228 OTAs and emulated FOE is depicted in Fig. 6.20 as dotted black line. The target characteristic computed by (6.25) and shifted to the cut-off frequency $f_0 = 1$ 592 Hz is represented by black solid line. The optimized magnitude characteristic given by (6.34) is displayed by dashed black line. The blue and green lines have been added to illustrate the position of the FO characteristics between the 2nd and 3rd filter order.

Both the optimized and simulated characteristics of the filter are in a very good agreement with the target function. As these characteristics overlap, the magnitude errors of the optimized function and of the simulated characteristic against the target function are shown in Fig. 6.21 by the dashed and dotted lines, respectively. The error of the optimized characteristic (6.34) with the found coefficients vs. the target function is ± 0.17 dB which confirms also the result in Fig. 6.14 (blue line at $\alpha = 0.25$). The error of the simulated characteristic follows the error of the optimized characteristic up to 1 kHz

and at higher frequency it turns to negative values, however it does not exceed -0.72 dB in the displayed band.

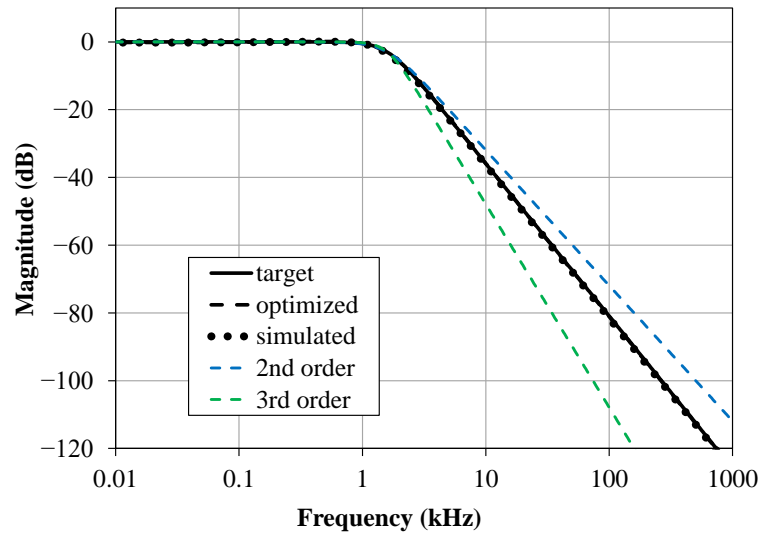


Fig. 6.20 Target acc. to (6.25) (solid black), optimized acc. to (6.34) (dashed black), and simulated (dotted black) magnitude characteristics of the Butterworth LP filter of the order 2.25

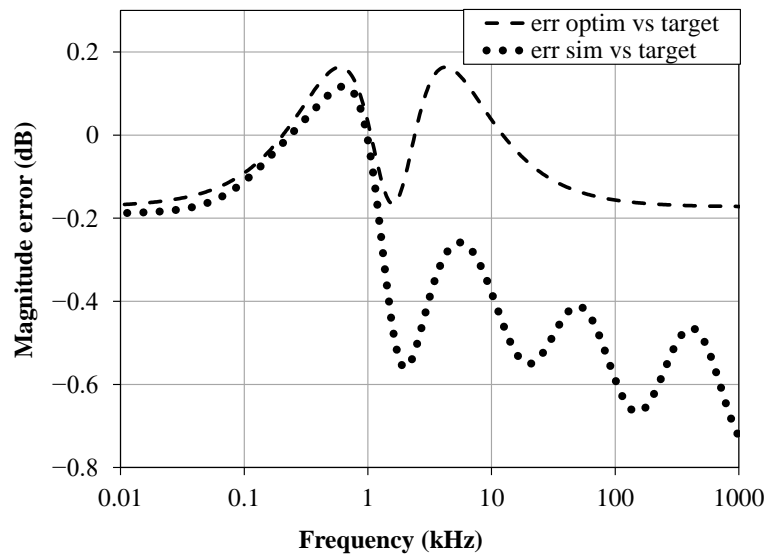


Fig. 6.21 Magnitude errors of optimized (6.34) (dashed), and simulated (dotted) characteristics from Fig. 6.20 vs. target function (6.25)

The phase characteristics of the optimized function (6.34) and of the simulated filter from Fig. 6.19 are shown in Fig. 6.22 by dashed and dotted lines, respectively. Target phase is not present in Fig. 6.22 as only magnitude part is defined by the target function (6.25). Target phase response in a form of mathematical relation cannot be defined in this case. Thus only the asymptotic phase values 0° and $-90^\circ \cdot 2.25 = -202.5^\circ$, which the phase

theoretically approaches at the edges of the frequency band, are indicated by the red arrows in Fig. 6.22. Both of the black phase characteristics in the figure are close to each other and approach the expected asymptotic values at low and high frequencies. The phase characteristics of the 2nd and 3rd order Butterworth filter have been also added for illustration.

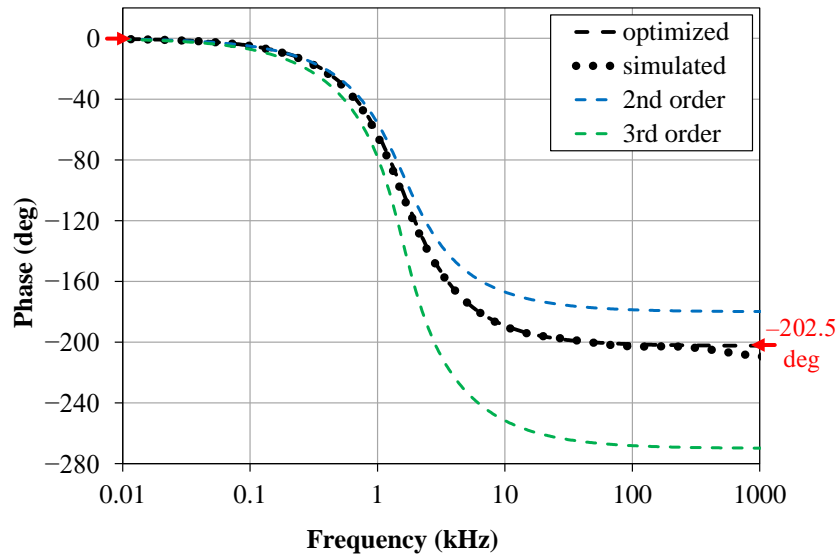


Fig. 6.22 Optimized acc. to (6.34) (dashed), and simulated (dotted) phase characteristics of the Butterworth LP filter of the order 2.25

6.3.5 Concluding Remarks

New formats of all-pole LP filter TFs of the fractional order higher than two suitable for non-cascade circuit implementations, e.g. by state-variable structures with integrators and multiple feedbacks, have been introduced. The LP TFs of the fractional order from 2 to 6 have been examined regarding the accuracy of the approximation of the Butterworth target function. Their slope of magnitude frequency response in stop-band is continuously adjustable between -40 dB/dec and -120 dB/dec and not limited to multiples of 20 dB/dec only which is an important difference compared to IO filters. All the FO LP TF formats considered (depending on the selected values of n and k) show good agreement with the target function, while the maximum absolute error is mostly below 0.5 dB. The error can be reduced even below 0.3 dB with the optimal choice of the value of k , i.e. the position of the FO integrator in the filter structure. It was found that the FO integrator should be located in the middle of the structure and for higher filter orders it should not at least occur at its edge to reach the lowest error of approximation of the magnitude target function. For these most suitable values of k and fractional orders from 2 to 6 the relations for computing the FO LP TF coefficients are presented.

The resulting FO filter structure differs from the conventional IO one only in replacing one standard capacitor with FOC. With the expected availability of FOC

implementations, it will be possible to easily design FO filters without increasing the circuit complexity compared to conventional IO filters. The structures with integrators and multiple feedbacks are practically well-proven and employ commonly available active elements.

FO HP filters can be easily obtained from the proposed FO LP filters by the well-known $s \rightarrow 1/s$ transformation. The described methodology can also be used to design FO filters based on other target functions (e.g. Chebyshev, Cauer, Bessel), but for this purpose it is necessary for the designer to program own optimization routine for finding the TF coefficients and possibly use a modified filter structure with feedforwards in case the TF contains transfer zeros.

6.4 Other Author's Works on FO Filters

This section briefly introduces the works of the author of this thesis concerning FO filters, which are of less importance and for spatial reasons it is not possible to deal with them in more detail. Subsection 6.4.1 deals with earlier articles by the author of this thesis, where the FO TFs of other authors were used (e.g. [44]) and their main contribution is the verification and optimization of the possible circuit implementation of FO filters and various analyzes of their parameters and behavior, which distinguish them from IO filters. Subsection 6.4.2 deals with finding the FO TF coefficients for elliptic filters using a similar approach to Sections 6.1 - 6.3, i.e. obtaining the true FO filter TF and their coefficients based on error minimization against the elliptic (Cauer) target function. The next Subsection 6.4.3 deals with IO TFs of higher order approximating different kinds of FO filters.

6.4.1 Implementations and Analyses of FO Filters

The author's paper [127] describes FO multifunction filter with two DVCCs, four grounded passive elements, one of which is FOC. The filter provides LP and BP TF simultaneously and its order can be set between one and two. The TF coefficients are set according to the rules in [44] and the filter provides maximally flat Butterworth response. Procedure of obtaining suitable parameters of passive elements is demonstrated in detail in order to give practical instruction, for example how to properly utilize the dynamical range of conveyors, or to tune the cut-off frequency. PSpice simulations confirm the theoretical expectations, show very good performance with AD844 amplifier [101] as conveyor replacement, and discover the most critical parasitic properties of conveyors.

FO LP filter design based on a multiple-feedback filter with a single operational amplifier is presented in the author's paper [131]. One of the capacitors is replaced in the original IO filter by FOC. The analytical description of the circuit is given and procedure of element computation for a Butterworth-like approximation is stated again according to the rules in [44]. The manufactured sample of FOC based on resistive-capacitive layers

with distributed parameters as described in Chapter 3 is employed in the filter. Simulation and measurement results are provided to verify the functionality of the design.

In the paper [132] author analyses the influence of FOE properties on characteristics of frequency filter where the element is employed. Tow-Thomas topology with one capacitor replaced by FOC is examined. This element is emulated by fifth-order Foster I RC network which has limited validity of FO impedance properties resulting in distortion of the filter characteristics. Shifting the frequency band of FOE emulation is tested and recommendations regarding the correct filter functionality are provided.

At this point, it is also worth mentioning the chapter in the book [133], which summarizes the scientific findings of the author and his team in the field of FO filters achieved by the year 2018. These results are also parts of the Sections 6.1 and 6.4.2.

6.4.2 FO Filters with Elliptic Responses

This subsection is based on the author's publications [51] and [134] where FO TFs to approximate the pass-band and stop-band ripple characteristics of a second-order elliptic (Cauer) LP filter are designed and validated. The coefficients for these TFs are determined through the application of a least squares fitting process. These fittings are applied to symmetrical and asymmetrical frequency ranges to evaluate how the selected approximated frequency band impacts the determined coefficients using this process and the TF magnitude characteristics.

MATLAB simulations of $(1 + \alpha)$ order LP magnitude responses are given as examples with fractional steps from $\alpha = 0.1$ to $\alpha = 0.9$ and compared to the second-order elliptic response. Further, MATLAB simulations of the order $(1 + \alpha) = 1.25$ and 1.75 using all sets of coefficients are given as examples to highlight their differences. The FO elliptic filter responses were validated using both SPICE simulations and experimental results using two operational amplifier-based topologies realized with emulated FOCs for $(1 + \alpha) = 1.2$ and 1.8 order filters.

6.4.3 FO Filters Approximated by IO Rational Transfer Functions

The author also dealt with the second basic approach of the design of FO filters, which is the approximation of the FO TF using IO rational function of higher order. As mentioned in the Section 2.2, the approach can be based on the following two techniques. The earlier of the techniques uses an intermediate step, where FO TF is first obtained using minimization of error versus a target function (similarly to Sections 6.1 – 6.3). Then the terms in the FO TF containing non-integer powers of s are approximated by IO rational function. This TF is then implemented by a known structure of IO filter. This technique is used in articles [121], [135] – [140].

The paper [135] presents design and implementation of FO filters based on promising CMOS structure of low-voltage differential difference current conveyor (DDCC) designed and fabricated using the $0.35 \mu\text{m}$ CMOS AMIS process. In the papers [136] and

[137], FO LP and HP filters with universal voltage conveyors (UVC) derived by the continued fraction expansion are presented.

The paper [138] deals with FO LP filter with electronically adjustable pole frequency and fractional order between 1 and 2. It is based on third-order follow-the-leader feedback (FLF) topology with OTAs and adjustable current amplifiers.

Another FLF-based electronically reconfigurable FO filter, that is able to be configured as LP and HP filter, is introduced in [139]. It offers independent electronic control of the order between 1 and 2, pole frequency, and particular type of approximation.

In the paper [140], six current conveyor-based multiple-feedback current-mode circuits approximating the FO LP filter response are proposed. A method of reducing number of circuit elements is demonstrated.

Novel topologies of capacitorless FO filters, implemented using the internal gate-source capacitance of metal oxide semiconductor (MOS) transistors, are introduced in [121]. The filters offer digital programmability in terms of selecting one of four standard filter functions and the capability for electronic tuning of frequency characteristics.

The second technique of IO emulation of a FO filter, used in more recent works, is a direct approximation of a target function using IO rational function. This method is applied in the author's articles [141] – [144].

In the paper [141], a new two-steps design strategy is introduced for the optimal rational approximation of FO Butterworth filter. At first, the weighting factors of the summation between n - and $(n + 1)$ -order Butterworth filters are optimally determined. This model is then employed as initial point for another optimization, which minimizes the magnitude error relative to the $(n + \alpha)$ -order Butterworth response.

Generalization of IO transitional Butterworth-Butterworth filter to the FO domain is presented in [142]. Rational approximants of this FO transitional filter are optimally realized and several design examples demonstrate the correctness of the design.

The article [143] presents the optimal modeling of power-law filters with the LP, HP, BP, and band-stop (BS) responses and their inverse counterparts by means of IO rational approximants. The performances of the approximants exhibiting the fractional-step magnitude and phase responses are evaluated using various statistical indices. At the cost of higher computational complexity, the proposed approach achieved improved accuracy with guaranteed stability when compared to similar published solutions.

This topic is further developed in [144] by a further generalization of FO filters whose limiting form is that of the second-order filter. This new filter class can also be regarded as a superset of the recently reported power-law filters [143]. The inverse FO filter variants can also be achieved using the suggested method.

7. FO OSCILLATORS

As already mentioned in Section 2.3, FO oscillators provide some more general properties compared to classic IO oscillators thanks to their non-integer order. Their order affects both the oscillating condition and the oscillating frequency. If these FO oscillators are designed to be multi-output, the fractional order can allow setting the relative phase shift of the output signals by non-integer multiples of 90 degrees. The fractional order thus represents another adjustable parameter of the oscillator and provides another degree of freedom, but the relations for describing the oscillator's operation become more complex compared to the integer order. The consequence is, for example, the impossibility of independent setting of the oscillation condition and the oscillation frequency. However, the possibility of setting very high oscillation frequencies for FO oscillators when using common component values can be an advantage. For IO oscillators, very low values of capacitances, which would be comparable to parasitic capacitances, would have to be used.

The author of this thesis published the papers [70], [145], and [146] dealing with FO oscillators. The following Section 7.1 is based on the article [70] which provides a detailed description of practical FO oscillator design and verification.

7.1 FO Oscillator Design and Evaluation

The basic circuit selected for the FO oscillator design is shown in Fig. 7.1. Two DVCCs were employed as active elements and two grounded FO admittances (Y_α , Y_β) are connected to Z terminals of the conveyors. The characteristic equation of the circuit is

$$Y_\alpha Y_\beta R_1 R_2 - Y_\beta R_2 + 1 = 0. \quad (7.1)$$

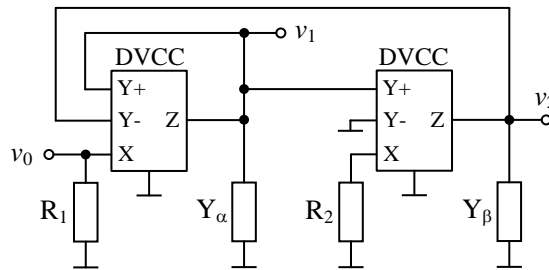


Fig. 7.1 Oscillator with current conveyors and FO admittances

Assuming that $|Y_{\alpha 0}|$ and $|Y_{\beta 0}|$ are the magnitudes of the admittances Y_α and Y_β at the oscillation angular frequency ω_0 , the formulas for these admittances can be expressed as $Y_\alpha = |Y_{\alpha 0}|j^\alpha$ and $Y_\beta = |Y_{\beta 0}|j^\beta$. After substituting these relations into (7.1), rearranging terms

in order to separate real and imaginary parts and equating them to zero, we can derive the following relations

$$R_1 = \frac{\sin\left(\frac{\pi}{2}\beta\right)}{|Y_{\alpha 0}|\sin\left[\frac{\pi}{2}(\alpha + \beta)\right]}, \quad (7.2)$$

$$R_2 = \frac{\sin\left[\frac{\pi}{2}(\alpha + \beta)\right]}{|Y_{\beta 0}|\sin\left(\frac{\pi}{2}\alpha\right)}. \quad (7.3)$$

The expressions in (7.2) and (7.3) are used for computing the values of the resistances R_1 and R_2 in order the circuit to oscillate at the frequency ω_0 . In other words, the values described by (7.2) and (7.3) fulfill the condition of oscillation. No relation for oscillation frequency is presented here, as in fact it does not exist. The oscillation frequency is simply ω_0 , i.e. the value of frequency where the fractional admittances used in the oscillator have their magnitudes $|Y_{\alpha 0}|$ and $|Y_{\beta 0}|$. Unfortunately, the oscillation frequency and condition cannot be set independently, but this problem seems to be common to this class of FO oscillators.

To tune the oscillation frequency to a new value ω_0' the following formulas can be used

$$\frac{\omega_0'}{\omega_0} = \left\{ \frac{\sin\left(\frac{\pi}{2}\beta'\right)}{|Y_{\alpha 0}|R_1'\sin\left[\frac{\pi}{2}(\alpha' + \beta')\right]} \right\}^{\frac{1}{\alpha'}} = \left\{ \frac{\sin\left[\frac{\pi}{2}(\alpha' + \beta')\right]}{|Y_{\beta 0}|R_2'\sin\left(\frac{\pi}{2}\alpha'\right)} \right\}^{\frac{1}{\beta'}}. \quad (7.4)$$

Here $|Y_{\alpha 0}|$ and $|Y_{\beta 0}|$ are still the admittance magnitudes at the original oscillation frequency ω_0 and the single quotes at R_1 , R_2 , α , and β mean that their values are going to be modified in order to tune, i.e. these are the new values of the element parameters. The whole relation (7.4) must be valid to keep the circuit at the oscillation boundary, i.e. it represents the oscillation condition. Obtaining the relation (7.4) is similar to deriving (7.2) and (7.3) from the characteristic equation (7.1) with the difference in the substitution of FO admittances by the relations $Y_\alpha = |Y_{\alpha 0}|(j\omega_0')^{\alpha'} / \omega_0^{\alpha'}$ and $Y_\beta = |Y_{\beta 0}|(j\omega_0')^{\beta'} / \omega_0^{\beta'}$.

It is apparent that the oscillation frequency and condition are influenced not only by resistances and magnitudes of admittances as in the case of classic oscillators but also by the admittance orders α and β . This increases the degree of freedom and brings other interesting properties that will be shown below.

Three voltage outputs (v_0 , v_1 , and v_2) are available as indicated in Fig. 7.1. Their voltages are related in the following way

$$v_0 = v_1 |Y_{\alpha 0}| R_1 e^{j\frac{\pi}{2}\alpha}, \quad (7.5)$$

$$v_2 = \frac{v_1}{|Y_{\beta 0}| R_2} e^{-j\frac{\pi}{2}\beta}. \quad (7.6)$$

It is seen that the phase shift between v_0 and v_1 is $\alpha\pi/2$, between v_2 and v_1 is $-\beta\pi/2$, and between v_0 and v_2 is $(\alpha + \beta)\pi/2$. The phase difference between the output voltages can be set continuously depending on the parameters α and β . This property is unique and is not available at IO oscillators.

It is also interesting to determine sensitivities of the normalized oscillation frequency (ω_0'/ω_0) to the passive element parameters:

$$S_{|Y_{\alpha 0}|}^{\omega_0'/\omega_0} = S_{R_1}^{\omega_0'/\omega_0} = -\frac{1}{\alpha}, \quad (7.7)$$

$$S_{|Y_{\beta 0}|}^{\omega_0'/\omega_0} = S_{R_2}^{\omega_0'/\omega_0} = -\frac{1}{\beta}. \quad (7.8)$$

The sensitivities increase in their absolute values with decreasing coefficients α and β . The oscillation frequency can be controlled by setting α and β as seen in (7.4), but one must consider that especially for low values of α and β the oscillation frequency could be very sensitive to tolerances of passive element parameters.

7.1.1 Oscillation Frequency Tuning

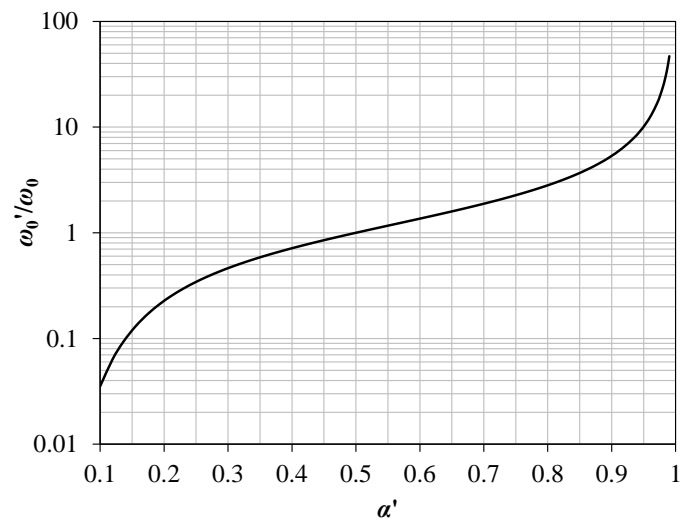
Equation (7.4) suggests the possibilities of tuning the oscillation frequency. The first option is to modify the order (α' and β') of the admittances which requires a controllable FOE. The second tuning possibility is varying the resistances R_1 and R_2 . Both these tuning options are analyzed below.

i) Tuning through the order of FOEs

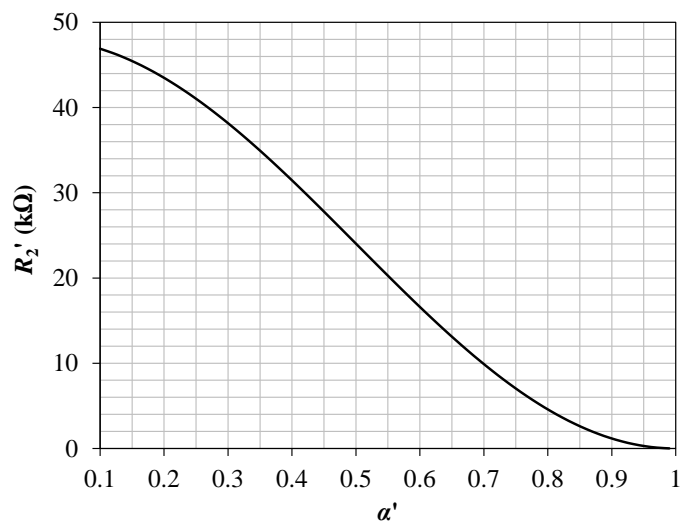
Let us aim at the tuning by the orders α' and β' . To simplify the analysis, both these values will be considered equal ($\alpha' = \beta'$) and thus (7.4) is transformed to

$$\frac{\omega_0'}{\omega_0} = \left[\frac{1}{|Y_{\alpha 0}| 2R_1' \cos\left(\frac{\pi}{2}\alpha'\right)} \right]^{\frac{1}{\alpha'}} = \left[\frac{2 \cos\left(\frac{\pi}{2}\alpha'\right)}{|Y_{\beta 0}| R_2'} \right]^{\frac{1}{\alpha'}} = \left(\frac{1}{|Y_{\alpha 0}| |Y_{\beta 0}| R_1' R_2'} \right)^{\frac{1}{2\alpha'}}. \quad (7.9)$$

Let us choose the initial magnitudes of FO admittances $|Y_{\alpha 0}| = |Y_{\beta 0}| = 1/17\,000\text{ S}$ and the orders $\alpha = \beta = 0.5$. As already mentioned, if the admittances Y_α and Y_β had these properties at a chosen frequency ω_0 and the resistances R_1 and R_2 are computed by (7.2) and (7.3), ω_0 would be the oscillation frequency. The calculated resistance values are $R_1 = 12\,021\ \Omega$, $R_2 = 24\,042\ \Omega$. The effect of increasing or decreasing the value of α' compared to the initial value of 0.5 on the normalized oscillation frequency is presented in Fig. 7.2(a). It should be noted that the resistance R_1 remained constant during this tuning ($R_1 = R_1' = 12\,021\ \Omega$) and R_2 was computed as a new value R_2' by $R_2' = 4R_1'\cos^2(\pi\alpha'/2)$ in order to keep the whole relation (7.9) valid and thus to meet the oscillation condition. The computed values of R_2' vs α' are depicted in Fig. 7.2(b).



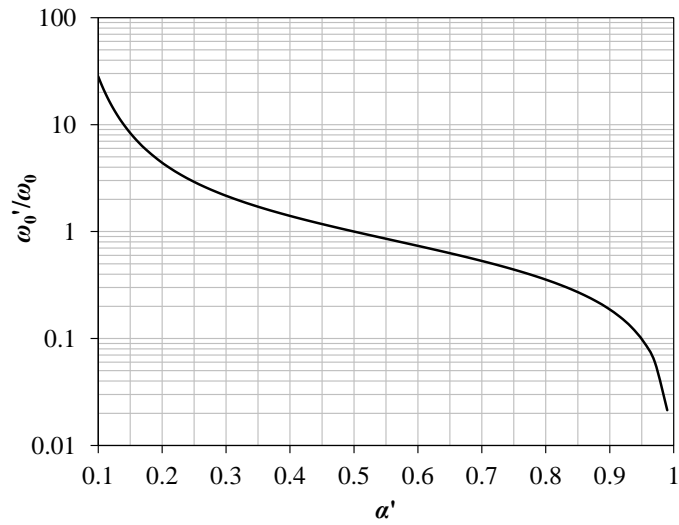
(a)



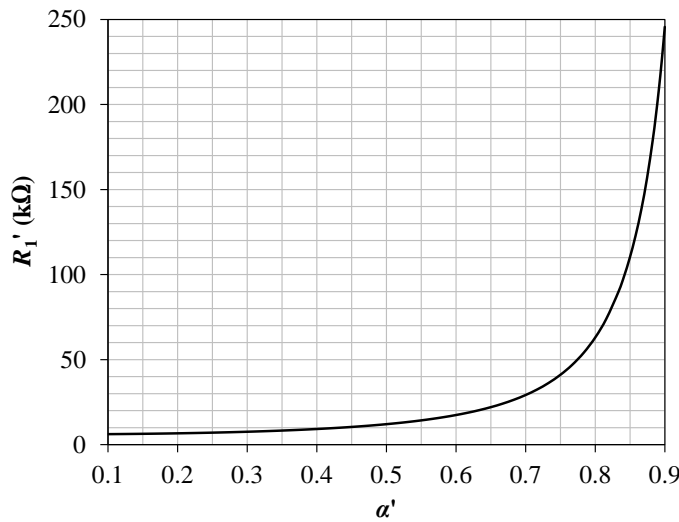
(b)

Fig. 7.2 (a) Tuning of normalized oscillation frequency (ω_0'/ω_0) by changing the order of both FOEs ($R_1 = \text{const.}$), and (b) computed values of R_2' as a function of the order

Another possibility is to set R_2 constant ($R_2 = R_2' = 24\,042\ \Omega$) and to compute R_1' . This variant is presented in Fig. 7.3.



(a)



(b)

Fig. 7.3 (a) Tuning of normalized oscillation frequency (ω_0'/ω_0) by changing the order of both FOEs ($R_2 = \text{const.}$), and (b) computed values of R_1' as a function of the order

The curve of the normalized oscillation frequency in Fig. 7.3(a) has inverse slope compared to the one in Fig. 7.2(a), i.e. the frequency decreases with increasing α' . Fig. 7.3(b) shows that the range of the computed resistance R_1' is high and R_1' increases dramatically at values of α' close to one.

ii) Tuning through the resistances R_1 and R_2

Another possibility of setting the oscillation frequency resulting from (7.4) or (7.9) is changing the resistances R_1' and R_2' while keeping the properties of FOEs constant.

Choosing $|Y_{\alpha 0}| = |Y_{\beta 0}| = 1/17\,000\text{ S}$ and $\alpha = \beta = \text{const.}$, the relation between R_1' and R_2' is similar to the previous subsection $R_2' = 4R_1' \cos^2(\pi\alpha/2)$. Fig. 7.4 depicts the tuning of the oscillator frequency by the resistances R_1' and R_2' for various values of $\alpha = \beta = \text{const.}$

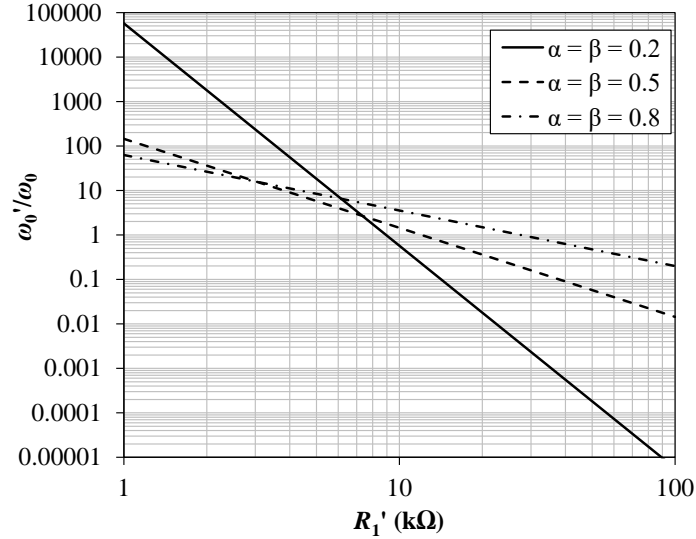


Fig. 7.4 Tuning the normalized oscillation frequency (ω_0'/ω_0) by changing R_1' (and R_2') for various values of $\alpha = \beta$

It is obvious from the figure above that the slope of the oscillation frequency vs R_1' can be modified by the selected order $\alpha = \beta$. Of particular interest is the increased range of the oscillation frequency at lower values of the order. E.g. with $\alpha = 0.2$ the oscillation frequency changes by five decades when the resistances R_1' and R_2' change by one decade. Thus, it is possible to obtain high oscillation frequencies when resistances and capacitances are relatively large compared to their values in IO oscillators. Similarly, very low oscillation frequencies can be reached without necessity to increase circuit resistances and capacitances excessively. Of course, one should again remember that sensitivities rise in this case as apparent from the relations (7.7) and (7.8).

7.1.2 Simulation and Experimental Measurement

The bulk-driven quasi-floating-gate (BD-QFG) structure of DVCC [147] designed at the author's workplace was used for the purpose of the simulation and measurement of the FO oscillator in Fig. 7.1. The conveyor was designed in Cadence platform and fabricated using 0.35 μm CMOS AMIS process with total chip area of 213 x 266 μm . The parameters of FOEs are $\alpha = \beta = 0.5$, $|Y_{\alpha 0}| = |Y_{\beta 0}| = 1/17\,000\text{ S}$ at $\omega_0 = 10\text{ krad/s}$ ($f_0 = 1\,592\text{ Hz}$). The resistances computed from (7.2) and (7.3) are again $R_1 = 12\,021\ \Omega$, $R_2 = 24\,042\ \Omega$. The value of oscillation frequency was chosen with respect to the properties of the BD-QFG conveyors and to the possible application of the oscillator in biomedical and/or other low-power applications.

The FOCs were emulated using Foster I RC circuits. Structure with ten resistors and nine capacitors was chosen in order to approximate the FOC more accurately in a wider frequency range for the purpose of oscillator tuning verification. A simpler FOC emulator structure can be sufficient if frequency tuning is not necessary or is limited to a narrow band. Details regarding the emulator are given in the source article [70].

Cadence simulations of the designed oscillator have been carried out and the obtained output voltage waveforms are presented in Fig. 7.5.

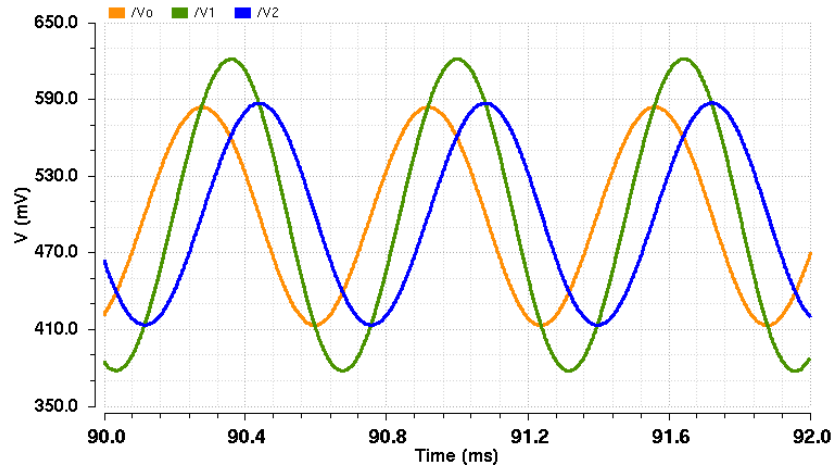


Fig. 7.5 Simulated output voltages of the designed oscillator vs time

The oscillation frequency of the simulated circuit is 1 560 Hz which is near to the theoretically expected value 1 592 Hz. The amplitudes are $V_0 = 85$ mV, $V_1 = 120$ mV, $V_2 = 86$ mV and phase shifts are 45 degrees as expected.

In order to verify the tuning capability of the oscillator, the plot of the simulated oscillation frequency, setting $\alpha' = \beta'$ and keeping R_1 constant, as a function of the order is presented in Fig. 7.6.

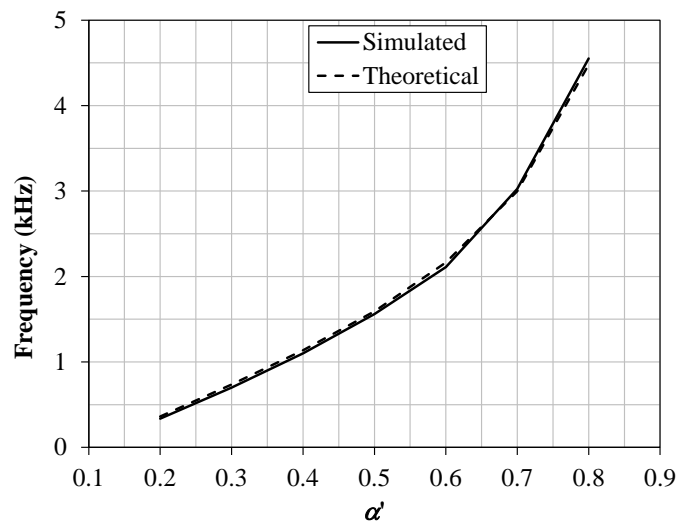


Fig. 7.6 Simulated oscillation frequency vs $\alpha' = \beta'$ ($R_1 = \text{const.}$)

The second considered possibility of tuning – by changing R_1' (while keeping $\alpha = \beta = 0.5$ and maintaining oscillation condition $R_2' \approx 2R_1'$) is shown in Fig. 7.7.

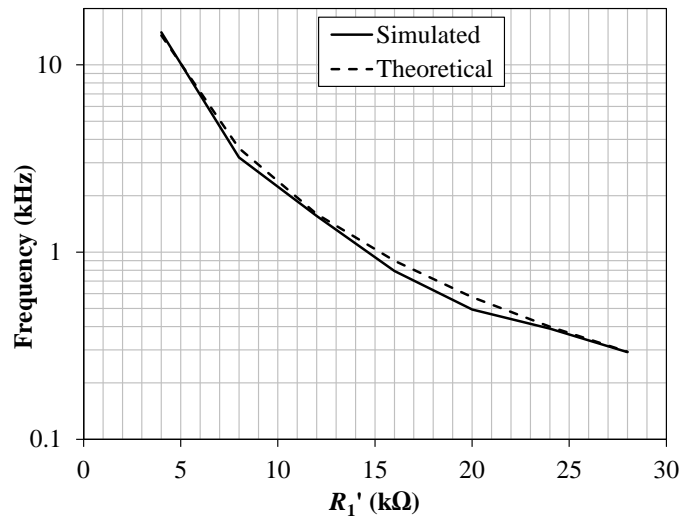


Fig. 7.7 Simulated oscillation frequency vs R_1' ($\alpha = \beta = 0.5$)

It is apparent from the two graphs above that the simulated oscillation frequency corresponds to the theoretical value.

The oscillator was also implemented with fabricated samples of BD-QFG DVCC chip and passive element parameters mentioned at the beginning of this section. The measured output voltage waveforms are presented in Fig. 7.8.

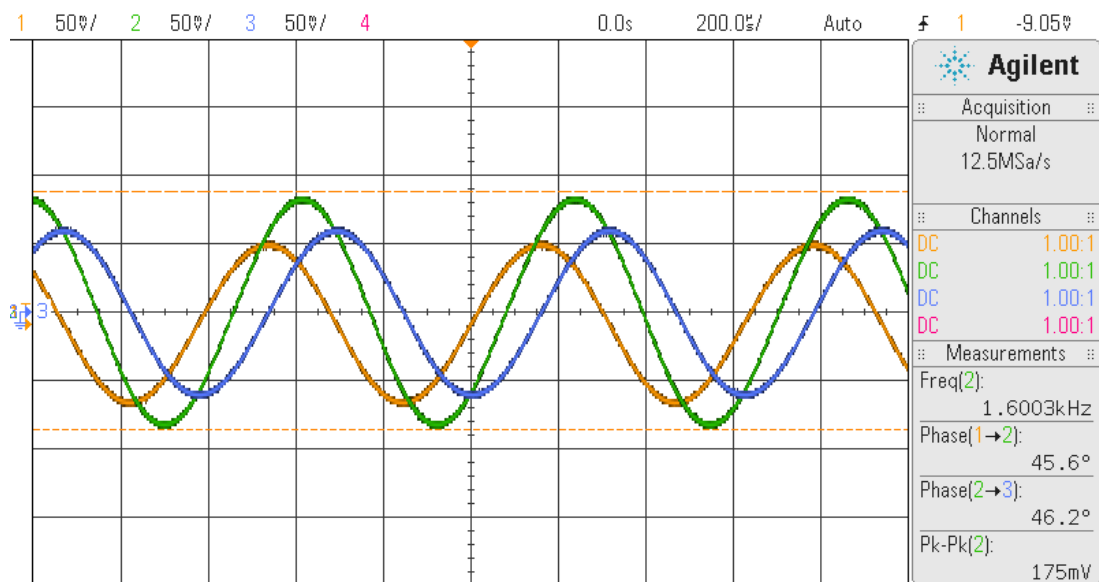


Fig. 7.8 Measured output voltages of the designed oscillator vs time

The measured oscillation frequency is 1 600 Hz which is very close to the theoretical value. Also, the phase shifts between outputs (45.6 and 46.2 degrees) and amplitudes are in accordance with expectations. The measured spectrum of the first output signal is

shown in Fig. 7.9. The fundamental harmonic component is at least 40 dB larger than the other ones. The value of THD computed from measured spectral components is approximately 1 %.

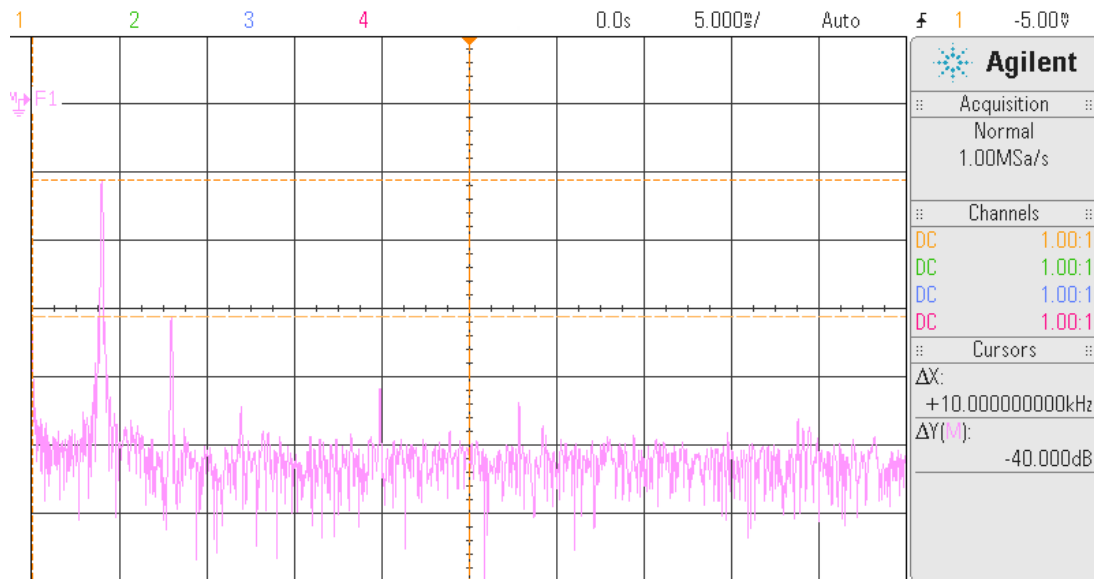


Fig. 7.9 Measured spectrum of the first output voltage (vertical scale 20 dB/div, horizontal 2 kHz/div)

Tuning the oscillation frequency of the experimental circuit by changing R_1' was also carried out. With $R_1' = 24 \text{ k}\Omega$ the oscillation frequency was 416 Hz (theoretically 399 Hz) and with $R_1' = 6.2 \text{ k}\Omega$ the oscillation frequency was 6 kHz (theoretically 5.98 kHz).

Both the simulated and the experimental results are very close to the theoretical ones and prove the attractive features of the designed FO oscillator.

7.1.3 Concluding Remarks

The author's goal was to present design and evaluation of FO oscillator from the practical point of view. The oscillator is based on a simple structure with two DVCCs, two grounded resistors, and two grounded FOCs. The theoretical analysis showed design rules for passive elements and possibilities of oscillation frequency tuning which can be done also by setting the orders α and β of FOCs. With lower values of these orders, the oscillation frequency can have much higher range than in the case of classic IO oscillator with the same parameters of passive elements. An arbitrary phase shift of output signals is another unique property which is not present at IO oscillators. The main drawbacks of the designed circuit are non-orthogonal setting of oscillation frequency and condition and high sensitivities to passive element parameters for lower values of α and β .

8. CONCLUSION

The extension of classic linear electrical circuits from the integer to the fractional domain brings generalization of their characteristics, leading to a wider usability of these circuits. It is a recent research topic, which scientists have been focusing on in the last 10 – 15 years. FO circuits find applications in a wide range of areas of electrical engineering. They provide qualitatively new properties and characteristics that are difficult to implement using classic IO circuits. As examples, let us mention their use for modeling the electrical properties of materials or objects occurring in nature, controlling processes and systems, filtering signals with the aim of extracting the required component or implementing the operation of FO derivation and integration of electrical quantities.

The theoretical design of FO circuits must be carried out with regard to feasibility with a circuit structure of reasonable complexity and with available components. The basic element of FO circuits is FOE, i.e. an element with FO impedance. Currently, intensive research is underway on these elements resulting in their implementations based on various principles, e.g. emulation using structures containing resistors and classic capacitors, implementation by electrochemical principles utilizing various chemical substances that are, however, incompatible with integration technologies and provide non-accurate FOE properties.

A key issue of FOE implementations is achieving sufficient accuracy of impedance magnitude and phase in a wide enough frequency band. At the same time, these parameters must be constant over time, and the structure should be compatible with current integrated circuit manufacturing technologies. In this respect, the implementation of FOE using RC layer structures with distributed parameters, which the author of this thesis also dealt with, brings promising results. These structures can be realized in well proven thick-film, thin-film and CMOS technology. Using the first mentioned technology, the author successfully practically verified the validity of the design method. The other two technologies will be part of future research and it is expected that the dimensions of the structures will be significantly reduced, higher operating frequencies will be achieved, and probably also the possibility of electronic control of these FOE elements will be attained.

The lack of FOE with different parameters led the author to research the impedance transformations of FOE with the aim of obtaining new values of both the impedance magnitude and, above all, its order, and thus also the type of passive element. The simulation successfully verified the method of obtaining a FO inductor using a gyrator, as well as obtaining a whole range of fractional orders using the transformation of the “seed” FOE impedance by the GIC circuit.

Using FOE, the author also managed to model the electrical properties of the cardiac cell membrane. The model presented in this thesis is more accurate than commonly used IO models.

Frequency filters and oscillators are wide group of electrical circuits that can be also designed with fractional order. FO filters provide characteristics that lie between the characteristics of classic IO filters. E.g. in the case of magnitude frequency characteristics, it is possible to obtain continuously variable slopes, in the case of phase characteristics, then continuously adjustable phases. For FO filters, it is necessary to create an analytical description, which is not available in the form of tables or mathematical relations, as with IO filters. The forms and coefficients of the TFs must be sought to obtain the desired filter characteristics and topology. For FO oscillators, the order can be used to set the oscillation frequency and, in particular, to change the dynamic range of the frequency, i.e. the steepness of the dependence of this frequency on the values of the passive elements. Furthermore, FO oscillators can provide phase shifts of output signals equal to non-integer multiples of 90 degrees. The author also dealt with these topics of FO filters and oscillators and verified the results on functional samples by computer simulations and experimental measurements.

It is worth mentioning here that the thesis is also written from a pedagogical point of view, so that the reader familiar with classic IO electrical circuits can study the topic of FO circuits and understand their benefits. The thesis covers only selected topics of the author's scientific and pedagogical work in years after Ph.D. defense, i.e. between 2006 and 2022. The same is valid for own references that are included in the Bibliography – only 42 relevant references are cited in this thesis. As stated before, David Kubánek is author or co-author of 28 journal articles and 34 international conference contributions indexed in the Web of Science Core Collection (numbers were updated in October 2022).

BIBLIOGRAPHY

- [1] Gielen, G., Maricau, E. *Analog IC Reliability in Nanometer CMOS*. Springer New York, 2013, doi: 10.1007/978-1-4614-6163-0.
- [2] Ken, X., Min, C., He, X., Chen, Z., Zheng, W. An automatic DC-Offset cancellation method and circuit for RF transceiver. In *Proc. of the 2015 IEEE 11th International Conference on ASIC, ASICON 2015*, Wangjiang, China, pp. 1-4, 2015, doi: 10.1109/ASICON.2015.7517123.
- [3] Li, K., Teng, J., Liu, Q., Xuan, X., Lu, J., Jiang, D., Huang, Y. A Digital Controller Assisted Flexible Auto-tuning Method for Continuous-time Filters. *Circuits Syst. Signal Process.*, no. 33, pp. 2401-2417, 2014, doi: 10.1007/s00034-014-9765-x.
- [4] Biolek, D., Senani, R., Biolkova, V., Kolka, Z. Active Elements for Analog Signal Processing: Classification, Review, and New Proposals. *Radioengineering*, vol. 17, no. 4, pp. 15-32, 2008, ISSN 1210-2512.
- [5] Geiger, R. L., Sanchez-Sinencio, E. Active filter design using operational transconductance amplifiers: A tutorial. *IEEE Circ. And Devices Magazine*, vol. 1, no. 2, pp. 20-32, 1985, doi: 10.1109/MCD.1985.6311946.
- [6] Fabre, A., Saaid, O., Wiest, F., Boucheron, C. High frequency applications based on a new current controlled conveyor. *IEEE Trans. on Circuits and Systems I*, vol. 43, no. 2, pp. 82-91, 1996, doi: 10.1109/81.486430.
- [7] Salama, K. N., Soliman, A. M. CMOS operational transresistance amplifier for analog signal processing. *Microelectronics Journal*, vol. 30, no. 3, pp. 235-245, 1999, doi: 10.1016/S0026-2692(98)00112-8.
- [8] Wang, J. Ye, Y., Pan, X., Gao, X. Parallel-type fractional zero-phase filtering for ECG signal denoising. *Biomedical Signal Processing and Control*, vol. 18, pp. 36-41, 2015, doi: 10.1016/j.bspc.2014.10.012.
- [9] Martinek, R., Ladrova, M., Sidikova, M., Jaros, R., Behbehani, K., Kahankova, R., Kawla-Sterniuk, A. Advanced Bioelectrical Signal Processing Methods: Past, Present and Future Approach - Part II: Brain Signals. *Sensors*, vol. 21, no. 19: 6343, 2021, doi: 10.3390/s21196343.
- [10] Freeborn, T.J. A Survey of Fractional-Order Circuit Models for Biology and Biomedicine. *IEEE Journal on Emerging and Selected Topics in Circuits and Systems*, vol. 3, no. 3, pp. 416-424, 2013, doi: 10.1109/JETCAS.2013.2265797.
- [11] Mohsen, M., Said, L.A., Madian, A.H., Radwan, A.G., Elwakil, A.S. Fractional-Order Bio-Impedance Modeling for Interdisciplinary Applications: A Review. *IEEE Access*, vol. 9, pp. 33158-33168, 2021, doi: 10.1109/ACCESS.2021.3059963.
- [12] AboBakr, A., Said, L.A., Madian, A.H., Elwakil, A.S., Radwan, A.G. Experimental comparison of integer/fractional-order electrical models of plant. *AEU - International Journal of Electronics and Communications*, vol. 80, pp. 1-9, 2017, doi: 10.1016/j.aeue.2017.06.010.

- [13] Palaniappan, A., Palermo, S.A. Design Methodology for Power Efficiency Optimization of High-Speed Equalized-Electrical I/O Architectures. *IEEE Transactions on Very Large Scale Integration (VLSI) Systems*, vol. 21, no. 8, pp. 1421-1431, 2013, doi: 10.1109/TVLSI.2012.2211628.
- [14] Tepljakov, A. *Fractional-order Modeling and Control of Dynamic Systems*. Springer International Publishing: Berlin/Heidelberg, Germany, 2017, doi: 10.1007/978-3-319-52950-9.
- [15] Oldham, K.B., Spanier, J. *The Fractional Calculus: Theory and Applications of Differentiation and Integration to Arbitrary Order*. Academic, New York, 1974, ISBN: 9780080956206.
- [16] Podlubny, I. *Fractional Differential Equations: An Introduction to Fractional Derivatives, Fractional Differential Equations, to Methods of Their Solution and Some of Their Applications*. Elsevier, 1998, ISBN: 9780080531984.
- [17] Ortigueira, M.D. *Fractional Calculus for Scientists and Engineers*. Springer: Dordrecht, Germany, 2011, doi: 10.1007/978-94-007-0747-4.
- [18] Kochubei, A., Luchko, Y., Tarasov, V.E., Petráš, I. *Handbook of Fractional Calculus with Applications, Volume 1 Basic Theory*. De Gruyter Grand Forks, 2019, doi: 10.1515/9783110571622.
- [19] Hilfer, R. *Applications of Fractional Calculus in Physics*. World Scientific, 2000, doi: 10.1142/3779.
- [20] Gutierrez, R.E., Rosario, J.M., Machado, J.T. Fractional Order Calculus: Basic Concepts and Engineering Applications. *Mathematical Problems in Engineering*, vol. 2010, Article ID 375858, 2010, doi: 10.1155/2010/375858.
- [21] Ortigueira, M.D. An introduction to the fractional continuous-time linear systems: The 21st century systems. *IEEE Circuits and Systems Magazine*, vol. 8, no. 3, pp. 19-26, 2008, doi: 10.1109/MCAS.2008.928419.
- [22] Elwakil, A.S. Fractional-order circuits and systems: An emerging interdisciplinary research area. *IEEE Circuits and Systems Magazine*, vol. 10, no. 4, pp. 40-50, 2010, doi: 10.1109/MCAS.2010.938637.
- [23] Nakagawa, M., Sorimachi, K. Basic Characteristics of a Fractance Device. *IEICE Trans. Fundam. Electron. Commun. Comput. Sci.*, vol. E75-A, no. 12, pp. 1814-1819, 1992.
- [24] Koton, J., Kubanek, D., Dvorak, J., Herencsar, N. On Systematic Design of Fractional-Order Element Series. *Sensors*, vol. 21, no. 4: 1203, 2021, doi: 10.3390/s21041203.
- [25] Tsirimokou, G. A systematic procedure for deriving RC networks of fractional order elements emulators using MATLAB. *AEU - International Journal of Electronics and Communications*, vol. 78, pp. 7-14, 2017. doi: 10.1016/j.aeue.2017.05.003.
- [26] Shah, Z.M., Kathjoo, M.Y., Khanday, F.A., Biswas, K., Psychalinos, C. A survey of single and multicomponent Fractional-Order Elements (FOEs) and their

- applications. *Microelectronics Journal*, vol. 84, pp. 9-25, 2019. doi: 10.1016/j.mejo.2018.12.010.
- [27] Caputo, M., Fabrizio, M. On the Singular Kernels for Fractional Derivatives. Some Applications to Partial Differential Equations. *Progress in Fractional Differentiation and Applications*, vol. 7, no. 2, pp. 79-82, 202, doi: 10.18576/pfda/0070201.
- [28] Losada, J., Nieto, J.J. Fractional Integral Associated to Fractional Derivatives with Nonsingular Kernels. *Progress in Fractional Differentiation and Applications*, vol. 7, no. 3, pp. 137-143, 2021, doi: 10.18576/pfda/070301.
- [29] Biswas, K., Sen, S., Dutta, P.K. Realization of a Constant Phase Element and Its Performance Study in a Differentiator Circuit. *IEEE Transactions on Circuits and Systems II: Express Briefs*, vol. 53, no. 9, pp. 802-806, 2006, doi: 10.1109/TCSII.2006.879102.
- [30] Adhikary, A., Khanra, M., Sen, S., Biswas, K. Realization of a carbon nanotube based electrochemical fractor. In *Proc. of the 2015 IEEE International Symposium on Circuits and Systems (ISCAS)*, pp. 2329-2332, 2015, doi: 10.1109/ISCAS.2015.7169150.
- [31] Elshurafa, M., Almadhoun, N., Salama, K., Alshareef, H. Microscale electrostatic fractional-order capacitors using reduced graphene oxide percolated polymer composites. *Appl. Phys. Lett.*, vol. 102, no. 232901, pp. 1-4, 2013, doi: 10.1063/1.4809817.
- [32] Buscarino, A., Caponetto, R., Di Pasquale, G., Fortuna, L., Graziani, S., Pollicino, A. Carbon Black based capacitive Fractional-order Element towards a new electronic device. *AEU - International Journal of Electronics and Communications*, vol. 84, pp. 307-312, 2018, doi: 10.1016/j.aeue.2017.12.018.
- [33] Caponetto, R., Graziani, S., Pappalardo, F.L., Sapuppo, F. Experimental Characterization of Ionic Polymer Metal Composite as a Novel Fractional Order Element. *Advances in Mathematical Physics*, vol. 2013, article ID 953695, 2013, doi: 10.1155/2013/953695.
- [34] Agambayev, A., Patole, S., Bagci, H., Salama, K.N. Tunable fractional-order capacitor using layered ferroelectric polymers. *AIP Advances*, vol. 7, no. 095202, 2017, doi: 10.1063/1.4991659.
- [35] Carlson, G.E., Halijak, C.A. Approximation of Fractional Capacitors $(1/s)^{(1/n)}$ by a Regular Newton Process. *IEEE Transactions on Circuit Theory*, vol. 11, no. 2, pp. 210-213, 1964, doi: 10.1109/TCT.1964.1082270.
- [36] Charef, A., Sun, H.H., Tsao, Y.Y., Onaral B. Fractal system as represented by singularity function. *IEEE Transactions on Automatic Control*, vol. 37, no. 9, pp. 1465-1470, 1992, doi: 10.1109/9.159595.
- [37] Matsuda, K., Fujii, H. $H(\infty)$ optimized wave-absorbing control - Analytical and experimental results. *Journal of Guidance, Control, and Dynamics*, vol. 16, no. 6, pp. 1146-1153, 1993, doi: 10.2514/3.21139.

- [38] Oustaloup, A., Levron, F., Mathieu, B., Nanot, F.M. Frequency-band complex noninteger differentiator: characterization and synthesis. *IEEE Transactions on Circuits and Systems I: Fundamental Theory and Applications*, vol. 47, no. 1, pp. 25-39, 2000, doi: 10.1109/81.817385.
- [39] El-Khazali, R. On the biquadratic approximation of fractional-order Laplacian operators. *Analog Integrated Circuits and Signal Processing*, vol. 82, no. 3, pp. 503-517, 2015, doi: 10.1007/s10470-014-0432-8.
- [40] Kapoulea, S. Design of Fractional-Order Circuits with Reduced Spread of Element Values. Master thesis. RN: 1058034, 2018, available online: https://www.researchgate.net/profile/Stavroula-Kapoulea/publication/327396441_Design_of_Fractional-Order_Circuits_with_Reduced_Spread_of_Element_Values/links/5b8d2494299bf1d5a73ab881/Design-of-Fractional-Order-Circuits-with-Reduced-Spread-of-Element-Values.pdf
- [41] Tsirimokou, G., Psychalinos, C., Elwakil, A.S. Emulation of a constant phase element using Operational Transconductance Amplifiers. *Analog Integrated Circuits and Signal Processing*, vol. 85, no. 3, pp. 413-423, 2015, doi: 10.1007/s10470-015-0626-8.
- [42] Adhikary, A., Sen, P., Sen, S., Biswas, K. Design and Performance Study of Dynamic Fractors in Any of the Four Quadrants. *Circuits, Systems, and Signal Processing*, vol. 35, pp. 1909-1932, 2016, doi: 10.1007/s00034-015-0213-3.
- [43] Cole, K.S. Permeability and impermeability of cell membranes for ions. In *Proc. of the Cold Spring Harbor Symp. Quant. Biol.*, vol. 8, pp. 110-122, 1940, doi: 10.1101/SQB.1940.008.01.013.
- [44] Freeborn, T. Comparison of $(1 + \alpha)$ Fractional-Order Transfer Functions to Approximate Lowpass Butterworth Magnitude Responses. *Circuits, Systems, and Signal Processing*, vol. 35, no. 6, pp. 1983-2002, 2016, doi: 10.1007/s00034-015-0226-y.
- [45] Biswas, K., Bohannan, G., Caponetto, R., Lopes, A.M., Machado, J.A.T. *Fractional-Order Devices*. Springer: Berlin/Heidelberg, Germany, 2017, doi: 10.1007/978-3-319-54460-1.
- [46] Tsirimokou, G., Psychalinos, C., Elwakil, A.S. *Design of CMOS Analog Integrated Fractional-Order Circuits: Applications in Medicine and Biology*. Springer: Berlin/Heidelberg, Germany, 2017, doi: 10.1007/978-3-319-55633-8.
- [47] Helie, T. Simulation of Fractional-Order Low-Pass Filters. In *IEEE/ACM Transactions on Audio, Speech, and Language Processing*, vol. 22, no. 11, pp. 1636-1647, 2014, doi: 10.1109/TASLP.2014.2323715.
- [48] Tietze, U., Schenk, C., Gamm, E. *Electronic Circuits: Handbook for Design and Application*, 2nd edition, Springer, Berlin, Heidelberg, 2008, doi: 10.1007/978-3-540-78655-9.

- [49] Freeborn, T., Maundy, B., Elwakil, A.S. Approximated Fractional Order Chebyshev Lowpass Filters. *Mathematical Problems in Engineering*, vol. 2015, Article ID 832468, pp. 1-7, 2015, doi: 10.1155/2015/832468.
- [50] Freeborn, T.J., Elwakil, A.S., Maundy, B. Approximated fractional order inverse Chebyshev lowpass filters. *Circuits, Systems, and Signal Processing*, vol. 35, pp. 1973-1982, 2016, doi: 10.1007/s00034-015-0222-2.
- [51] Kubanek, D., Freeborn, T.J., Koton, J., Dvorak, J. Validation of Fractional-Order Lowpass Elliptic Responses of $(1 + \alpha)$ -Order Analog Filters. *Applied Sciences*, vol. 8, no. 12: 2603, pp. 1-17, 2018, doi: 10.3390/app8122603.
- [52] Kubanek, D., Freeborn, T. $(1 + \alpha)$ Fractional-order transfer functions to approximate low-pass magnitude responses with arbitrary quality factor. *AEU - International Journal of Electronics and Communications*, vol. 83, pp. 570-578, 2018, doi: 10.1016/j.aeue.2017.04.031.
- [53] Kubanek, D., Freeborn, T., Koton, J. Fractional-order band-pass filter design using fractional-characteristic specimen functions. *Microelectronics Journal*, vol. 86, pp. 77-86, 2019, doi: 10.1016/j.mejo.2019.02.020.
- [54] Mahata, S., Kar, R., Mandal, D. Optimal fractional-order highpass Butterworth magnitude characteristics realization using current-mode filter. *AEU - International Journal of Electronics and Communications*, vol. 102, pp. 78-89, 2019, doi: 10.1016/j.aeue.2019.02.014.
- [55] Freeborn, T.J., Maundy, B., Elwakil, A.S. Field programmable analogue array implementation of fractional step filters. *IET Circuits Devices and Systems*, vol. 4, no. 6, pp. 514-524, 2010, doi: 10.1049/iet-cds.2010.0141.
- [56] Hamed, E.M., AbdelAty, A.M., Said, L.A., Radwan, A.G. Effect of Different Approximation Techniques on Fractional-Order KHN Filter Design. *Circuits, Systems, and Signal Processing*, vol. 37, pp. 5222-5252, 2018, doi: 10.1007/s00034-018-0833-5.
- [57] Maundy, B., Elwakil, A.S., Freeborn, T.J. On the practical realization of higher-order filters with fractional stepping. *Signal Processing*, vol. 91, no. 3, pp. 484-491, 2011, doi: 10.1016/j.sigpro.2010.06.018.
- [58] Mahata, S., Saha, S.K., Kar, R., Mandal, D. Optimal design of fractional order low pass Butterworth filter with accurate magnitude response. *Digital Signal Processing*, vol. 72, no. C, pp. 96-114, 2018, doi: 10.1016/j.dsp.2017.10.001.
- [59] Mahata, S., Saha, S., Kar, R., Mandal, D. Optimal integer-order rational approximation of α and $\alpha + \beta$ fractional-order generalised analogue filters. *IET Signal Processing*, vol. 13, no. 5, pp. 516-527, 2019, doi: 10.1049/iet-spr.2018.5340.
- [60] Mahata, S., Banerjee, S., Kar, R., Mandal, D. Revisiting the use of squared magnitude function for the optimal approximation of $(1 + \alpha)$ - order Butterworth filter. *AEU - International Journal of Electronics and Communications*, vol. 110, pp. 1-11, 2019, doi: 10.1016/j.aeue.2019.152826.

- [61] Ali, A.S., Radwan, A.G., Soliman, A.M. Fractional order Butterworth filter: active and passive realizations. *IEEE Journal on Emerging and Selected Topics in Circuits and Systems*, vol. 3, no. 3, pp. 346-354, 2013, doi: 10.1109/JETCAS.2013.2266753.
- [62] Acharya, A., Das, S., Pan, I., Das, S. Extending the concept of analog Butterworth filter for fractional order systems. *Signal Processing*, vol. 94, pp. 409-420, 2013, doi: 10.1016/j.sigpro.2013.07.012.
- [63] Said, L.A., Ismail, S.M., Radwan, A.G., Madian, A.H., El-Yazeed, M.F.A., Soliman, A.M. On the optimization of fractional order low-pass filters. *Circuits Systems, and Signal Processing*, vol. 35, no. 6, pp. 2017-2039, 2016, doi: 10.1007/s00034-016-0258-y.
- [64] Elwakil, A.S., Allagui, A., Maundy, B.J., Psychalinos, C. A low frequency oscillator using a super-capacitor. *AEU - International Journal of Electronics and Communications*, vol. 70, no. 7, pp. 970-973, 2016, doi: 10.1016/j.aeue.2016.03.020.
- [65] Lahiri, A. Low-frequency quadrature sinusoidal oscillators using current differencing buffered amplifiers. *Indian Journal of Pure & Applied Physics*, vol. 49, no. 6, pp. 423-428, 2011.
- [66] Said, L.A., Radwan, A.G., Madian, A.H., Soliman, A.M. Fractional order oscillators based on operational transresistance amplifiers. *AEU - International Journal of Electronics and Communications*, vol. 69, no. 7, pp. 988-1003, 2015, doi: 10.1016/j.aeue.2015.03.003.
- [67] Said, L.A., Radwan, A.G., Madian, A.H., Soliman, A.M. Three Fractional-Order-Capacitors-Based Oscillators with Controllable Phase and Frequency. *Journal of Circuits, Systems, and Computers*, vol. 26, no. 10, pp. 1750160-1750178, 2017, doi: 10.1142/S0218126617501602.
- [68] Fouda, M., Soltan, A., Radwan, A.G., Soliman, A.M. Fractional-order multi-phase oscillators design and analysis suitable for higher-order PSK applications. *Analog Integrated Circuits and Signal Processing*, vol. 87, no. 2, pp. 301-312, 2016, doi: 10.1007/s10470-016-0716-2.
- [69] Radwan, A.G., Elwakil, A.S., Soliman, A.M. Fractional-order sinusoidal oscillators: design procedure and practical examples. *IEEE Transactions on Circuits and Systems I: Regular Papers*, vol. 55, no. 7, pp. 2051-2063, 2008, doi: 10.1109/TCSI.2008.918196.
- [70] Kubanek, D., Khateb, F., Tsirimokou, G., Psychalinos, C. Practical Design and Evaluation of Fractional-Order Oscillator Using Differential Voltage Current Conveyors. *Circuits, Systems, and Signal Processing*, vol. 35, no. 6, pp. 2003-2016, 2016, doi: 10.1007/s00034-016-0243-5.
- [71] Said, L.A., Radwan, A.G., Madian, A.H., Soliman, A.M. Two-port two impedances fractional order oscillators. *Microelectronics Journal*, vol. 55, no. 9, pp. 40-52, 2016, doi: 10.1016/j.mejo.2016.06.003.

- [72] Sotner, R., Jerabek, J., Langhammer, L., Kartci, A., Herencsar, N., Metin, B. Practical Design of Fractional-Order Resonator for Application in the Multiphase Oscillator. In *Proc. of the 2020 27th IEEE International Conference on Electronics, Circuits and Systems (ICECS)*, pp. 1-4, 2020, doi: 10.1109/ICECS49266.2020.9294799.
- [73] Wyndrum, R.W. Jr. The exact synthesis of distributed RC networks. Dept. of Elec. Engrg., New York University, New York, Technical Report, 400-76, May 1963.
- [74] O'Shea, R. Synthesis using distributed RC networks. *IEEE Transactions on Circuit Theory*, vol. 12, no. 4, pp. 546-554, 1965, doi: 10.1109/TCT.1965.1082508.
- [75] Koton, J., Kubanek, D., Ushakov, P.A., Maksimov, K. Synthesis of fractional-order elements using the RC-EDP approach. In *Proc. of the 2017 European Conference on Circuit Theory and Design (ECCTD)*, Catania, Italy, pp. 1-4, 2017, doi: 10.1109/ecctd.2017.8093314.
- [76] Gil'mutdinov, A.K., Ushakov, P.A. Physical implementation of elements with fractal impedance: State of the art and prospects. *Journal of Communications Technology and Electronics*, vol. 62, 2017, pp. 441-453, doi: 10.1134/S1064226917050060.
- [77] Gil'mutdinov, A.K., Ushakov, P.A., El-Khazali, R. *Fractal Elements and their Applications*, Springer, Cham, 2017, doi: 10.1007/978-3-319-45249-4.
- [78] Kaiser, H.R., Castro, P.S., Nichols, A.J. *Thin-film distributed parameter circuits*. Space/Aeronautics, R&D Technical handbook, vol. 38, pp. E17-E23, 1962.
- [79] Ushakov, P.A., Maksimov, K.O., Stoychev, S.V., Gravshin, V.G., Kubanek, D., Koton, J. Synthesis of elements with fractional-order impedance based on homogenous distributed resistive-capacitive structures and genetic algorithm. *Journal of Advanced Research*, vol. 25, p. 275-283, 2020, doi: 10.1016/j.jare.2020.06.021.
- [80] Ushakov, P., Shadrin, A., Kubanek, D., Koton, J. Passive fractional-order components based on resistive-capacitive circuits with distributed parameters. In *Proc. of the 2016 39th International Conference on Telecommunications and Signal Processing (TSP)*, pp. 638-642, 2016, doi: 10.1109/TSP.2016.7760960.
- [81] Davis, L. *Handbook of Genetic Algorithms*. Nostrand Reinhold, New York. 1991. 385 p.
- [82] White, N. *Thick films*. In: Kasap S., Capper P. (editors), *Springer Handbook of Electronic and Photonic Materials*. Springer; 2017, doi: 10.1007/978-3-319-48933-9.
- [83] Kubánek, D., Koton, J., Jeřábek, J., Prášek, J., Dvořák, J., Sadílek, J. capFOE_045; Experimentální prototyp prvku s impedancí fraktálního řádu 0,45 v tlustovrstvé technologii (capFOE_045). Ústav telekomunikací, FEKT VUT v Brně, Technická 3082/12, functional sample.

- [84] Kubánek, D., Koton, J., Jeřábek, J., Prášek, J., Dvořák, J., Sadílek, J. capFOE_05; Experimentální prototyp prvku s impedancí fraktálního řádu 0,5 v tlustovrstvé technologii (capFOE_05). Ústav telekomunikací, FEKT VUT v Brně, Technická 3082/12, functional sample.
- [85] Venables, J.A. *Introduction to Surface and Thin Film Processes (1 ed.)*. Cambridge University Press, 2000, doi: 10.1017/cbo9780511755651.
- [86] Razavi, B. *Design of Analog CMOS Integrated Circuits*. Boston, MA: McGraw-Hill, 2001.
- [87] Dvorak, J., Kubanek, D., Herencsar, N., Kartci, A., Bertsias, P. Electronically Adjustable Emulator of the Fractional-Order Capacitor. *Elektronika Ir Elektrotechnika*, vol. 25, no. 6, pp. 28-34, 2019, doi: 10.5755/j01.eie.25.6.24823.
- [88] Koton, J., Sladok, O., Kubanek, D., Ushakov, P. Impedance transformation of RC-EDP based fractional-order elements. In *Proc. of Fifth Forum of Young Researchers*, pp. 94-101, 2017. ISBN: 9785752607530.
- [89] Adhikary, A., Sen, S. Biswas, K. Practical Realization of Tunable Fractional Order Parallel Resonator and Fractional Order Filters. *IEEE Transactions on Circuits and Systems I: Regular Papers*, vol. 63, no. 8, pp. 1142-1151, 2016, doi: 10.1109/TCSI.2016.2568262.
- [90] Tsirimokou, G., Psychalinos, C., Elwakil, A.S., Salama, K.N. Electronically Tunable Fully Integrated Fractional-Order Resonator. *IEEE Transactions on Circuits and Systems II: Express Briefs*, vol. 65, no. 2, pp. 166-170, 2018, doi: 10.1109/TCSII.2017.2684710.
- [91] Radwan, A.G., Fouda, M.E. Optimization of fractional-order RLC filters. *Circuits, Systems, and Signal Processing*, vol. 32, no. 5, pp. 2097-2118, 2013, doi: 10.1007/s00034-013-9580-9.
- [92] Freeborn, T.J., Maundy, B., Elwakil, A.S. Fractional Resonance-Based $RL_{\beta}C_{\alpha}$ Filters. *Mathematical Problems in Engineering*, Article ID 726721, pp. 1-10, 2013, doi: 10.1155/2013/726721.
- [93] Kartci, A., Agambayev, A., Farhat, M., Herencsar, N., Brancik, L., Bagci, H., Salama, K.N. Synthesis and Optimization of Fractional-Order Elements Using a Genetic Algorithm. *IEEE Access*, vol. 7, pp. 80233-80246, 2019, doi: 10.1109/ACCESS.2019.2923166.
- [94] Deliyannis, T, Sun, Y., Fidler, J.K. *Continuous-time Active Filter Design*. CRC Press, USA, 1999.
- [95] Kubanek, D., Koton, J., Dvorak, J., Herencsar, N., Sotner, R. Analysis of OTA-Based Gyrator Implementing Fractional-Order Inductor. In *Proc. of the 2020 43rd International Conference on Telecommunications and Signal Processing (TSP)*, Milan, Italy. IEEE, pp. 583-588, 2020, doi: 10.1109/TSP49548.2020.9163406.
- [96] Kubanek, D., Koton, J., Dvorak, J., Herencsar, N., Sotner, R. Optimized Design of OTA-Based Gyrator Realizing Fractional-Order Inductance Simulator: A Comprehensive Analysis. *Applied Sciences*, vol. 11, no. 1: 291, pp. 1-19, 2021, doi: 10.3390/app11010291. ISSN: 2076-3417.

- [97] Sotner, R., Jerabek, J., Kartci, A., Domansky, O., Herencsar, N., Kledrowetz, V., Alagoz, B.B., Yeroglu, C. Electronically reconfigurable two-path fractional-order PI/D controller employing constant phase blocks based on bilinear segments using CMOS modified current differencing unit. *Microelectronics Journal*, vol. 86, 2019, pp. 114-129, doi: 10.1016/j.mejo.2019.03.003.
- [98] Koton, J., Herencsar, N., Kubanek, D., Psychalinos, C. Fractional-Order Elements of Complement Order. In *Proc. of the 2017 10th International Conference on Electrical and Electronics Engineering (ELECO)*, Bursa, pp. 1212-1215, 2017, ISBN: 978-605-01-0737-1.
- [99] Koton, J., Kubanek, D., Herencsar, N., Dvorak, J., Psychalinos, C. Designing constant phase elements of complement order. *Analog Integrated Circuits and Signal Processing*, vol. 97, no. 1, pp. 107-114, 2018, doi: 10.1007/s10470-018-1257-7.
- [100] Antoniou, A. Bandpass transformation and realization using frequency-dependent negative-resistance elements. *IEEE Transactions on Circuit Theory*, vol. 18, no. 2, pp. 297-299, 1971, doi: 10.1109/TCT.1971.1083241.
- [101] Analog Devices. AD844 60 MHz, 2000 V/ μ s Monolithic Op Amp with Quad Low Noise. Datasheet, Rev. G, 2017.
- [102] Koton, J., Dvorak, J., Kubanek, D., Herencsar, N. Design of Fractional Order Elements' Series. In *Proc. of the 2019 11th International Conference on Electrical and Electronics Engineering (ELECO)*, pp. 496-499, 2019 doi: 10.23919/ELECO47770.2019.8990413.
- [103] Koton, J., Dvorak, J., Kubanek, D., Herencsar, N. Designing series of fractional-order elements. *Analog Integrated Circuits and Signal Processing*, vol. 106, no. 3, p. 553-563, 2012, doi: 10.1007/s10470-021-01811-4.
- [104] Koton, J., Kubanek, D., Dvorak, J., Kledrowetz, V. FGIC44 – Fully controllable immittance converter. Brno University of Technology, FEEC, Dept. of Telecommunications, Technicka 12, 616 00 Brno, functional sample.
- [105] Dvorak, J., Kubanek, D., Koton, J. FGIC44 - Fully Controllable Immittance Converter: Chip Performance Evaluation. In *Proc. of the 2021 13th International Congress on Ultra Modern Telecommunications and Control Systems and Workshops (ICUMT)*, pp. 182-187, 2021, doi: 10.1109/ICUMT54235.2021.9631676.
- [106] Kubanek, D., Koton, J., Svecova, O. Extraction of Cardiac Cell Membrane Fractional-Order Capacitance from Current Response to Voltage Step. *Elektronika Ir Elektrotechnika*, vol. 28, no. 4, pp. 42-47, 2022, doi: 10.5755/j02.eie.31151.
- [107] Freeborn, T.J., Maundy, B., Elwakil, A. Simplifying Cole-impedance extraction from the current-excited step response. In *Proc. of the 2013 IEEE 56th International Midwest Symposium on Circuits and Systems (MWSCAS)*, pp. 952-955, 2013, doi: 10.1109/MWSCAS.2013.6674808.

- [108] Freeborn, T.J., Maundy, B., Elwakil, A.S. Cole impedance extractions from the step-response of a current excited fruit sample. *Computers and Electronics in Agriculture*, vol. 98, pp. 100-108, 2013. doi: 10.1016/j.compag.2013.07.017.
- [109] Gillis, K.D. Techniques for membrane capacitance measurements. In: *Sakmann, B., Neher, E. (Eds.), Single-channel recording*, Springer, Boston, pp. 155-198, 1995. doi: 10.1007/978-1-4419-1229-9_7.
- [110] Thompson, R.E., Lindau, M., Webb, W.W. Robust, High-Resolution, Whole Cell Patch-Clamp Capacitance Measurements Using Square Wave Stimulation. *Biophysical Journal*, vol. 81, no. 2, pp. 937-948, 2001, doi: 10.1016/S0006-3495(01)75752-9.
- [111] Wang, X., Becker, F.F., Gascoyne, P.R. The fractal dimension of cell membrane correlates with its capacitance: a new fractal single-shell model. *Chaos*, vol. 20, no. 4: 043133, 2010, doi: 10.1063/1.3526972.
- [112] Simurda, J., Simurdova, M., Svecova, O., Bebarova, M. A new approach to the determination of tubular membrane capacitance: passive membrane electrical properties under reduced electrical conductivity of the extracellular solution. *BioRxiv*, Preprint (Submitted for publication), 2021, doi: 10.1101/2021.11.12.468264.
- [113] Bebarova, M., Matejovic, P., Pasek, M., Simurdova, M., Simurda, J. Effect of ajmaline on action potential and ionic currents in rat ventricular myocytes. *General Physiology and Biophysics*, vol. 24, no. 3, pp. 311-325, 2005.
- [114] Hotka, M., Zahradnik, I. Reconstruction of membrane current by deconvolution and its application to membrane capacitance measurements in cardiac myocytes. *PloS ONE*, vol. 12, no. 11, e0188452, 2017, doi: 10.1371/journal.pone.0188452.
- [115] Monje, C.A., Chen, Y., Vinagre, B., Xue, D., Feliu, V. *Fractional order systems and controls - Fundamentals and applications*. Advances in industrial control series, Springer, Berlin, 2010, doi: 10.1007/978-1-84996-335-0.
- [116] Podlubny, I. Mittag-Leffler function (<https://www.mathworks.com/matlabcentral/fileexchange/8738-mittag-leffler-function>), MATLAB Central File Exchange. Retrieved September 05, 2022.
- [117] Simurda, J., Simurdova, M., Svecova, O. A new simple approach to estimation of membrane capacitance from current responses to voltage clamp steps. *Progress in Biophysics and Molecular Biology*, vol. 157, pp. 18-23, 2020, doi: 10.1016/j.pbiomolbio.2020.04.005.
- [118] Elwan, H.O., Soliman, A.M. Novel CMOS differential voltage current conveyor and its application. *IEE Proceedings of Circuits Devices System*, vol. 144, no. 3, pp. 195-200, 1997, doi: 10.1049/ip-cds:19971081.
- [119] PSpice User's Guide © 1985-2000, Cadence Design Systems, Inc.
- [120] Khatoon, S. Practical Realization of Current Mode Active Elements Using AD844 and some Applications. *Indian Journal of Applied Research*, vol. 3, no. 5, pp. 303-307, 2013, doi: 10.36106/ijar.

- [121] Bertias, P., Khateb, F., Kubanek, D., Khanday, F., Psychalinos, C. Capacitorless Digitally Programmable Fractional-Order Filters. *AEU - International Journal of Electronics and Communications*, vol. 78, pp. 228-237, 2017, doi: 10.1016/j.aeue.2017.04.030.
- [122] Freeborn, T.J., Maundy, B., Elwakil, A. Fractional-step Tow-Thomas biquad filters. *Nonlinear Theory and Its Applications*, IEICE, vol. 3, no. 3, pp. 357-374, 2012, doi: 10.1587/nolta.3.357.
- [123] Kubanek, D., Freeborn, T., Koton, J., Herencsar, N. Evaluation of $(1 + \alpha)$ Fractional-Order Approximated Butterworth High-Pass and Band-Pass Filter Transfer Functions. *Elektronika Ir Elektrotechnika*, vol. 24, no. 2, pp. 37-41, 2018, doi: 10.5755/j01.eie.24.2.20634.
- [124] Ahmadi, P., Maundy, B., Elwakil, A.S., Belostotski, L. High-quality factor asymmetric-slope band-pass filters: a fractional-order capacitor approach. *IET Circuits, Devices & Systems*, vol. 6, no. 3, pp. 187-197, 2012, doi: 10.1049/iet-cds.2011.0239.
- [125] Verma, R., Pandey, N., Pandey, R. Electronically Tunable Fractional Order Filter. *Arabian Journal for Science and Engineering*, vol. 42, pp. 3409-3422, 2017, doi: 10.1007/s13369-017-2500-8.
- [126] Kubanek, D., Freeborn, T., Koton, J., Dvorak, J. Transfer Functions of Fractional-Order Band-Pass Filter with Arbitrary Magnitude Slope in Stopband. In *Proc. of the 2019 42nd International Conference on Telecommunications and Signal Processing (TSP)*, Budapest, Hungary, pp. 655-659, 2019, doi: 10.1109/TSP.2019.8769089.
- [127] Kubanek, D., Koton, J., Jerabek, J. Design and properties of fractional-order multifunction filter with DVCCs. In *Proc. of the 2016 39th International Conference on Telecommunications and Signal Processing (TSP)*, pp. 620-624, 2016, doi: 10.1109/TSP.2016.7760956.
- [128] Kubanek, D., Koton, J., Jerabek, J., Andriukaitis, D. $(N + \alpha)$ -Order low-pass and high-pass filter transfer functions for non-cascade implementations approximating Butterworth response. *Fractional Calculus and Applied Analysis*, vol. 24, no. 3, pp. 689-714, 2021, doi: 10.1515/fca-2021-0030.
- [129] Perry, D.J. New multiple feedback active RC network. *Electronics Letters*, vol. 11, no. 16, pp. 364-365, 1975, doi: 10.1049/el:19750278.
- [130] Linear Technology. LT1228 100 MHz Current Feedback Amplifier with DC Gain Control. Datasheet, 2012.
- [131] Kubanek, D., Koton, J., Ushakov, P. Fractional-Order Multiple-Feedback Filter Employing RC Element with Distributed Parameters. In *Proc. of the Fifth Forum of Young Researchers*, Izhevsk, Russia: Publishing House of Kalashnikov ISTU, pp. 70-74, 2017, ISBN: 978-5-7526-0753-0.
- [132] Kubanek, D., Koton, J., Dvorak, J. Influence of Fractional-Order Element Properties on Frequency Filter Characteristics. In *Proc. of the 2019 11th International Congress on Ultra Modern Telecommunications and Control*

- Systems and Workshops (ICUMT)*, Dublin, Ireland, pp. 1-5, 2019, doi: 10.1109/ICUMT48472.2019.8970959.
- [133] Koton, J., Jerabek, J., Kubanek, D., Dvorak, J. Analog Filters with Arbitrarily Adjustable Frequency Response. In *Fractional Order Systems: Optimization, Control, Circuit Realizations and Applications*. Advances in Nonlinear Dynamics and Chaos (ANDC). Academic Press, pp. 383-419, 2018, doi: 10.1016/C2017-0-04459-2.
- [134] Freeborn, T., Kubanek, D., Koton, J., Dvorak, J. Fractional-order Lowpass Elliptic Responses of $(1 + \alpha)$ -order Transfer Functions. In *Proc. of the 41st International Conference on Telecommunications and Signal Processing (TSP)*, pp. 1-5, 2018, doi: 10.1109/TSP.2018.8441421.
- [135] Khateb, F., Kubanek, D., Tsirimokou, G., Psychalinos, C. Fractional-order filters based on low-voltage DDCCs. *Microelectronics Journal*, vol. 50, pp. 50-59, 2016, doi: 10.1016/j.mejo.2016.02.002.
- [136] Koton, J., Kubanek, D., Vrba, K., Shadrin, A., Ushakov, P. Universal voltage conveyors in fractional-order filter design. In *Proc. of the 2016 39th International Conference on Telecommunications and Signal Processing (TSP)*, pp. 593-598, 2016, doi: 10.1109/TSP.2016.7760950.
- [137] Koton, J., Kubanek, D., Sladok, O., Vrba, K., Shadrin, A., Ushakov, P. Fractional-Order Low- and High-Pass Filters Using UVCs. *Journal of Circuits, Systems and Computers*, vol. 26, no. 12, pp. 1-22, 2017, doi: 10.1142/S0218126617501924.
- [138] Jerabek, J., Sotner, R., Kubanek, D., Dvorak, J., Langhammer, L., Herencsar, N., Vrba, K. Fractional-Order Low-Pass Filter with Electronically Adjustable Parameters. In *Proc. of the 2016 39th International Conference on Telecommunications and Signal Processing (TSP)*, pp. 569-574, 2016, doi: 10.1109/TSP.2016.7760945.
- [139] Jerabek, J., Sotner, R., Dvorak, J., Polak, J., Kubanek, D., Herencsar, N., Koton, J. Reconfigurable Fractional-Order Filter with Electronically Controllable Slope of Attenuation, Pole Frequency and Type of Approximation. *Journal of Circuits, Systems and Computers*, vol. 26, no. 10, pp. 1-21, 2017, doi: 10.1142/S0218126617501572.
- [140] Koton, J., Jerabek, J., Herencsar, N., Kubanek, D. Current conveyors in current-mode circuits approximating fractional-order low-pass filter. In *Proc. of the 2017 European Conference on Circuit Theory and Design (ECCTD)*, Catania, Italy, pp. 1-4, 2017, doi: 10.1109/ECCTD.2017.8093277.
- [141] Mahata, S., Herencsar, N., Kubanek, D. Optimal Approximation of Fractional-Order Butterworth Filter Based on Weighted Sum of Classical Butterworth Filters. *IEEE Access*, vol. 9, pp. 81097-81114, 2021, doi: 10.1109/ACCESS.2021.3085515.
- [142] Mahata, S., Herencsar, N., Kubanek, D., Kar, R., Mandal, D., Gökner, I.C. A Fractional-Order Transitional Butterworth-Butterworth Filter and Its Experimental

- Validation. *IEEE Access*, vol. 9, pp. 129521-129527, 2021, doi: 10.1109/ACCESS.2021.3114182.
- [143] Mahata, S., Herencsar, N., Kubanek, D. On the Design of Power Law Filters and Their Inverse Counterparts. *Fractal and Fractional*, vol. 5, no. 4: 197, pp. 1-23, 2021, doi: 10.3390/fractalfract5040197.
- [144] Mahata, S., Herencsar, N., Kubanek, D. Further Generalization and Approximation of Fractional-Order Filters and Their Inverse Functions of the Second-Order Limiting Form. *Fractal and Fractional*, vol. 6, no. 4: 209, pp. 1-25, 2022, doi: 10.3390/fractalfract6040209.
- [145] Kubanek, D., Vrba, K., Ushakov, P. Oscillator with Current Conveyors and Fractional Capacitors. In *Proc. of the Fourth Forum of Young Researchers*. Izhevsk, Russia, pp. 343-347, 2014, ISBN: 978-5-7526-0649-6.
- [146] Dvorak, J., Kubanek, D., Koton, J., Jerabek, J., Smekal, D. Adjustable Multiphase Sinusoidal Oscillator with Fractional-Order Elements. In *Proc. of the 2019 11th International Congress on Ultra Modern Telecommunications and Control Systems and Workshops (ICUMT)*, Dublin, Ireland, pp. 1-6, 2019, doi: 10.1109/ICUMT48472.2019.8970842.
- [147] Khateb, F. The experimental results of the bulk-driven quasi-floating-gate MOS transistor. *AEU - International Journal of Electronics and Communications*, vol. 69, no. 1, pp. 462-466, 2015, doi: 10.1016/j.aeue.2014.10.016.

ABBREVIATIONS AND SYMBOLS

Abbreviations:

ac	alternating current
BD-QFG	Bulk-Driven Quasi-Floating-Gate
BP	Band-Pass
BS	Band-Stop
C	Capacitor
CCCII	Current Controlled Current Conveyor of Second Generation
CMOS	Complementary Metal Oxide Semiconductor
COMP	Compensation terminal
CPE	Constant Phase Element
dc	direct current
DDCC	Differential Difference Current Conveyor
DVCC	Differential Voltage Current Conveyor
FDNR	Frequency-Dependent Negative Resistor
FLF	Follow-the-Leader Feedback
FO	Fractional-Order
FOC	Fractional-Order Capacitor
FOE	Fractional-Order Element
FOI	Fractional-Order Inductor
GA	Genetic Algorithm
GIC	General Immittance Converter
HP	High-Pass
IFLF	Inverse Follow-the-Leader Feedback
IO	Integer-Order
L	Inductor
LP	Low-Pass
LSE	Least Squares Error
MOS	Metal Oxide Semiconductor
OTA	Operational Transconductance Amplifier
OTRA	Operational Transresistance Amplifier
R	Resistor
RC	Resistive-Capacitive
RC-EDP	Resistive-Capacitive Layer Elements with Distributed Parameters
TF	Transfer Function
UVC	Universal Voltage Conveyor
VDCC	Voltage Differencing Current Conveyor

Symbols:

A	Set defining nodes of R-C-NRs connected to gnd node	
<i>a</i>	Coefficient of a polynomial or a function	(-)
B	Set defining connections of terminals of R-C-NRs	
<i>b</i>	Coefficient of a polynomial or a function	(-)
<i>B(ω)</i>	Butterworth filter transfer function	(-)
<i>BW</i>	Bandwidth (of a filter)	(rad/sec)
<i>C</i>	Capacitance	(F)
C	Set of circuit structure factors of R-C-NR FOE	
<i>D</i>	Parameter of FDNR element	(Ω·F ²)
E	Set defining interconnections of adjacent R-C-NRs	
<i>E(·)</i>	Mittag-Leffler function	
<i>f</i>	Frequency	(Hz)
<i>F</i>	Fractance	(F/sec ^{1-α})
<i>F(s)</i>	Laplace transform (<i>s</i> -domain image) of a function <i>f(t)</i>	
<i>f(t)</i>	Function of time	
<i>FD</i>	Fractal dimension	(-)
<i>Fit</i>	Fitness function	(-)
<i>G</i>	Conductance	(S)
<i>g_m, g</i>	Transconductance	(S)
<i>h</i>	Auxiliary variable in mathematical relations	(-)
<i>H(s)</i>	Transfer function of a filter in <i>s</i> -domain	(-)
<i>i</i>	Auxiliary variable in mathematical relations	(-)
<i>I, i</i>	Current	(A)
<i>j</i>	Auxiliary variable in mathematical relations	(-)
<i>j</i>	Imaginary unit	
<i>k</i>	Parameter of FO filter TF, number of integrator converted to FO	(-)
<i>L</i>	Dimensionless length of R-C-NR section	(-)
L	Set of lengths (<i>L</i>) of R-C-NR sections	
$\mathcal{L}\{\cdot\}$	Laplace transform	
<i>L_F</i>	Final length of R-C-NR section	(m)
<i>LSE</i>	Least Squares Error	
<i>m</i>	Auxiliary variable in mathematical relations	(-)
<i>M</i>	Constant defining limit of summation, number of datapoints	(-)
<i>N</i>	Ratio of top and bottom layer resistances of R-C-NR structure	(-)
<i>n</i>	Integer component of order	(-)
N	Set of ratios of layer resistances (<i>N</i>) of R-C-NR FOE	
P	Set of parametric factors of R-C-NR FOE	
<i>p</i>	Range of FOE order <i>α</i> realized by GIC	(-)
<i>Q</i>	Quality factor	(-)

R	Resistance	(Ω)
$RecCur$	Recorded current response	(A)
s	Complex variable in Laplace transform	(rad/s)
t	Time	(sec)
T	Time period	(sec)
V, v	Voltage	(V)
W	Dimensionless width of R-C-NR structures, here $W = 1$	(-)
W_F	Final width of R-C-NR section	(m)
x	Parameter of genetic algorithm (maximum number of iterations)	(-)
X	Sought vector of coefficients of a function	(-)
y	Parameter of genetic algorithm (maximum number of iterations)	(-)
$Y, Y(s)$	Admittance	(S)
z	Argument of Mittag-Leffler function	(-)
$Z, Z(s)$	Impedance	(Ω)
α	Fractional component of order, order of differentiation	(-)
β	Fractional component of order, complementary order ($1 - \alpha$)	(-)
γ	Parameter of Mittag-Leffler function	(-)
$\Gamma(\cdot)$	Gamma function	
δ	Parameter of genetic algorithm (threshold for fitness function)	(-)
Δ	Absolute magnitude error	(dB)
ε	Allowed phase deviation	(rad), (deg)
θ	Auxiliary variable in R-C-NR structure admittance matrix	(-)
λ	Parameter of Mittag-Leffler function	(-)
σ	Auxiliary variable for computing fitness function	(-)
ϕ	Phase of impedance	(rad), (deg)
Ψ	Set of all factors of R-C-NR FOE	
ω	Angular frequency	(rad/s)

LIST OF FIGURES

3.1	(a) 3D view of R-C-NR structure; (b) its equivalent schematic	20
3.2	Example of the allowed window of the phase response for fitness function calculation	23
3.3	Flow-chart of algorithm for R-C-NR FOE synthesis	24
3.4	Dialog windows of the FOE synthesis program; (a) input and (b) output data of synthesis	26
3.5	Designed topology of FOE.....	27
3.6	Photograph of the fabricated thick-film FOE sample [83] (dimensions approx. 43x16 mm)	28
3.7	Phase characteristics of the synthesized R-C-NR FOE (black), measured samples (red), simulated with the real properties of the manufactured materials (blue), and measured samples with compensation of contact parasitic capacitances (green)	28
4.1	Schematic symbol of OTA.....	31
4.2	OTA-based gyrator.....	31
4.3	Gyrator with OTA parasitic properties.....	32
4.4	Passive circuit with the input admittance (4.5); the relations in the schematic express admittances of the particular elements	33
4.5	Bode magnitude and phase admittance characteristics expressing (4.5) (the values at the magnitude characteristic denote the order of the admittance in the respective frequency band)	34
4.6	Simulated magnitude and phase characteristics of gyrator input admittance	37
4.7	General view on immittance converter.....	38
4.8	Schematic symbol of CCII	40
4.9	General immittance converter using CCII and OTA as active elements	41
4.10	View on general immittance converter as a function block.....	42
4.11	Feasible phase angles of Y_{IN} (4.22) using up to two seed FOEs with $\alpha_{seed1} = 0.25$ and $\alpha_{seed2} = 0.0625$	44
4.12	Proposed OTA-based general immittance converter.....	46
4.13	Proposed OTA-based general immittance converter for $p = 4$	47
4.14	Proposed GIC with OTA parasitic properties.....	48
4.15	Magnitude frequency characteristics of the working (red line) and parasitic (black line) admittances of the nodes A to D	49
4.16	Magnitude frequency characteristics of the working (red lines) and parasitic (black lines) admittances of the node E	50
4.17	Phasor diagram resulting in zero admittance of node E	51
4.18	Circuit with negative conductance (a) between terminal COMP and ground; (b) between terminals COMP+ and COMP-	53
4.19	Simulation results of admittance of designed “seed” FOEs with central frequency 1 kHz: (a) Magnitude responses; (b) phase responses.....	54
4.20	Circuit layout of the proposed GIC	55
4.21	Simulation results of input admittance of the proposed GIC with OTA parasitics: (a) Magnitude responses; (b) phase responses	56
4.22	Simulation results of input admittance of proposed GIC with compensated OTA parasitics: (a) Magnitude responses; (b) phase responses	59
5.1	Single-dispersion Cole impedance model	60
5.2	Experimental setup for measuring current step response of cell membrane	61
5.3	Imposed voltage pulse and response of the membrane current	62
5.4	Current transient responses: recorded (black), fitted with FOC (red), fitted with classic capacitor (green), and response with model parameters detected by 3P method [117] (blue).....	66

5.5	Relative errors of responses fitted with FOC (red), fitted with classic capacitor (green), and model parameters detected by 3P method [117] (blue) against the recorded response	67
6.1	Coefficients b to approximate second-order magnitude response using (6.1) – (6.3) as blue, black, and green lines, respectively, for: (a) $Q = 0.707$; (b) $Q = 2$; (c) $Q = 5$	72
6.2	Maximum errors of approximation of (6.4) by (6.1), (6.2), and (6.3) as blue, black, and green lines, respectively; for $Q = 0.707, 2,$ and 5 as full, dashed, and dotted lines respectively: (a) values of b found by <i>fminsearch</i> ; (b) values of b approximated by (6.6)	74
6.3	Magnitude and phase of TF (6.2) vs frequency for $\alpha = 0.25, 0.5,$ and 0.75 : (a) $Q = 0.707$; (b) $Q = 2$; (c) $Q = 5$	76
6.4	Fractional-order filter with DVCCs.....	77
6.5	Grounded FOE implemented by GFREQ block in OrCAD	78
6.6	Implementation of DVCC ₁ with R ₁ by two AD844s.....	78
6.7	Simulated (solid) and ideal (dotted) magnitude and phase characteristics of the LP filter of the order 1.5 and $Q = 5$	79
6.8	Target function (6.16) given as a dotted line compared to its IO components, specifically the first order LP response (green), first-order HP response (blue), and second-order BP response (black)	82
6.9	Magnitude frequency characteristics of the TF (6.13) with new coefficients from (6.17) (solid lines), and the target function (6.16) (dotted lines) for $\alpha = 0.25$ (green), 0.5 (blue), and 0.75 (black) and (a) $\beta = 0.25$; (b) $\beta = 0.5$; (c) $\beta = 0.75$	85
6.10	Mean (a) and maximum (b) absolute dB magnitude errors of the function (6.13) with the new coefficients compared to the target function (6.16) depending on α and β	87
6.11	Tow-Thomas FO BP filter topology.....	88
6.12	Simulated and measured magnitude frequency characteristics of the Tow-Thomas filter in Fig. 6.11 with $\alpha = 0.8$ and $\beta = 0.2$	89
6.13	Inverse follow-the-leader feedback (IFLF) structure implementing (6.23).....	91
6.14	Maximum absolute error between magnitude in dB of (6.24) and (6.25) for $n = 2$	93
6.15	Maximum absolute error between magnitude in dB of (6.24) and (6.25) for $n = 3$	94
6.16	Maximum absolute error between magnitude in dB of (6.24) and (6.25) for $n = 4$	94
6.17	Maximum absolute error between magnitude in dB of (6.24) and (6.25) for $n = 5$	95
6.18	Coefficients of TF (6.24) with $n = 2$ and $k = 2$ found by <i>fminsearch</i> function (solid lines) and interpolated by (6.28) (dotted lines)	95
6.19	OTA-based 2.25-order LP filter	98
6.20	Target acc. to (6.25) (solid black), optimized acc. to (6.34) (dashed black), and simulated (dotted black) magnitude characteristics of the Butterworth LP filter of the order 2.25	99
6.21	Magnitude errors of optimized (6.34) (dashed), and simulated (dotted) characteristics from Fig. 6.20 vs. target function (6.25)	99
6.22	Optimized acc. to (6.34) (dashed), and simulated (dotted) phase characteristics of the Butterworth LP filter of the order 2.25	100
7.1	Oscillator with current conveyors and FO admittances.....	104
7.2	(a) Tuning of normalized oscillation frequency (ω_0'/ω_0) by changing the order of both FOEs ($R_1 = \text{const.}$), and (b) computed values of R_2' as a function of the order	107
7.3	(a) Tuning of normalized oscillation frequency (ω_0'/ω_0) by changing the order of both FOEs ($R_2 = \text{const.}$), and (b) computed values of R_1' as a function of the order	108
7.4	Tuning the normalized oscillation frequency (ω_0'/ω_0) by changing R_1' (and R_2') for various values of $\alpha = \beta$	109
7.5	Simulated output voltages of the designed oscillator vs time.....	110
7.6	Simulated oscillation frequency vs $\alpha' = \beta'$ ($R_1 = \text{const.}$).....	110
7.7	Simulated oscillation frequency vs R_1' ($\alpha = \beta = 0.5$).....	111

7.8	Measured output voltages of the designed oscillator vs time	111
7.9	Measured spectrum of the first output voltage (vertical scale 20 dB/div, horizontal 2 kHz/div)	112

LIST OF TABLES

4.1	Combinations of admittances Y_i , their α_i and the unique fractional order α of Y_{IN} for $\alpha_{seed} = 0.2$	44
4.2	Combinations of admittances Y_i , their α_i and the unique fractional order α of Y_{IN} for $\alpha_{seed1} = 0.25$ and $\alpha_{seed2} = 0.0625$	45
5.1	Extracted parameter values and errors for the considered extraction methods.....	67
6.1	Stop-band slopes (dB/dec) of the TF (6.13), of the target function (6.16), and theoretical slope values	86